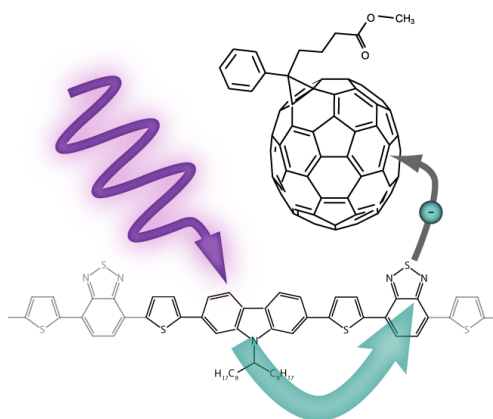


Excitation Dynamics and Charge Carrier Generation in Organic Semiconductors



Dissertation zur Erlangung des
naturwissenschaftlichen Doktorgrades
der Bayerischen Julius-Maximilians-Universität
Würzburg



vorgelegt von
Björn GIESEKING
aus Minden

Würzburg 2014

Eingereicht am: 08.04.2014
bei der Fakultät für Physik und Astronomie

1. Gutachter: Prof. Dr. Vladimir Dyakonov
2. Gutachter: Prof. Dr. Jean Geurts
3. Gutachter: Prof. Dr. Wolfgang Kinzel
der Dissertation.

1. Prüfer: Prof. Dr. Vladimir Dyakonov
2. Prüfer: Prof. Dr. Jean Geurts
3. Prüfer: Prof. Dr. Wolfgang Kinzel
im Promotionskolloquium.

Tag des Promotionskolloquiums: 03.07.2014

Doktorurkunde ausgehändigt am:

» DAT HEFF ICK MI GLIEKS DACHT. «

G. Giesecking

Kurzfassung

Der Transport optischer Anregungen, genannt Exzitonen, sowie deren Umwandlung in Ladungsträger stellen die beiden wesentlichen Mechanismen dar, welche die Funktion von organischer Photovoltaik (OPV) erst ermöglichen. Daher ist ein genaues Verständnis dieser Prozesse, der beteiligten Mechanismen sowie möglicher Verlustkanäle von essentieller Bedeutung, um die Effizienz organischer Solarzellen weiter zu steigern. Für die Untersuchung der genannten Vorgänge bieten sich grundsätzlich spektroskopische Methoden, wie etwa die Untersuchung der Absorptions- und Emissioncharakteristiken, an. Da sich viele der erwähnten Prozesse auf der sub-Nanosekunden (ns) Zeitskala abspielen, werden für deren Untersuchung hoch-zeitaufgelöste Messmethoden benötigt. Aus diesem Grund wurden im Rahmen dieser Arbeit zwei Messmethoden, basierend auf einem Femtosekunden-Lasersystem aufgebaut und verwendet. Hierbei handelt es sich um die Picosekunden (ps) zeitaufgelöste Photolumineszenz-Spektroskopie (PL) und die transiente Absorptionsspektroskopie (TA).

Anhand des prototypischen organischen Halbleiters Rubren habe ich mich mit der Fragestellung beschäftigt, inwieweit ein alternativer Ansatz zur Erhöhung der Effizienz von organischen Solarzellen, basierend auf der Nutzung von Triplet Exzitonen, welche durch Singlet Fission generiert wurden, genutzt werden könnte. Bei der Singlet Fission werden aus einem optisch angeregten Singlet Exziton zwei Triplet Exzitonen erzeugt, unter der Voraussetzung, dass die Summe der Energien der beiden Triplets in etwa der Energie des Singlet Exzitons entspricht. Hierfür wurde der Einfluss von charakteristischen Längenskalen auf die Exzitonendynamik in verschiedenen Rubren-Morphologien, die ein zunehmend begrenztes Anregungsvolumen aufweisen, untersucht. Dabei zeigt sich, dass durch den Einfluss von Grenzflächenzuständen der erwünschte Singlet Fission Prozess effizient unterdrückt wird, sollten diese Zustände von Exzitonen während ihrer Migration erreicht werden. Dieser Sachverhalt ist bei einer möglichen Realisierung von Triplet-basierter OPV zu berücksichtigen, da in Dünnschicht-Solarzellen solche Grenzflächenzustände eine relevante Rolle spielen und für Exzitonen gut zugänglich sind.

Während der oben genannte Ansatz bis jetzt nur für Modellsysteme untersucht wird, konnte die Effizienz ungeordneter organischer "bulk heterojunction" (heterogemisch, BHJ) Solarzellen in den vergangenen Jahren durch die Verwendung neuer, komplexerer Donormaterialien signifikant gesteigert werden. Allerdings war eine genaue Kenntnis der dahinter stehenden Photophysik und insbesondere der Anregungsdynamik dieser Systeme nicht vorhanden. Anhand einer systematischen optischen Studie am prominenten Copolymer PCDTBT und seiner Bausteine konnte die Natur der angeregten Zustände und deren Kopplungsmechanismus, basierend auf einem teilweisen Ladungsübertrag zwischen

zwei funktionalen Gruppen des Copolymers identifiziert werden. Die Ergebnisse der zeitaufgelösten Messungen deuten darauf hin, dass dieser interne Kopplungsmechanismus die Photophysik von organischen Solarzellen, basierend auf diesen Copolymeren bestimmt. Diese effiziente Kopplung ist ein wesentlicher Grund für den Erfolg des Copolymerkonzeptes.

Ein weiterer wichtiger Aspekt betrifft die Optimierung der Morphologie der aktiven Schicht von BHJ Solarzellen, welcher sich aus der Diskrepanz zwischen Exzitonendiffusionslänge (≈ 10 nm) und Absorptionslänge des Sonnenlichts (≈ 100 nm) ergibt. Aus diesem Grund sind auch bei BHJ Zellen, basierend auf neuartigen Copolymeren die Prozessparameter, welche die Morphologie beeinflussen — wie das Ausheizen der Zelle oder die Zugabe von Additiven — von großer Bedeutung. Unsere kombinierte optische, elektrische und morphologische Studie an Solarzellen, basierend auf dem hocheffizienten Copolymer PBDTTT-C zeigt dabei einen direkten Zusammenhang von Additivkonzentration und Durchmischungsgrad der aktiven Schicht. Das beobachtete Effizienzmaximum ergibt sich dabei für diejenige Morphologie, welche ein optimiertes Gleichgewicht zwischen Erzeugung und Transport von Ladungsträgern aufweist. Die Ergebnisse verdeutlichen, wie wichtig das Verständnis der Auswirkungen einzelner Prozessparameter auf die Morphologie und damit die Effizienz von BHJ Solarzellen ist.

Abstract

The transport of optically excited states, called excitons, as well as their conversion into charges define the two major steps allowing for the operation of organic photovoltaic (OPV) devices. Hence, a deep understanding of these processes, the involved mechanisms as well as possible loss channels is crucial for further improving the efficiency of organic solar cells. For studying the aforementioned processes spectroscopic methods like absorption and emission measurements are useful tools. As many of the processes take place on a sub-nanosecond (ns) timescale ultrafast spectroscopic methods are required. Due to this reason two experiments based on a femtosecond laser system were built and employed in this work, namely picosecond (ps) time-resolved photoluminescence (PL) and transient absorption (TA) spectroscopy.

By analyzing the PL decay dynamics in the prototypical organic semiconductor rubrene, the feasibility of a new approach for improving the efficiency of organic solar cells by harvesting triplet excitons generated by singlet fission was examined. Singlet fission describes a process where two triplet excitons are generated via a photoexcited singlet exciton precursor state if the energy of the two triplets is comparable with the energy of the singlet. For this purpose the influence of characteristic length scales on the exciton dynamics in different rubrene morphologies exhibiting an increasing degree of confinement was analyzed. The results show that the quenching at interfacial states efficiently suppresses the desired fission process if these states are reached by excitons during migration. Since interfacial states are expected to play a significant role in thin film solar cells and are easily accessible for the migrating excitons, the results have to be considered for triplet-based OPV.

While the aforementioned approach is only investigated for model systems so far, the efficiency of disordered organic bulk heterojunction (BHJ) solar cells could be significantly enhanced in the last couple of years by employing new and more complex copolymer donor materials. However, little is known about the photophysics and in particular the excitation dynamics of these systems. By carrying out a systematic optical study on the prominent copolymer PCDTBT and its building blocks we were able to identify the nature of the two characteristic absorption bands and the coupling mechanism between these levels. The latter mechanism is based on an intrachain partial charge transfer between two functional subunits and our time-resolved measurements indicate that this coupling governs the photophysical properties of solar cells based on these copolymers. The efficient coupling of functional subunits can be seen as a key aspect that guarantees for the success of the copolymer approach.

Another important issue concerns the optimization of the morphology of BHJ solar cells. It arises from the discrepancy between the exciton diffusion length

(≈ 10 nm) and the absorption length of solar irradiation (≈ 100 nm). Due to this reason, even for devices based on new copolymer materials, processing parameters affecting the morphology like annealing or employing processing additives are of major importance. In our combined optical, electrical and morphological study for solar cells based on the high-efficient copolymer PBDTTT-C we find a direct correlation between additive content and intermixing of the active layer. The observed maximum in device efficiency can be attributed to a morphology guaranteeing for an optimized balance between charge generation and transport. Our results highlight the importance of understanding the influence of processing parameters on the morphology of the BHJ and thus on the efficiency of the device.

Contents

1	Introduction	1
2	Theoretical Background	5
2.1	Organic Semiconductors	5
2.2	Radiative and Radiationless Transitions in Organic Molecules	7
2.3	Molecular Aggregates	14
2.3.1	Aggregate Picture	14
2.3.2	Exciton Transport	20
2.3.3	Excitons in Organic Crystals and Polymers	23
2.3.4	Polarons and Charge Transfer States	26
2.4	Photophysics of the Bulk Heterojunction	29
3	Experimental Section	33
3.1	Material Systems	33
3.1.1	Prototypical Organic Semiconductor Rubrene	33
3.1.2	Copolymer Donor Materials	35
3.1.3	The Fullerene Acceptor	39
3.2	Femtosecond Laser Setup	40
3.3	Time-resolved Photoluminescence Spectroscopy	42
3.3.1	Setup	42
3.3.2	SHG Stage	43
3.3.3	Streak Camera	44
3.4	Femtosecond Transient Absorption Spectroscopy	48
3.4.1	Method	48
3.4.2	Setup	52
3.4.3	Measuring Procedure	54
4	The Local Environment Affects the Exciton Dynamics in Rubrene Single Crystals	57
4.1	Singlet Fission for Organic Photovoltaics	57
4.2	Optical Sample Characterization	59
4.3	Exciton Dynamics	65
4.4	Nanocrystalline Rubrene Film	72
4.5	Summary	75

5	Excitation Dynamics in Low Band Gap Donor-Acceptor Copolymers and Blends	77
5.1	Third Generation Polymers	77
5.2	Comparative Steady State Absorption and PL Study	79
5.3	Exciton Dynamics in Copolymer Films	86
5.4	Relaxation Dynamics in Copolymer:Fullerene Blends	93
5.5	Summary	97
6	The Influence of Processing Additive on the Charge Generation in Copolymer Solar Cells	101
6.1	Copolymer Blends and the Influence of Additives	101
6.2	Solar Cell Performance	103
6.3	Optical Characterization	104
6.4	Singlet Exciton Dissociation	109
6.5	Charge Carrier Generation	112
6.6	Blend Topography	118
6.7	Summary	121
7	Conclusions	125
A	Experimental Details	133
A.1	Preparation of Thin Film Samples	133
A.2	Synthesis of PCDTBT Building Blocks	134
A.3	Femtosecond Laser Setup	135
A.4	Cryostat Holder and TA Alignment Stage	136
A.5	Streak Measurement Modes	137
B	List of Publications	139
C	Danksagung	143
D	Eidesstattliche Erklärung	147
	Literaturverzeichnis	149

CHAPTER 1

Introduction

One of the main challenges of mankind for the new millennium is to guarantee the general supply of energy. The basic issue can be summarized as follows: While the population as well as the average income grow and thus increase the demand for energy, the vast amount of primary energy supply is still based on fossil fuels. By 2030 the world population is expected to grow by 1.3 billion while, at the same time, the world income is expected to double [1]. As a result, the primary energy consumption is projected to increase by around 35 % [1, 2]. The world, however, is still depending on limited resources like oil and coal that are linked to emission of CO₂ and thus have a dramatic impact on global warming. As shown in Figure 1.1 the contribution of fossil fuels to the overall primary energy supply has only been reduced by 5.6 % compared to 1973 still yielding a contribution of more than 80 % (2010) [3]. This reduction was mainly compensated by increasing the contribution of nuclear energy. Nevertheless, due to the risks related to the operation of nuclear power plants, the storage of nuclear waste as well as its potential for military use, nuclear energy cannot be considered a long-term solution. Hence, a reasonable alternative entails promoting renewable, emission-

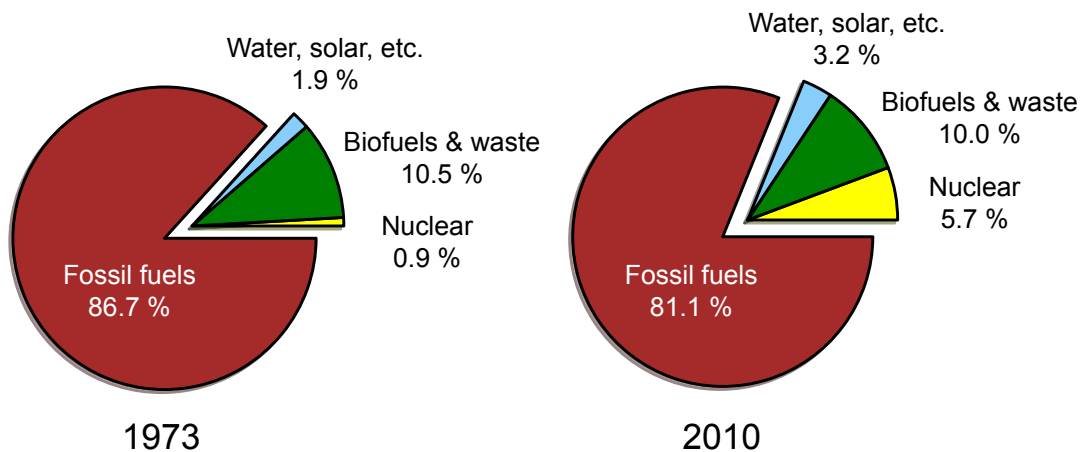


Figure 1.1: Graphs illustrating the fuel shares of the world's total primary energy supply in 1973 and 2010 [3].

neutral energies by using for example wind, water and sunlight for generating electricity.

The sun is an enormous source of energy with an average intensity of radiation reaching the earth of around 1000 W/m^2 . Using solar energy is thus considered an important component for supplying the world with renewable energy. It can be estimated that covering 0.16 % of the land with solar cells exhibiting an efficiency of 10 % would be sufficient to supply the world's expected demand on energy in 2050 [4].

The use of solar irradiation as an energy source is based on the photovoltaic effect first observed by Becquerel [5]. Upon photon absorption by a semiconductor a valence electron is promoted to the conduction band. The resulting electron-hole pair can then be separated to yield two opposite charges that can be extracted as photocurrent. Since the first silicon solar cell was presented in the early 1950s [6] much effort has been put into improving the efficiency of inorganic semiconductor-based devices. Today's silicon-based solar cells yield efficiencies of 25 % [7] which is close to the theoretical limit of 30 % estimated by Shockley and Queisser [8].

In contrast, the field of organic photovoltaics is a comparably young field of research that was initiated in 1977 when Heeger, MacDiarmid and Shirakawa discovered that the conductivity of the polymer polyacetylene can be increased by oxygen doping [9]. As indicated by the name, organic solar cell devices are comprised of carbon-based semiconducting molecules. Due to the high absorption coefficient of these molecules the active layer is comparably thin — between 100 and 150 nm. These semi-transparent layers can be put on flexible substrates by roll-to-roll printing allowing for large scale and low cost production using only little material. In general OPV is not seen as a competitive technique with respect to inorganic photovoltaics but as a complementary approach with possible applications, for example, in the area of building integration. The field of OPV can be divided into two main areas of research: devices that are based on small molecules and those that are based on polymers. Compared to small molecule devices polymer-based solar cells usually come with the general advantage of thicker active layers, i.e. superior absorption characteristics and, in addition, no processing steps under vacuum are necessary. The investigations presented in this work are based on polymer solar cells or, to be more precise on polymer-based bulk heterojunction devices. In these devices, due to the comparatively high binding energy of generated excitons, donor and acceptor molecules are blended to guarantee an efficient dissociation of the excited states. The BHJ layout has proven to be one of the most successful approaches in the field of OPV guaranteeing for an efficient conversion of excitation energy into charges while, at the same time, exhibiting good absorption characteristics.

For several years the majority of BHJ solar cells was comprised of polymer

poly(3-hexylthiophene-2,5-diyl)(P3HT) blended with the fullerene [6,6]-phenyl-C₆₁-butyric acid methyl ester (PC₆₁BM) yielding efficiencies of up to 5 % [10]. From around 2009 onwards, however, the efficiency could be increased to more than 10 % mainly by the use of new donor materials (see Figure 1.2). Exceeding the 10 % level, OPV has reached efficiencies allowing for making the step from the lab to industrial scale fabrication and commercialization. Yet, there is room for improvement regarding the device efficiency.

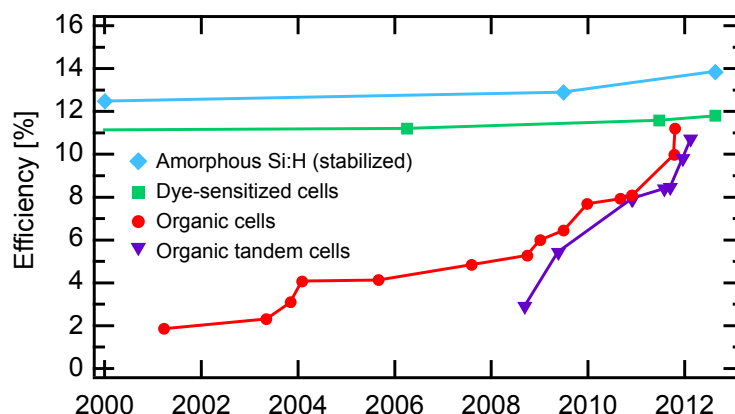


Figure 1.2: Overview of the development of the efficiencies of organic solar cells compared to amorphous silicon and dye-sensitized technologies (after Ref. [11]).

In order to make the light-to-charge conversion process more efficient it is important to understand the elementary photophysical processes following the absorption of sunlight that lead to the generation of charge carriers and to identify possible loss mechanisms. Hence, the main focus of this work is to analyze how excitation energy is distributed in organic semiconductor systems, what influences the generation of charges and how both processes can be made more efficient. As will be shown in the scope of this work, spectroscopic methods present a useful toolbox for addressing these issues. As many of the processes take place on the sub-ns to ns timescale, the methods of choice need to exhibit a very high temporal resolution. For this reason two picosecond time-resolved experimental methods implemented in this work, namely time-resolved PL and transient absorption spectroscopy, were employed. Both methods are based on a femtosecond laser system that was also built within the scope of this work. These time-resolved methods were supplemented by steady state optical characterization measurements as well as techniques to characterize the morphology of the analyzed samples.

The following chapter will start with a summary of the necessary theoretical background concerning organic semiconductors and their interaction with light.

In the third chapter, the investigated material systems are introduced and the experimental setups are described. Afterwards the results are presented and extensively discussed.

Theoretical Background

This chapter gives a summary of the theoretical background that is important for the discussion of the results presented later on in this thesis. The experimental methods used in this work are predominantly based on photophysical tools with a focus on time-dependent techniques. Thus, after a short introduction of the material class of organic semiconductors, the interaction of light with organic molecules will be discussed in more detail. The subsequent section presents a theoretical description of the excited states as well as their dynamics within aggregates of organic molecules, relevant for organic crystals as well as polymeric systems. These paragraphs are mainly based on the books by Pope and Swenberg as well as Turro, Ramamurthy and Scaiano [12, 13]. Finally the fundamental photophysical processes that follow the excitation of an organic blend system used for photovoltaics are summarized applying the principles and mechanisms discussed in the preceding sections. A more detailed discussion of the fundamental physics behind organic solar cells can be found, for example, in the reviews by Brabec et al. [14] and Deibel et al [15].

2.1 Organic Semiconductors

As indicated by the word *organic* this class of semiconductors describes compounds based on carbon that may also contain other “organic elements” such as hydrogen or oxygen. As carbon is the main building block it governs the properties of organic semiconductors. Being the sixth element in the periodic table its ground state electronic configuration is $1s^2 2s^2 2p^2$ [16]. Carbon atoms can form molecules with other carbon or non-carbon atoms upon the overlap of the respective electronic wave functions which are combined to molecular wave functions, while the electrons from each atom are distributed among the new molecular orbitals. This mechanism can be qualitatively described by the Molecular Orbital approximation which is based on the linear combination of atomic orbitals [12, 17].

The existence of organic semiconductors is based on the fact that carbon atoms can undergo a so-called hybridization: The 2s- and 2p-orbitals can mix to form a set of equivalent and thus degenerate orbitals. In one possible configuration called sp^2 hybridization, the 2s mixes with the $2p_x$ and $2p_y$ to form

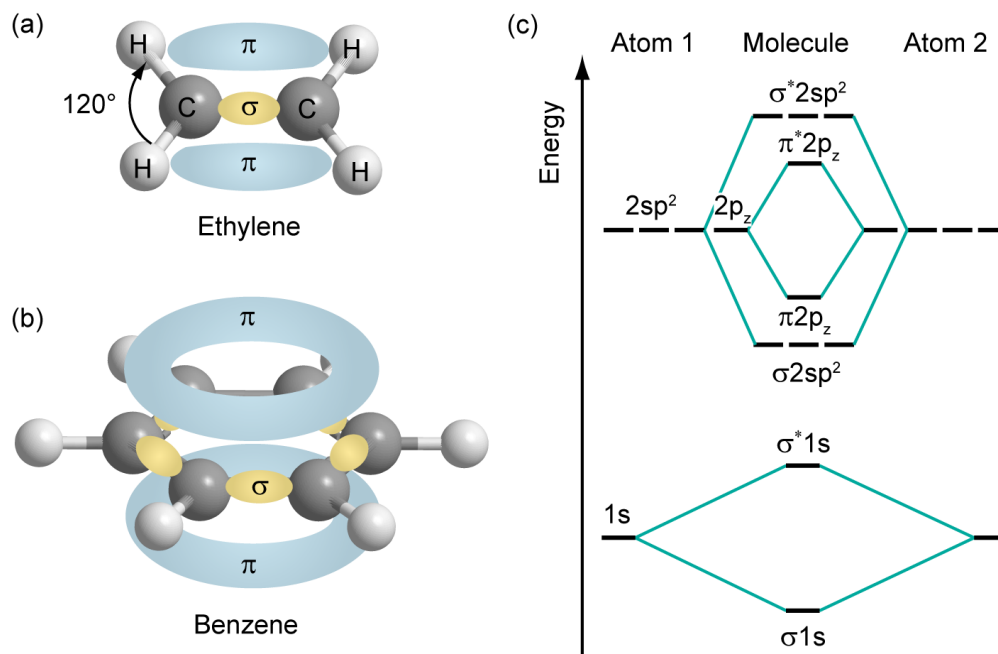


Figure 2.1: Molecular structures of ethylene (a) and benzene (b) with schematically drawn σ and π bonds. (c) Resulting energy levels of two bond sp^2 -hybridized carbon atoms.

three sp orbitals which are coplanar and directed about 120° apart from each other (see Figure 2.1 (a)). These orbitals can form σ -bonds with other atoms in which electrons are localized between the two binding partners. The $2p_z$ orbital remains unaltered and aligns perpendicular to the plane of hybridization. When connecting two carbon atoms, the $2p_z$ orbitals of the atoms form a π -bond in addition to the σ -bond resulting in a double bond between both atoms. As can be seen for the ethylene molecule depicted in Figure 2.1 (a) the resulting π -orbitals establish a delocalized electron density above and below the plane of the carbon atoms. Linking carbon atoms to a chain or ring as in benzene (Figure 2.1 (b)) one can create an extended delocalized π -electron system which is crucial for charge transport. As there is one electron per $2p_z$ orbital, the resulting molecule exhibits alternating single and double bonds and therefore is called *conjugated*. At this point it has to be mentioned that, for example, in benzene the sites of the double bonds are not fixed but that there are two different arrangements that equally contribute to the binding of the atoms in the ring. Molecules built from these rings such as anthracene or tetracene are called *aromatic* due to the odor of the natural compounds in which they are found.

The resulting orbitals of the molecule are created by the interaction of the

2.2. Radiative and Radiationless Transitions in Organic Molecules 7

respective atoms [16], as schematically shown in Figure 2.1 (c) for two sp^2 -hybridized carbon atoms. For molecules such as benzene the resulting highest occupied (HOMO) and lowest unoccupied molecular orbitals (LUMO) are π and π^* -orbitals, respectively. Therefore the fundamental optical and electrical properties of conjugated organic molecules are due to processes involving these π -electrons while the other electrons attribute to the bonds between atoms. The number of energy levels with π -character is directly proportional to the number of incorporated carbon atoms so that in larger conjugated molecules or polymers a band-like structure of closely spaced energy levels is created (see section 2.3).

Since double bonds are generally slightly shorter than single bonds, an additional bandgap between the fully occupied HOMO and the LUMO is being introduced by the Peierls-instability [16]. This bandgap manifests the semi-conducting character of the organic molecule in which the HOMO can be seen equivalent to the valence and the LUMO equivalent to the conduction band. In contrast to inorganic semiconductors, where the material itself consists of single covalently bound atoms, organic semiconductor materials consist of individual organic molecules held together by comparatively weak van der Waals forces. The collective properties of these semiconductor systems thus critically depend on the degree to which the π -electron systems of adjacent molecules interact with one another.

2.2 Radiative and Radiationless Transitions in Organic Molecules

The simplest model system for studying the interaction of light and matter is to assume a two-level atom (Figure 2.2 (a)). As electrons are spatially well confined in these systems they absorb photons of well-defined energies when illuminated with a spectrum of light. By absorbing a photon an electron is promoted to the excited atomic state ($S_0 \rightarrow S_1$). After a certain time, neglecting radiationless transitions for now, the electron relaxes back to the ground state and a photon with an energy $h\nu = E_1 - E_0$ is emitted. The resulting absorption and emission spectra exhibit sharp lines when measured at low pressure in the gas phase [13]. The energetic levels involved are called electronic levels with associated transitions in the ultraviolet to visible region of the electromagnetic spectrum at a couple of electron volts (eV). These transitions dominate the absorption and photoluminescence (PL) spectra of both atoms and organic molecules [12].

Due to the additional degrees of freedom, molecules exhibit characteristic vibrational and rotational motions that manifest themselves as energetic sublevels (vibrational sublevels ν and rotational sublevels r in Figure 2.2 (b)). Vibrational energies are of the order of 1000 cm^{-1} ($\approx 0.1 \text{ eV}$) in the near infrared

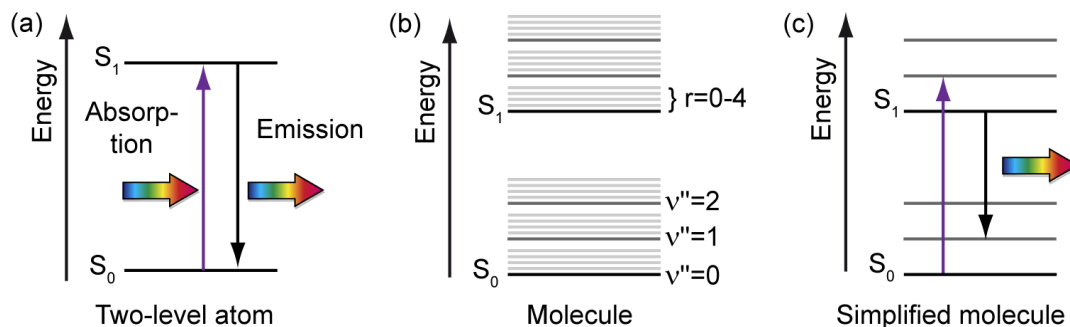


Figure 2.2: (a) Energy level representation of the interaction of light with a two-level system. (b) The additional rotational and vibrational degrees of freedom of a molecule result in additional energetic sublevels (ν, r). (c) Simplified representation of a molecule in the energy level diagram.

(IR) region while typical rotational energies are in the far IR ($\approx 10 \text{ cm}^{-1}$) and in general cannot be resolved by experiments in the liquid or solid phase [12]. In principle there is a large number of vibrational modes for a given molecule, however, many vibrational transitions are too weak to be resolved. Therefore it is often sufficient to assume one prominent vibrational mode and its progression ($\nu = 0, 1, 2, \dots$) in order to describe absorption and emission spectra of organic molecules (Figure 2.2 (c)). The vibrational sublevels themselves are energetically broadened by the presence of additional vibrations and thermal fluctuations as well as morphological inhomogeneities resulting in different local environments in the case of solids. It is important to mention that in contrast to an atom, the electronic transitions within a molecule are rather considered to be of *vibronic* nature due to the coupling between electrons and phonons. A result is that the sharp lines in absorption and PL as observed for an atom are replaced by a set of closely spaced lines.

In principle the properties of a molecular system can be deduced if the wave function representing it is known. This wave function can be obtained from solving the stationary Schrödinger equation,

$$\hat{H}\Psi = E\Psi, \quad (2.1)$$

where \hat{H} is the Hamiltonian operator and Ψ the wave function. As mentioned before both Hamiltonian and wave function contain electronic contributions as well as contributions from the nuclei. If the adiabatic Born–Oppenheimer approximation is valid the wave function of the molecule can be written as

$$\Psi_m = \psi_{el} \psi_\nu \psi_r \psi_s, \quad (2.2)$$

2.2. Radiative and Radiationless Transitions in Organic Molecules 9

with corresponding energies

$$E_m = E_{el} + E_\nu + E_r + E_s . \quad (2.3)$$

Here the subscripts el , ν and r refer to the electronic, vibrational and rotational contributions, respectively and s denotes the contribution by the electron spin. This approximation makes use of the fact that the masses of electrons and nuclei differ significantly so that electrons can be considered to respond instantaneously to changes of the nuclei configuration. The probability R of an optical transition between an initial state i and a final state f in dipole approximation can be calculated from the absolute square of the transition dipole element \mathbf{M}_{if} :

$$R_{if} \propto |\mathbf{M}_{if}|^2 = |\langle \Psi_i | \mathbf{p} | \Psi_f \rangle|^2 , \quad (2.4)$$

where \mathbf{p} is the dipole operator which is the quantum mechanical analogon and directly proportional to the classical oscillator strength which describes the interaction of an electron with an electric field [13]. Inserting equation (2.2) into (2.4) gives

$$R_{if} \propto |\langle \psi_{el_i} | \mathbf{p} | \psi_{el_f} \rangle|^2 |\langle \psi_{\nu_i} | \psi_{\nu_f} \rangle|^2 |\langle \psi_{r_i} | \psi_{r_f} \rangle|^2 |\langle \psi_{s_i} | \psi_{s_f} \rangle|^2 . \quad (2.5)$$

The different parts of this equation again depict the electronic, vibrational, rotational and spin contributions. The dipole operator only appears in the first term since nuclei cannot respond rapidly enough to the optical frequencies and spins are insensitive to electric fields. If any of the terms in equation (2.5) is zero, the probability of the transition is zero and is called a dipole forbidden transition.

Considering the case of absorption of a photon (spin-allowed transition) while excluding the rotational contributions which in general cannot be spectrally resolved and do not play a role in solid state, equation (2.5) is reduced to

$$R_{if} \propto |\langle \psi_{el_i} | \mathbf{p} | \psi_{el_f} \rangle|^2 |\langle \psi_{\nu_i} | \psi_{\nu_f} \rangle|^2 \propto T_{FC} |\langle \psi_{el_i} | \mathbf{p} | \psi_{el_f} \rangle|^2 . \quad (2.6)$$

with T_{FC} , the Frank-Condon factor, comprising the vibrational contributions. As the dipole operator is of odd symmetry, the initial and final electronic state wave functions must be of opposite symmetry otherwise the transition is forbidden. Applying the Born–Oppenheimer approximation the potential of the configuration of nuclei for a given electronic state can be described by a potential energy surface. As an electronic transition takes place in around 10^{-15} s and is thus much faster compared to nuclear motions with about 10^{-13} s, both processes can be assumed to be decoupled [12]. This is the basic idea behind the so-called Frank–Condon principle. As a result, the electronic transitions between the ground and excited state are vertical. At room temperature the thermal excess energy (25 meV) is much smaller than the typical energetic spacing between

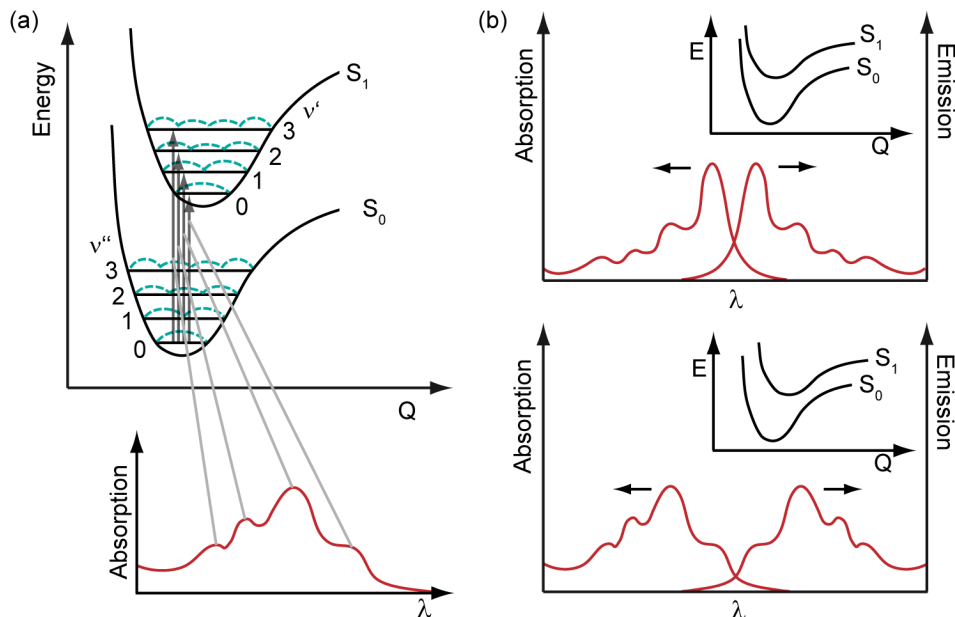


Figure 2.3: (a) Potential energy surface scheme illustrating the electronic transitions between the ground and first excited state of a molecule (after [12]). (b) The relative heights of the absorption peaks depend on the degree of overlap between the vibrational wave functions of the involved transitions. For a small displacement (upper graph) the $0 \rightarrow 0$ transition dominates, while for a significant displacement (lower graph) it shifts to higher-energetic transitions (after [13]).

vibronic levels so that it can be assumed that absorption to the vibronic levels of the excited states always takes place from the $\nu = 0$ vibrational level of the ground state (see Figure 2.3 (a)). The promotion of an electron to an excited state is tantamount to the redistribution of electronic density and involves changes in the molecular structure, i.e. the internuclear distances, for example due to alteration of the bonding length. Therefore the distance between the nuclei in the ground and excited state, denoted with the configuration coordinate Q is different. The probability of absorption from the electronic ground state into the different vibronic levels of the excited states is defined by T_{FC} and scales with the degree of the overlap between the vibrational wave functions of the involved energetic levels. If the horizontal displacement of the potential curves is small, such as for instance in anthracene [13], the $0 \rightarrow 0$ band is quite strong ($\nu'' = 0 \rightarrow \nu' = 0$). For significant displacements of the excited state potential curves, the spectral weight shifts to higher-energetic bands (see Figure 2.3 (b)). In general, a larger displacement Q is assumed for the excited state because the equilibrium geometry is expected to be larger in that state compared to the

2.2. Radiative and Radiationless Transitions in Organic Molecules 11

ground state [13].

After excitation of the molecule to an upper vibronic level the electron rapidly relaxes back to the $\nu' = 0$ level of the electronically excited state. In solids this process is much faster than the radiative transition to the ground state so that — in accordance with Kasha’s rule [18, 19] — emission will in general take place from the lowest excited state. The emitted photon is characteristically of longer wavelength and the energetic redshift between absorption and emission is called Stokes shift. As the Frank–Condon principle can also be applied to the reverse process, i.e. relaxation of an electron to the ground state, the emission spectrum is a mirror image of the absorption spectrum (see Figure 2.3 (b)). If the vibronic features in absorption and emission spectra can be spectrally resolved, the progression in absorption shows the vibrational structure of the excited state and vice versa.

Considering the electron spin one has to differentiate between singlet state transitions ($S_0 \rightleftharpoons S_n$) and those involving triplet states ($S_n \rightleftharpoons T_n$). Because of the Pauli exclusion principle two electrons with parallel spins cannot occupy the same molecular orbital, but are in different orbitals. This leads to a reduced electron–electron repulsion and, thus, a reduction of the energy of the excited triplet state compared to the singlet state (Figure 2.4 (a)). Consequently, emission from a triplet state, called phosphorescence (associated rate k_{Ph}), is redshifted with respect to singlet emission, which is called fluorescence (k_F). Processes in which the spin multiplicity is changed such as $S_0 \rightleftharpoons T_n$ or $S_1 \rightarrow T_1$ are formally spin-forbidden but can still be observed as the electronic orbital wave functions of, for example, T_1 and S_0 or S_1 and T_1 mix. These processes are called inter-system crossing (ISC) and the associated rates strongly depend on the magnitude of the spin-orbit coupling in the molecule. The coupling in turn is stronger for heavier atoms [13, 20, 21] and also depends on the resonance between the energetic levels that mix ($S_1 \rightarrow T_1$) [13]. The rates for spin-forbidden radiative electronic transitions in organic molecules are in general much smaller ($10^{-1} - 10^4 \text{ s}^{-1}$) than rates for spin-allowed transitions ($10^5 - 10^9 \text{ s}^{-1}$) resulting in longer triplet excited state lifetimes compared to singlet lifetimes [13]. As singlet and triplet excited states are coupled by the ISC process, the fluorescence efficiency depends on the ratio between the rates of radiative decay from the excited singlet state k_F and the ICS rate k_{ISC} and the resulting ratio differs a lot depending on the type of organic molecule.

In special cases, where the first excited singlet exciton energy level is close to twice the energy of the first excited triplet state, a singlet exciton can decay into two triplet excitons (Figure 2.4 (a)). This process is called singlet fission (SF). It is spin-allowed, as the two resulting triplet states are effectively created via the singlet precursor state. It can be described as a molecule excited to the first excited singlet state (1) sharing its energy with a neighboring molecule by

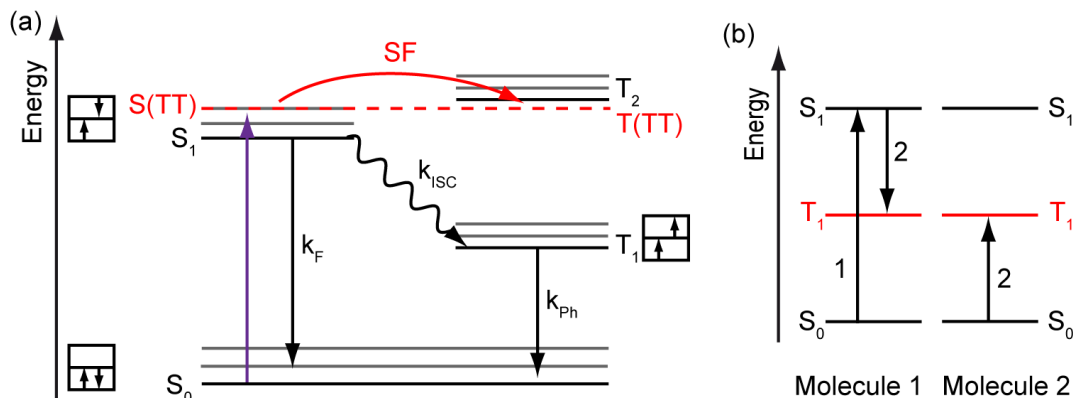


Figure 2.4: (a) First excited electronic levels of a molecule considering the electron spin resulting in a singlet (S) and triplet (T) manifold. Possible transitions between S and T states as well as decay channels are indicated by the corresponding rates k . (b) Energy scheme illustrating the singlet fission process (after [22]).

spin dipole-dipole interaction (2) thus creating two triplets (see Figure 2.4 (b)). If the process is isoenergetic or even exoergic and the coupling is strong, such as in organic crystals, singlet fission can occur on the picosecond to sub-picosecond scale even competing with vibrational relaxation [22]. If the two triplets can diffuse apart rapidly, as in crystals and polymers, they can be described as individual triplet excitons. If not, they destroy each other forming a singlet or higher excited triplet (triplet fusion). In most cases fission takes place from the lowest energetic level of S_1 and involves thermal activation or the release of excess energy, but it can also be a “hot” process meaning that it occurs from a higher vibrational level of S_1 . As hot fission in general has to compete with the efficient internal relaxation within S_1 it is usually not very efficient [22].

Even when both fluorescence and phosphorescence of an organic molecule are measured simultaneously, the resulting total radiative quantum efficiency in general is below unity. Apparently there are radiationless processes that “compete” with the radiative transitions to the ground state. In principle one can divide radiationless transitions into two categories, namely intramolecular relaxation and dissociation or ionization of the molecule. Considering the first case — ionization of organic molecules will be discussed in section 2.3.4 — intramolecular radiationless transitions can be characterized by the so-called internal conversion (IC) as well as ISC processes. IC describes all energetic relaxations between different electronic levels (e.g. $S_2 \rightarrow S_1, S_1 \rightarrow S_0$) or different vibrational levels of the same electronic level (e.g. $S_1 : \nu_3 \rightarrow \nu_0$) within the same spin multiplet

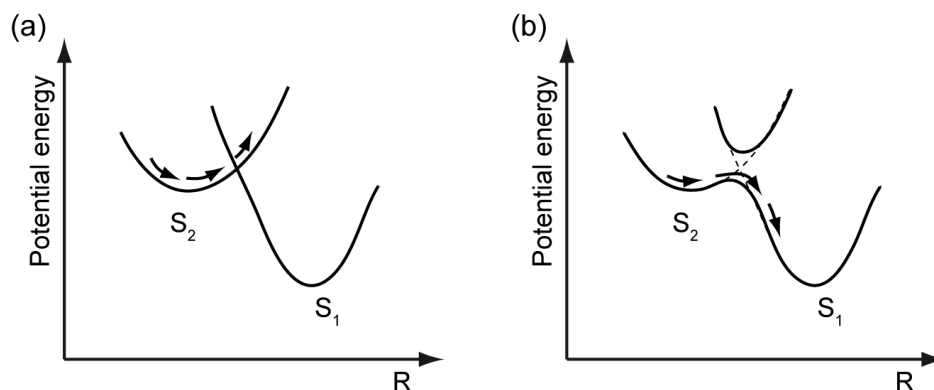


Figure 2.5: The potential energy surfaces representing different electronic interactions and, for example, cross (a) or avoid (b) each other (after [13]). For the latter case an electron from the higher energetic level can undergo a radiationless transfer to the lower electronic state called internal conversion. The excess energy of the electron is converted into vibrational energy of the system. The value R is the reaction coordinate.

— i.e. singlet or triplet states. In contrast, as described above, the ISC is a process involving the transitions between both spin manifolds. Analogous to the discussion of the Frank–Condon principle, radiationless processes can in general be discussed by describing the energy levels involved with associated electronic potential energy surfaces and analyzing the motion of a “representative point” indicating the nuclear configuration that determines the electronic distribution. These potential surfaces can interact, for example cross each other (Figure 2.5 (a)), and in certain cases an electron from a higher lying excited state S_2 can be transferred to S_1 (Figure 2.5 (b)), while the excess energy is dissipated by the coupling to intra- and/or inter-molecular vibrations. As the transition is accompanied by the change of the nuclear geometry of the organic molecule, vibronic modes also mediate the conversion process itself and certain vibrational modes can even promote radiationless transitions [13]. Therefore, for efficient IC between two energetic states the availability of a variety of suitable vibronic states, provided for example by the interaction with other molecules is essential to guarantee for an efficient conversion [12]. Further explanations and examples dealing with the theory of potential energy surfaces can be found in literature [13, 23, 24].

As already introduced in the context of the Stokes shift, all photophysical processes usually start from the lowest vibrational level of the S_1 or T_1 in accordance with Kasha’s rule [18, 19]. In agreement with this rule the IC rates for

both $S_{n>1} \rightarrow S_1$ as well as $S_{n \geq 1} : \nu \geq 1 \rightarrow \nu = 0$ transitions are in general of the order of $10^{11} - 10^{13} \text{ s}^{-1}$ and $10^{12} - 10^{14} \text{ s}^{-1}$, respectively and thus much larger than those for the radiative transitions from these states [13]. For transitions from $S_1 \rightarrow S_0$ the ratio between IC and radiative decay depends on the rigidity of the molecule, the presence/absence of vibrational modes inducing radiationless transitions and the energy gap ΔE between the potential minima of the states involved, as the rate for IC k_{IC} is found to be proportional to $e^{-\alpha \Delta E}$ [13]. The radiative and radiationless transitions discussed for organic molecules in this section are summarized in Figure 2.6.

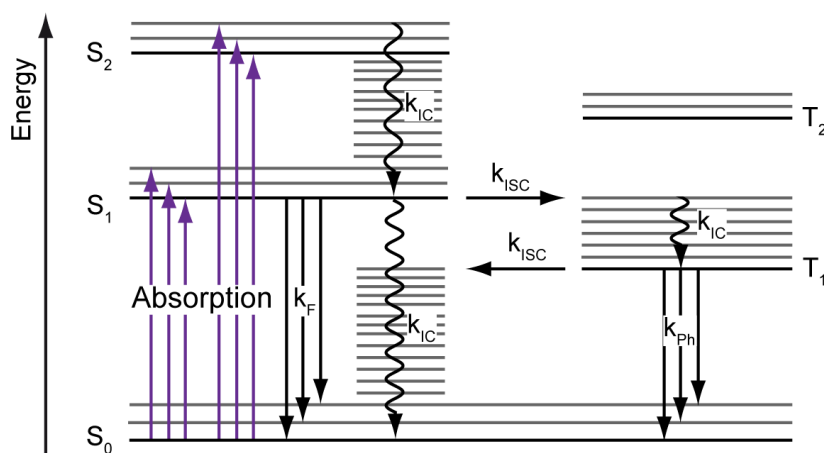


Figure 2.6: Energy level scheme summarizing the possible relaxation pathways of an optically excited molecule. The relevant decay mechanisms are represented by the respective rates k (after [12]).

2.3 Molecular Aggregates

2.3.1 Aggregate Picture

So far, the absorption and emission of an isolated single organic molecule was described. Now the discussion will be focused on the excited states of molecular aggregates. This and the following section will predominantly deal with excitations of the singlet manifold and the possible relaxation pathways. In this context the ISC process towards the triplet state will be treated as a possible radiationless decay mechanism. Due to the weak binding forces between the organic molecules in an aggregate — usually they are held together by van der Waals forces — many spectroscopic properties can be retraced to the individual

molecular properties, such as vibronic “fingerprints”. However, the interaction between the molecules gives rise to spectral changes and new features and the high periodic order of organic crystals even justifies a band approach in analogy to inorganic semiconductor theory. In respect thereof, several optical and electrical properties of organic semiconductors can be discussed in terms of a molecular or band-like approach [25].

The intermolecular coupling present in molecular aggregates motivates the description of excited states of this system as quasi-particles called excitons as initially introduced by Frenkel in 1931. An exciton describes a coulombically bound electron-hole pair which can be semi-classically described as a hydrogen-like complex with an approximated binding energy of [20]:

$$E_{exc} = -\frac{Z^2 e^4 m_0}{32(\pi \epsilon_0 \hbar)^2 \epsilon_r} \cdot \frac{1}{n^2}, \quad (2.7)$$

with Z being the atomic number, e the elementary charge, m_0 the electron mass, ϵ_0 the dielectric permeability, \hbar the reduced Planck constant, ϵ_r the dielectric constant of the medium and n the quantum number. As the dielectric constant in organic materials is relatively small (≈ 3) [26] the electrons and holes are tightly bound with binding energies up to 1 eV as for anthracene crystals [27]. In addition, the structural relaxation of the excited state compared to the ground state, as observed for polymers, contributes to the relatively high exciton binding energy [28]. The type of exciton is called Frenkel exciton and both electron and hole can be assumed to be located at the same molecular site. In contrast an exciton with electron and hole being delocalized over several neighboring repeating units is called Wannier–Mott exciton and is most common in inorganic semiconductors, where the dielectric constant is much higher.

The simplest example of an interacting molecular system is the physical dimer. In contrast to the chemical dimer, where identical molecules are connected by chemical bonds, the term physical dimer refers to the case where these molecules are just close together but do not form a chemical bond. Applying a simplified quantum mechanical approach the important spectroscopic changes that result from aggregation can already be studied for this dimer. The Hamiltonian for such a system can be written as

$$\hat{H} = \hat{H}_1 + \hat{H}_2 + \mathbf{V}_{12}, \quad (2.8)$$

where $\hat{H}_{1,2}$ denote the Hamiltonians for the isolated molecules and \mathbf{V}_{12} the intermolecular interaction. Ignoring vibrational and spin contributions, the overall electronic wave function of the dimer ground state can be expressed as

$$\Psi_g = \Psi_1 \Psi_2, \quad (2.9)$$

with $\Psi_{1,2}$ being the ground state wave functions of the two molecules. Hence the ground state energy is given by the following equation:

$$E_g = E_1 + E_2 + \langle \Psi_1 \Psi_2 | \mathbf{V}_{12} | \Psi_1 \Psi_2 \rangle . \quad (2.10)$$

The last term in equation (2.10) depicts the additional coulombic binding energy of the molecule W which is negative. As Ψ_g is not an Eigenfunction of \hat{H} due to the presence of \mathbf{V}_{12} in principle an improved ground state wave function would have to be obtained considering the configuration interaction. For reasons of simplicity this fact is neglected. The lowest-lying excited dimer state is assumed to be the result of interaction of equivalent non-degenerate excited state levels of both molecules. Since the two molecules are identical, both combinations $\Psi_1^* \Psi_2$ and $\Psi_1 \Psi_2^*$, where * denotes the excited state, have in principle the same energy and the excitation is localized on one of the molecules. Considering the intermolecular interaction results in the coherent oscillation of excitation energy between both molecules – they are said to be excitonically coupled. This sharing of energy is expressed in the excited state wave function by a linear combination of the non-interacting states:

$$\Psi_e = a_1 \Psi_1^* \Psi_2 + a_2 \Psi_1 \Psi_2^* . \quad (2.11)$$

The two molecules are identical and so the excited state energy for the dimer becomes

$$E_{\pm} = E_1^* + E_2 + \langle \Psi_1^* \Psi_2 | \mathbf{V}_{12} | \Psi_1^* \Psi_2 \rangle \pm \langle \Psi_1^* \Psi_2 | \mathbf{V}_{12} | \Psi_1 \Psi_2^* \rangle , \quad (2.12)$$

where the third term is the coulombic interaction W' between the excited state of molecule 1 and the ground state of molecule 2 and the fourth term depicts the resonance interaction energy β . The corresponding excited states are

$$\Psi_{E_{\pm}} = \frac{1}{\sqrt{2}} (\Psi_1^* \Psi_2 \pm \Psi_1 \Psi_2^*) . \quad (2.13)$$

It has to be mentioned that the wave functions in general have to be antisymmetrized by adding electron exchange terms to fulfill the Pauli exclusion principle. As shown in Figure 2.7 the excitonic coupling of the molecules leads to a shift of ground and excited state energies (W, W') and a splitting of the excited state level into two levels separated by $2|\beta|$. The net shift of the absorption or PL spectrum depends on the magnitudes of W, W' and the relative orientation of the transition dipole moments of the molecules, i.e. the relative orientation of the molecules, as schematically shown in Figure 2.7. For a so-called H-aggregate, where the molecules are oriented so that their dipole moments are parallel to each other, only transitions from the higher lying excited state are dipole-allowed

(blueshift) as for the lower lying level the transition dipoles are antiparallel and thus cancel. The opposite, namely a redshift can be observed for J-aggregates, where the transition dipoles are oriented in line and now the dipole moments for the higher lying energy level of the dimer cancel. For an oblique orientation of both molecular transition dipole moments both transitions are allowed.

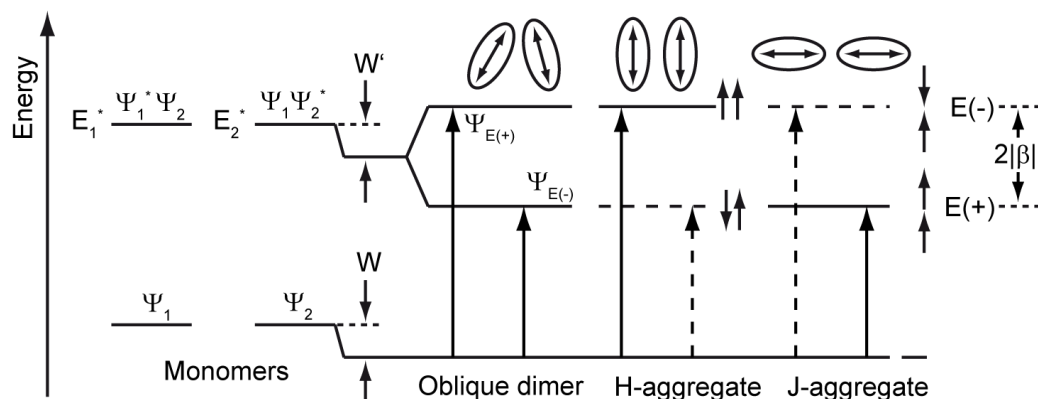
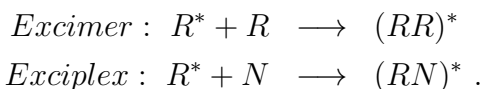


Figure 2.7: The interaction of two identical organic molecules represented by two-level systems results in the energetic shift of the levels (W, W') and a splitting of the excited state into two levels E_{\pm} separated by $2|\beta|$. The optical properties of the dimer depend on the relative orientation of the dipole moments of both monomers, indicated by the arrows (after [12]).

In addition to the dimer there is a second type of complex which is excitonically coupled in the excited state, but dissociated in the ground state. This complex is called an excimer if both molecules are identical or exciplex if both molecules involved are different:



Here * again denotes that the molecule or complex is in the excited state. As W is repulsive, the two molecules are only bound in the excited state, showing the typical broad and structureless PL [12] while the absorption spectrum is that of the isolated molecule. For the formation of an excimer or exciplex an excited molecule has to be close to another molecule in the ground state. Excimers can be formed for example by the collisions of molecules in solution and also appear in organic crystals such as pyrene or perylene [12].

In accordance with the theoretical description of the coupling between two molecules the excitonic coupling concept can be extended towards one-

dimensional (polymers) and bulk organic crystal structures. Assuming a one-dimensional crystal with only nearest neighbor interaction then the first excited state energy is split into N states, where N is the number of molecules in the crystal (Figure 2.8 (a)). For an infinite array of molecules the excited state becomes a band of states, called exciton band, and the excitation that is initially located at a single molecular site is spread among all the molecules. The excited state electronic wave function can again be described by a linear combination of the unperturbed single excited state configurations of the system. The exciton wave functions then result from minimizing the energy of the excited state applying the variation principle. For periodic boundary conditions the resulting energy band for a linear crystal as a function of the wavenumber $k = 2\pi/\lambda$ is shown in Figure 2.8 (b). Here β is the interaction energy between neighboring molecules. Due to the exciton binding energy the energetic gap (HOMO-LUMO gap) of the excited molecular site of the crystal is smaller compared to the “neutral” environment. In a band picture, where the valence band is representing the HOMO and the conduction band the LUMO levels of the unperturbed molecular sites, this phenomenon gives rise to excitonic band gap states as indicated in Figure 2.8 (c) [15, 25, 26].

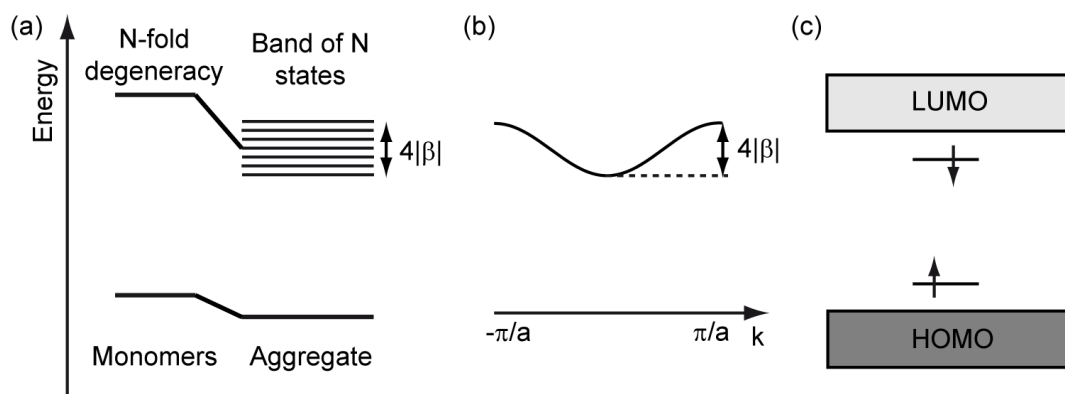


Figure 2.8: (a) The coupling of N identical molecules leads to a band of N states for the excited state of the aggregate. (b) For an organic crystal the excited state can be described applying the formalisms of band theory known from inorganic semiconductors ((a), (b) after [12]). (c) The exciton can then be described by an electronic gap state.

If the unit cell of an organic crystal exhibits one or more translationally inequivalent molecules the excited state band splits into a number of subbands that equals the number of inequivalent molecules (Figure 2.9). The splitting is named after Davydov who first applied exciton theory to organic crystals and

showed this phenomenon [29]. It originates from the inequivalent interaction between the molecules in the unit cell and its magnitude varies from a few hundred to several thousand cm^{-1} (few tenth to several hundreds of meV). Due to the different relative molecular orientations that give rise to the different Davydov bands, the polarization properties also differ between the bands [12].

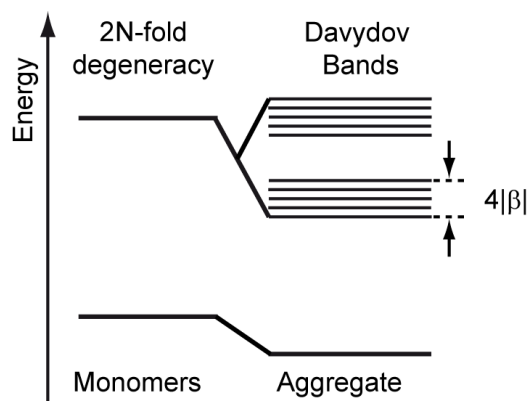


Figure 2.9: Scheme showing the qualitative Davydov splitting of the excited state band for a molecular crystal exhibiting two translationally inequivalent molecules in its unit cell (after [12]).

The typical effects of aggregation of organic molecules on the absorption and PL spectra can be summarized as follows:

- Energetic displacement of absorption and emission bands with respect to those of the single molecule
- Broadening of lines due to intermolecular electronic and vibrational interaction of the molecules
- Changes in molecular vibrational frequencies and the rise of new intermolecular lattice modes
- Change of oscillator strength of optical transitions
- Splitting of spectral lines with additional change of the polarization properties.

In addition, the energy levels of a real organic semiconductor system might be further broadened by the influence of inhomogeneities in the form of local disorder and/or chemical impurities as well as conformational variations as for polymers. Therefore usually just vibrational progressions of prominent vibrational modes like the 1400 cm^{-1} ($\approx 170 \text{ meV}$) breathing mode can be spectrally resolved.

2.3.2 Exciton Transport

The transport of excitation energy in organic semiconductors can be described in the exciton picture as the migration of these quasi-particles. Initially, after excitation of the molecular aggregate, the molecules within the excited domain inhibit a correlated phase relationship. Due to the coupling between neighboring molecules the excited region, i.e. the exciton, is now free to move along the aggregate. If the phase relationship is preserved the exciton is called coherent and it moves in a wave-like manner. In real organic molecular systems, due to inhomogeneities and interactions with phonons the coherent character described by the coherence time τ_C , remains only for a very short time of usually much less than 10^{-13} s [12]. After τ_C the exciton can be assumed to be localized at a certain site of the aggregate, for example a single molecule, and moves incoherently by jumps between neighboring sites.

The simplest mechanism for the transfer of excitation energy is the reabsorption of a photon emitted from the excited region by another region in the aggregate, called self-absorption. This process, however, occurs only for the small part of the emission spectrum that spectrally overlaps with the absorption of the molecule and becomes relevant only for larger distances of typically more than 10 nm [12]. A more general, widely applied concept for explaining and modeling exciton migration is the Förster or resonant energy transfer [30] model. It describes the transfer of energy from a donor molecule (D) to an acceptor molecule (A), which is in close vicinity (few nm), mediated by dipole–dipole interaction. In accordance with the dimer-problem it can in principle be considered as a coherent coupling leading to a coupled wave function in the form of

$$\Psi_{DA} = c_1 \Psi_A^* \Psi_D + c_2 \Psi_A \Psi_D^* , \quad (2.14)$$

with $\Psi_{D,A}$ denoting the donor and acceptor electronic wave functions, respectively. In this case the excitation energy oscillates between D and A with a frequency proportional to the coupling strength J and the rate for a transition from D to A was calculated by Perrin as:

$$k_{D \rightarrow A} = \frac{4|J|}{\hbar} \propto \frac{1}{R^3} . \quad (2.15)$$

Here R is the separation between donor and acceptor and $k_{D \rightarrow A}$ is proportional to $1/R^3$ because of the dipole–dipole interaction. This equation is only valid in the strong coupling limit, where the coupling $|J|$ is much stronger than the vibrational bandwidth ΔE of the acceptor. In practice, however, $\Delta E > |J|$ and the strong electron–phonon coupling leads to an efficient relaxation within the excited state of the acceptor, destroying the coherence and making the transfer of energy an irreversible process. In this so-called weak-coupling limit the energy

transfer rate can be written as

$$k_{DA} = \frac{1}{\tau_D} \left(\frac{R_0}{R} \right)^6, \quad (2.16)$$

with τ_D being the lifetime of the donor exciton, R_0 the Förster or critical radius and R the donor–acceptor distance. R_0 is the distance at which the transfer from donor to acceptor is equal to the radiative decay rate and it critically depends on the spectral overlap of donor emission and acceptor absorption spectra as well as the relative orientation of the dipole moments:

$$R_0^6 = \frac{3}{4\pi} f \int \frac{c^4}{\omega^4 n_0^4} F_D(\omega) \sigma_A(\omega) d\omega, \quad (2.17)$$

where $F_D(\omega)$ is the normalized fluorescence spectrum, $\sigma_A(\omega)$ the normalized absorption cross section and f describes the orientation of the transition dipole moments. The transfer of excitation energy from the donor towards the acceptor can be seen as the absorption of a virtual photon emitted by D exciting an electron of A (see Figure 2.10). As mediated by dipolar interaction, the Förster transfer is efficient over distances of a few nanometers [13]. Another form of resonant energy transfer is the so-called Dexter transfer [31] describing dipole-forbidden transitions by multipole interaction and electron exchange interactions (Figure 2.10). As these processes require the interaction of the molecular electronic orbital wave functions the range of the Dexter mechanism is in the sub-nanometer to nanometer range [13].

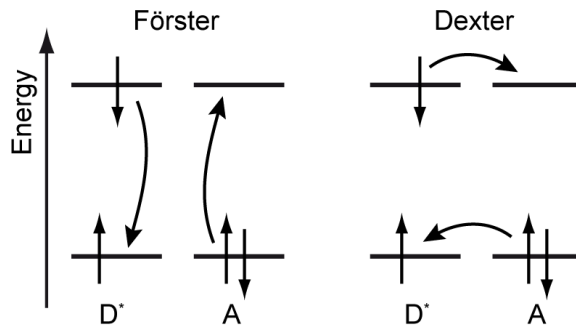


Figure 2.10: Energy scheme depicting the transfer of excitation from a donor (D) towards an acceptor (A) molecule. While the Förster mechanism is based on dipole–dipole interactions, the Dexter mechanism describes electron exchange and multipole interactions.

If an exciton encounters an inhomogeneity within the organic semiconductor, for example structural defects within the crystal or chemical impurities, these defects can act as lower-lying energetic sites trapping the exciton. The exciton

can subsequently decay to the ground state or be promoted to the first excited state again, for example by thermal excess energy of the system (Figure 2.11 (a)). The latter process is called exciton scattering. An exciton approaching an interface of the organic semiconductor can also get trapped, if the excited state energy of the surface molecule is below the “bulk level”, otherwise it is reflected (Figure 2.11 (a)). The existence of these surface states is a result of the breaking of symmetry and the missing neighboring molecules lead to a different shift of the surface molecules energy levels compared to the bulk molecules. The energetic position of the “surface level” with respect to the “bulk level” in general depends on the material system.

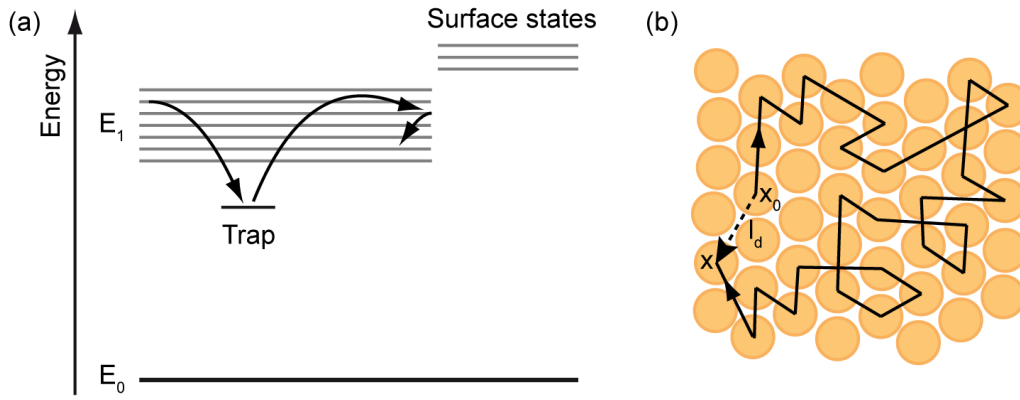


Figure 2.11: (a) Energy scheme illustrating the scattering of an exciton at an energetic trap as well as the reflection of the exciton at the surface of the aggregate (after [12]). (b) Motion of an exciton along organic molecules represented by spheres. The diffusion length l_d of an exciton is defined as the linear distance between the sites where it was created and vanishes. As the exciton motion is a random walk process, the real traveled distance is much larger than the diffusion length.

The experimentally observed effective exciton lifetime τ is in general determined by the sum of the rates of the radiative decay of the exciton k_r , defining the natural radiative lifetime, and the sum of all radiationless rates:

$$\tau = \frac{1}{k_r + \sum k_{nr}^i}, \quad (2.18)$$

with k_{nr}^i being the radiationless decay rates present in the system. The quantum yield of efficiency η from a given state can then be expressed as [13]

$$\eta = \Phi k_r \tau = \Phi \frac{k_r}{k_r + \sum k_{nr}^i}, \quad (2.19)$$

where Φ denotes the formation efficiency of the emitting state.

A measure for the distance an exciton moves through an organic semiconductor during its lifetime τ is called diffusion length l_d . It is the linear distance between the initial site x_0 , where the exciton was created and the site x where it vanishes. As exciton migration via hopping is a random walk process, the actual distance traveled is much larger than l_d , as can be seen in Figure 2.11 (b).

If the mobility of the exciton is considered to be isotropic, the diffusion length and the exciton lifetime are connected via the diffusion constant D :

$$l_d = \sqrt{ZD\tau} . \quad (2.20)$$

Z depends on the restriction of exciton motion and equals to six for three-dimensional motion, four for two-dimensional motion and two for one-dimensional diffusion. However, it is usually taken to be unity [12].

2.3.3 Excitons in Organic Crystals and Polymers

In addition to small radius Frenkel-type excitons, there also exists an intermediate or charge-transfer (CT) exciton in organic aggregates (Figure 2.12 (a)). In the latter case electron and hole are still coulombically bound forming a neutral polar excited state, but with an electron–hole separation, which is one or two times the intermolecular spacing. These excitons, also referred to as delocalized excitons, can be mobile, as electron and hole can move from one molecular site to the next, or trapped. The associated absorption and PL bands are usually broad, as the larger spatial extent allows for different structural configurations coexisting in equilibrium, and exhibit no characteristic vibrational features due to the intermolecular character [13]. In accordance with the band picture treatment of Frenkel excitons, the CT exciton energy levels form subgap states.

Although being a neutral quasi-particle, the electron–hole pair can induce a polarization of the surrounding electron density as well as the atoms — perhaps even the lattice — while moving through the organic semiconductor [12]. This exciton–phonon interaction can result in a delocalized exciton (CT exciton) being converted to a localized exciton by a self-induced local distortion called self-trapping. These bound states split off from the main exciton band (see Figure 2.12 (b)). The relative energetic position of the self-trapped excitonic state with respect to the delocalized state strongly depends on the energetics of the material system under investigation. A way to describe this aspect is to calculate the exciton–phonon coupling constant [32, 33]:

$$g = \frac{E_{LR}}{E_B} , \quad (2.21)$$

where E_{LR} is the lattice relaxation energy by trapping of the exciton and E_B the half width of the exciton band (see Figure 2.12 (b)) [32, 34]. If $g > 1$ then the

formation of a trapped exciton is energetically favored, while for $g < 1$ it is the opposite.

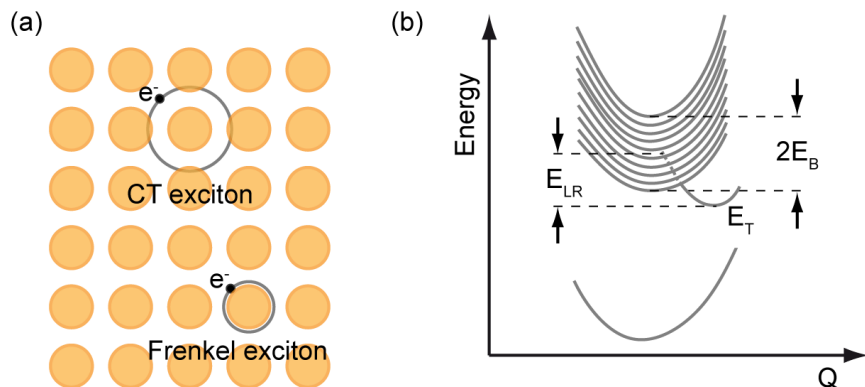


Figure 2.12: (a) Schematic drawing comparing the spatial extent of Frenkel and CT excitons. The molecules are indicated by lattice sites (after [12]). (b) Self-trapping of an exciton leads to the presence of a localized excitonic state E_T that splits off from the main excitonic band (after [32]).

Conjugated polymers that, besides small molecule organic crystals, form the second class of widely used organic semiconducting materials are comprised of a large number (couple of thousand to several ten thousands) of identical and equally spaced repeat units, called monomers, forming a long chain. An example is Poly(3-alkyl)thiophene (see Figure 2.13 (a)), a polymer that was intensively studied over the last decade. In these systems the absorption of a photon leads to the creation of an exciton which is delocalized over several monomers [35, 36] as a result of the overlap of the π -electron orbitals of the closely spaced monomers. These excitons are considered as Frenkel-type excitons and have binding energies in the range of ≈ 0.3 to 0.6 eV. [37, 38, 39]. The interaction between different chains, however, is very weak and comparable to the interaction of neighboring molecules in organic crystals [40].

A real polymer is not a perfectly straight and flat chain but has a shape as indicated in Figure 2.13 (a) with kinks, twists and loops. Due to the disordered character of the polymer system interchain interaction is efficiently suppressed and polymers can in principle be described as one-dimensional organic semiconductors [40]. This morphological disorder hampers the transport of excitons both between neighboring chains (interchain transport) and along a single chain (intrachain transport). Due to the kinks, twists, defects and impurities the spatial extent of the delocalized π -system along the chain is interrupted resulting in a distribution of conjugated segments (see Figure 2.13 (b)). The exciton can move

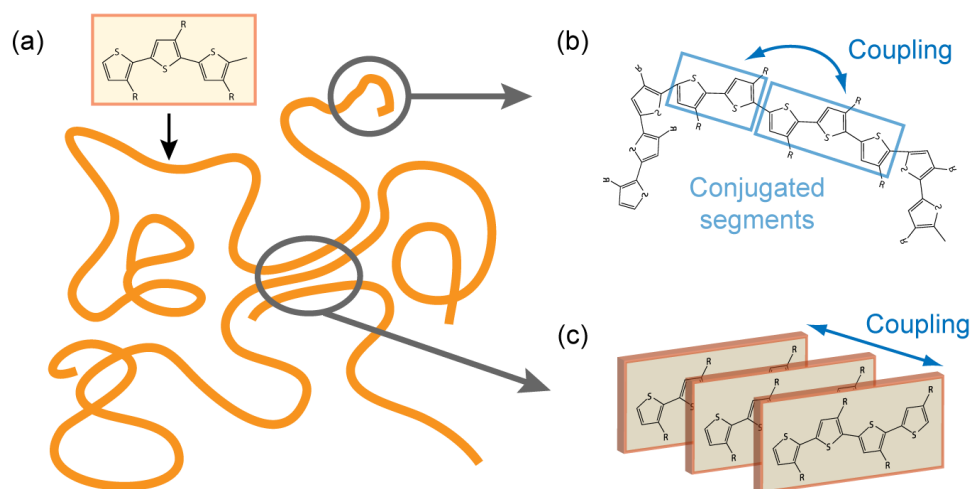


Figure 2.13: (a) Schematized polymer chain comprised of a large number of identical repeat units, for example Poly(3-alkyl)thiophene. (b) The distortion of the delocalized π -electron systems leads to the segmentation of the chain into coupled conjugated subunits. Created excitons can hop between these segments in an energetic downhill process. (c) Ordered regions within the polymer give rise to interchain coupling and thus also interchain migration of excitons.

within this system by hopping between different conjugated segments of one chain or segments between adjacent chains according to the Förster model [41]. These jumps will take place from smaller to larger conjugated segments (“particle in the box principle”) in an energetic downhill process. Reported diffusion lengths are between 3 and 14 nanometers [42, 43]. Moreover, exciton migration in polymers was reported to occur also via tunneling and thermally assisted hopping [44, 45]. In principle, as the classical Förster model assumes spherical donor and acceptor sites, one has to carefully check if deviations from the Förster model observed for a polymer system are due to the presence of an additional transport mechanism or just the result of missing adaption of the model to polymer systems.

If the polymer system exhibits ordered regions with parallel and closely spaced polymer chains or segments of these chains (Figure 2.13 (c)), a second type of exciton, called delocalized exciton, can be observed as result of the interchain coupling. Compared to intrachain excitons, the binding energy of interchain excitons is expected to be larger due to the absence of intra-monomer electron repulsion [46]. Compared to intrachain motion the transfer of excitation energy between different chains was reported to be faster [47] as the orientation of transition dipoles between two chains is more favorable than between two segments on the same chain. A prominent example for a material system where these in-

terchain coupling effects are visible is Poly(3-hexylthiophene-2,5-diyl) (P3HT). Here the polymer chains form lamella-like structures and the influence of inter-chain coupling on absorption and emission spectra can be modeled applying the aggregate picture [48, 49, 50].

2.3.4 Polarons and Charge Transfer States

A charge carrier (positive or negative) in an organic semiconductor, whether it was transferred from another material, injected or created after absorption of a photon, strongly interacts with its local environment. It can be approximated as a molecular ion that polarizes its surrounding resulting in a distortion of the electronic distribution (electronic polarization) and a slight change of the center of gravity of the neighboring molecules (lattice polarization) as indicated in Figure 2.14(a) [51]. As the electronic and lattice polarization times are usually much faster than the residence time of the charge carrier at a certain site — for example 10^{-16} s (electronic) and $10^{-16} - 10^{-14}$ s (lattice), respectively compared to a residence time of $10^{-14} - 10^{-13}$ s as for anthracene [12, 52] — the carrier surrounded by a polarization cloud is described as a quasi-particle called polaron. Due to the polarization, which can be seen as a local deformation of the lattice, the carrier tends to localize, if the polarization energy is larger than the interaction energy between molecules and the residence time is sufficiently long. This is in general the case for organic semiconductors while for inorganic semiconductors the low polarizability results in a fast transfer of carriers between neighboring sites and — considering the comparatively wide charge transport bands — they can be seen as being delocalized. In organic crystals the resulting energy levels associated with the electron and hole polarons are — in analogy to inorganic semiconductor theory — described by energy bands [12, 53], also referred to as valence and conduction band (Figure 2.14 (b)). Nevertheless, due to the weak intermolecular coupling and the so-called band-narrowing effect [54] these bands are narrow compared to inorganic semiconductors and the bandwidth calculated is usually below 100 meV at room temperature [55]. As the charge-phonon coupling is strong, the charges and their motion cannot be described by Bloch-waves [17] but, considering local and nonlocal electron-phonon coupling, by an extended Holstein-Peierls formalism [53] based on the model introduced by Holstein [54, 56]. The charge transport in organic crystals is assumed to depend on both band transport and thermally assisted hopping between sites and is in general highly anisotropic [53].

A charge that is put on a polymer chain also results in a local polarization and distortion of this segment of the chain (Figure 2.14 (c)). As a result the energy levels of the ionized subunit are shifted with respect to the HOMO and LUMO levels of the “neutral” monomers (Figure 2.14 (d)). In a band picture this

again leads to the rise of (polaronic) gap states [57, 58]. In principle polarons in polymers are described by the electron–phonon model [59, 60]. The disordered character of the system results in the non-applicability of a band-like model for describing the energetic levels involved in charge transport and the latter mechanism itself. Instead, the resulting polaronic energy levels are described by a Gaussian distribution of states and the polaron motion is described by thermally activated hopping [61]. As already discussed for excitons, in certain cases, where there is significant coupling between chains, as for P3HT, the existence of inter-chain polarons, also called delocalized or 2D polarons, in addition to intrachain or 1D polarons has been reported [62]. Nevertheless, for most polymer systems the predominant polaron type is expected to be of intrachain character.

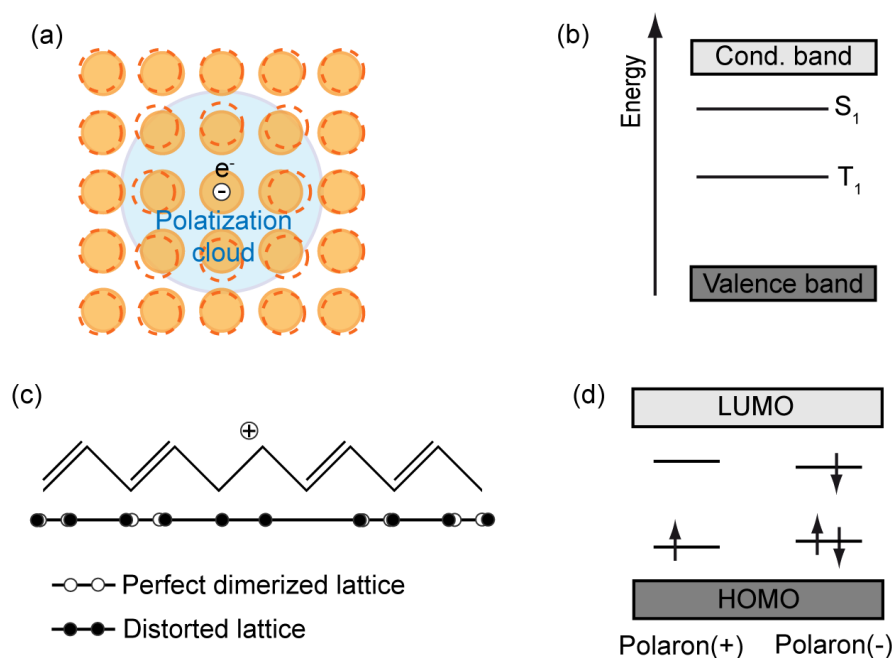


Figure 2.14: (a) Lattice site representation of an organic semiconductor exhibiting a single negative charge carrier that is located at a molecular site surrounded by a polarization cloud. This quasi-particle is called polaron. the dashed circles depict the lattice polarization. (b) The polaronic levels of an organic crystal can be described by bands in accordance with inorganic semiconductor theory. (c) A charge carrier put on a polymer chain also creates a local polarization and distortion of its surrounding resulting in a polaronic state ((a)-(c) after [12]). (d) In accordance with the discussion of excitonic states, the polaron can be described by gap states.

Charge generation can be promoted by bringing two different molecules, ex-

hibiting an energetic offset between the respective LUMO energy levels, in close vicinity to each other. It can be realized for example by the mixing of two different organic molecules in solution or the growth of heteromolecular crystals. If the distance between both types of molecules is small so that their electronic orbital wave functions overlap (compare Dexter mechanism), then, after excitation of the donor molecule, the electron from the excited state of the donor can be transferred to the excited state of the acceptor with the associated rate k_{CT} (Figure 2.15). The result is a positively charged donor and a negatively charged acceptor molecule. The electron and hole are in general still coulombically bound and the excited donor-acceptor complex is called CT state [13]. Binding energies estimated for these complexes in polymer-fullerene systems (see Section 2.4) are between 0.1 and 0.5 eV [26] and thus smaller than associated singlet exciton binding energies. In principle, a CT state can also be the result of an energy transfer towards the acceptor molecule followed by a hole transfer to the donor [15]. As being coulombically bound, the CT state can decay to the ground state (radiatively or radiationless) with k_R or the charges can be separated, if electron and hole are able to move away from the donor-acceptor site. If the first excited triplet state of the donor is close to or even lower in energy than the excited acceptor level, the electron can be transferred to the donor triplet level (k_{EBT}). This process is called electron back transfer.

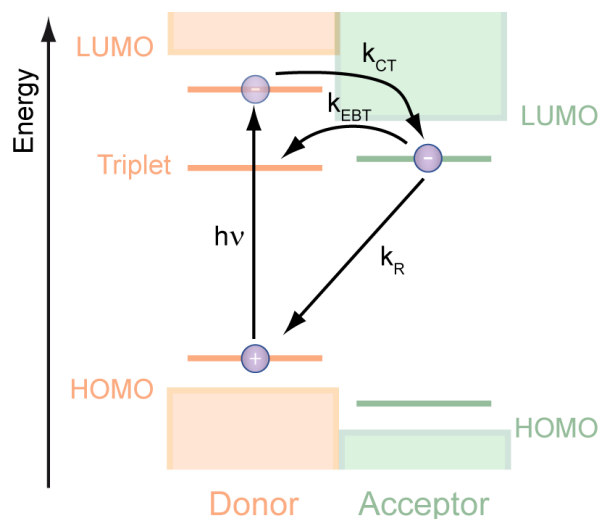


Figure 2.15: Bringing together two different molecules with a favorable offset between both LUMO levels can result in the transfer of an electron from the excited donor (D) towards the acceptor (A). If the donor triplet excited state is close in energy to the acceptor LUMO, then the electron can be transferred back towards the donor (after [15]).

2.4 Photophysics of the Bulk Heterojunction

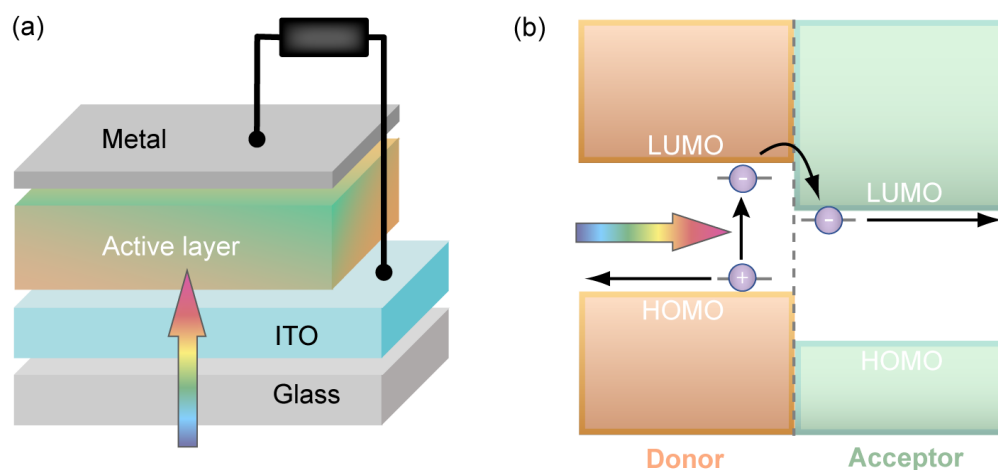


Figure 2.16: (a) Schematic layout of an organic solar cell comprised of an active layer which is sandwiched between a transparent bottom and a metal top electrode (after [15]). (b) Working principle of the heterojunction solar cell: The absorption of light creates singlet excitons within the donor phase which can migrate towards an interface. There they are split as the electron is transferred towards the acceptor. The opposite charges can then migrate to the respective electrodes and are extracted (after [26]).

The basic idea behind a solar cell, no matter if organic or inorganic materials are used, is the generation of free charges by the absorption of light. In order to achieve this, the exciton, which is initially generated via photon absorption in the active layer of the cell, has to be separated. Afterwards the carriers can be extracted at the top and bottom electrodes. A schematic drawing of a solar cell device structure is shown in figure 2.16 (a). In organic materials, as discussed above, due to the low dielectric constant, the exciton binding energy is of the order of 0.3 to 0.6 eV so that at room temperature excitons are not efficiently split. Therefore a second organic material acting as an electron acceptor has to be introduced into the active layer which exhibits a high electronegativity, for example the buckminsterfullerene C_{60} [63]. If the offset between the first excited singlet state of the donor and the first excited level of the acceptor associated with the CT state is large enough (approximately slightly higher than the exciton binding energy), the electron is transferred to the acceptor, as it is energetically more favorable (Figure 2.16 (b)). The exciton is now split but the electron on the acceptor and the hole on the donor may still be coulombically bound forming a

CT state, also referred to as polaron pair. By applying an external electric field, and/or driven by the interfacial energy gradient (see section 5), the charges are split and can migrate to the respective electrodes by hopping processes.

In practice donor–acceptor layers are mostly realized by evaporation of small donor and acceptor molecules (e.g. metal phthalocyanine donor and C_{60} acceptor molecules [64]) or by spin-casting blends comprised of polymer donors and fullerene acceptors from solution. The design of the active layer can be realized by a planar donor-acceptor-heterojunction as straight forward design. However, as the layer thickness has to be of the order of the absorption length (≈ 100 nm) [15, 26], the efficiency is limited by the short diffusion length of the singlet excitons, which is ≤ 10 nm [42, 43]. To overcome this limitation the bulk heterojunction design was introduced, which is based on the active layer being comprised of a blend of donor and acceptor molecules. Here the whole layer is an interdigitating donor–acceptor network and the large interface area allows for efficient exciton splitting throughout the layer. The disadvantage of this concept, however, comes with the more complicated separation and transport of the charges, due to the disordered system [15]. As the experimental work in this thesis is based on the bulk heterojunction design of the active layer of organic solar cells, further discussion will address this type only.

The processes that follow photoexcitation of a bulk heterojunction and finally lead to the creation of free charge carriers are depicted in Figure 2.17 (a) while Figure 2.17 (b) schematically shows the same mechanisms in an energy level diagram with the associated rates (inverse time constants). After absorption of a photon, which mostly takes place in the donor material, a singlet exciton is created (1) which can then migrate to a donor-acceptor interface (2) via Förster-type hopping and tunneling processes within its lifetime, which is of the order of 0.1 to 1 ns [26, 65]. At the interface the electron from the excited donor state is transferred towards the first excited state of the acceptor molecule within less than 200 fs [66, 67, 68, 69]. The result is the formation of a still coulombically bound interfacial state, the CT complex (3) indicated by the dashed potential barrier in Figure 2.17 (b). For example by applying an external field the bound polaron pair can be split with the rate k_{CS} resulting in separated charges that can move away from the interface (4). In principle, as indicated in Figure 2.17 (b), the initial thermal excess energy of the CT state after electron transfer from the donor, also referred to as hot CT, can possibly help overcoming the binding energy, compared to the relaxed or cold CT state [26, 70, 71, 72]. The CT dissociation is in general considered to be faster than 200 fs [73, 74] while a few studies report an additional lower ps time constant [75, 76] which might be due to diffusion assisted CT splitting.

The free charges, referred to as charge separated states (CS), can migrate along percolation pathways by thermally activated hopping towards the respec-

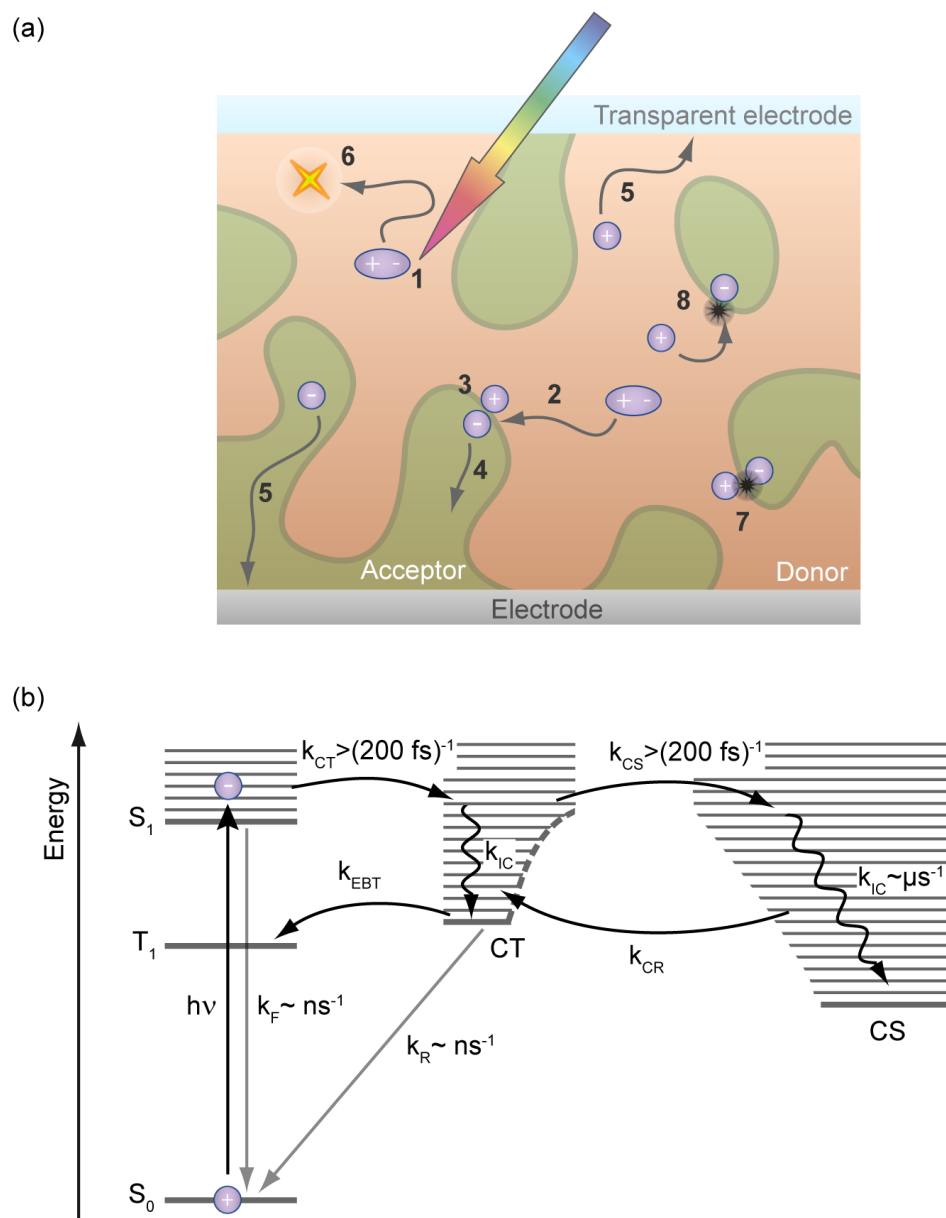


Figure 2.17: (a) Scheme illustrating the photophysical processes following the absorption of light within a bulk heterojunction solar cell (1-5). In addition possible loss mechanisms are indicated (6-8). (b) Energy level scheme of the processes depicted in (a) together with the associated rate constants (after [26]).

tive electrodes (5) (electrons in acceptor phase and holes in donor phase) and are extracted. Although the singlet exciton yield is in general much lower in the acceptor than in the donor material, also excitons generated in the acceptor phase contribute to the total number of generated charges. In this case the initial charge transfer is of opposite character, i.e. a hole is transferred from the acceptor towards the donor. The timescale for hole transfer is found to be comparable to reported electron transfer times [77].

Besides losses of generated singlet exciton by relaxation to the ground state (6) or ISC to the triplet state, the separation of the CT state and the transport of free charges harbor potential loss mechanisms. The CT complex can decay to the ground state (7), called geminate recombination, as both recombination partners originate from the same excitation site (exciton). For systems like polyphenylene vinylenes or polyfluorenes the associated CT-PL can be detected [78, 79, 80, 81] and, compared to donor singlet PL the emission of the interfacial state is redshifted [26, 37]. Reported CT lifetimes vary between half a ns and a few ns depending on the material system [82, 83]. In addition, as discussed in Section 2.3.4, the electron can be transferred back from the acceptor to the donor triplet level [84]. In specific cases where there is significant overlap of donor PL with the acceptor absorption, energy instead of electron transfer towards the acceptor followed by ISC can lead to negligible charge generation yields [85, 86].

During transport charge carriers can meet their opposite charge and recombine with the rate k_{CR} (8) probably via a CT state [26]. The process is called nongeminate recombination, as both charges have a different excitonic precursor state. This recombination process can be described according to Langevin [87]. Besides the recombination of two mobile opposite charges (bimolecular process), a mobile charge carrier can also recombine with a trapped opposite charge, which is called monomolecular recombination. Effective lifetimes reported for charge carriers within a bulk heterojunction range from μs to ms [88, 89, 90].

Experimental Section

In this chapter the studied organic material systems as well as the experimental details of the two time-resolved spectroscopy setups that were built in this work are summarized. The introduction of the materials focuses on the description of employed sample types and morphologies as well as a motivation of their use in the context of improving the performance of organic solar cell devices. The explanations concerning the experimental methods concentrate on the fundamental working principles and the actual design and measurement procedure of the installed setups. A short description of the recipe for thin film copolymer and copolymer-fullerene blend sample preparation can be found in the appendix (A.1).

3.1 Material Systems

3.1.1 Prototypical Organic Semiconductor Rubrene

Rubrene is a small molecule that is comprised of a tetracene backbone with four benzene rings attached to it (see Figure 3.1 (a)). These rings are tilted with respect to the backbone resulting in a slight twist of the tetracene subunit for rubrene in the gas phase [91]. Rubrene molecules form single crystals of several millimeters [92](Figure 3.1 (a)) by arranging in a so-called herringbone pattern as indicated in Figure 3.1 (b) under backbone planarization. These crystals are of exceptional structural quality as indicated by the x-ray diffraction (XRD) measurements (GE Inspection Technologies XRD 3003 T/T) showing Bragg peaks up to the fifteenth order (Figure 3.1 (c)). Experimental details concerning the growth of rubrene single crystals can be found in the work of T. Schmeiler [93]. Rubrene is often considered as a benchmark material for organic electronics, especially for organic field-effect transistors due to the high hole-mobility of up to $20 \text{ cm}^2/\text{Vs}$ [94] and proves to be an ideal prototypical organic semiconductor system for optical studies of excitonic processes [95, 96, 97]. Moreover, sufficiently high PL quantum yields in combination with different, well-controllable rubrene morphologies allows for studies of the correlation between characteristic length scales and excitation transport (see Chapter 4).

Apart from pyramidal surface structures resulting from specific growth conditions [98], rubrene crystals of micrometer size can be fabricated by precipitation

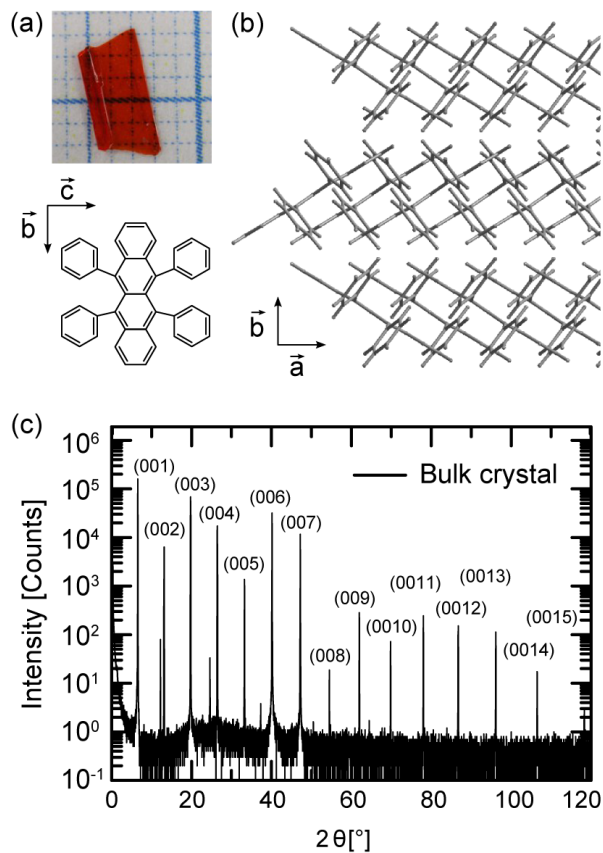


Figure 3.1: (a) Top: Photograph of a rubrene bulk single crystal. Bottom: Schematic structure of the rubrene molecule being comprised of a tetracene backbone with four attached benzene rings. (b) These molecules arrange in a herringbone-like pattern to form single crystals of several millimeters. (c) The high crystallinity is indicated by x-ray diffraction measurements exhibiting Bragg peaks up to the fifteenth order.

from solution as described in literature [99, 100]. Resulting ensembles of rubrene crystals with typical lateral extensions between one and two μm were imaged using scanning electron microscopy (Zeiss REM Ultra-Plus) and exemplary pictures are shown in the Figure 3.2. The crystallinity of the structures is proven by corresponding transmission electron microscopy images (FEI-TitanTM) exhibiting characteristic diffraction patterns. In general two different types of microcrystals can be found: hexagonal- and rectangular-shaped ones. The difference in shape might arise from the different orientation of the crystallographic axes with respect to the substrate as indicated by the different diffraction patterns for the two different shapes.

Due to an activation barrier of 210 meV required for planarization of the

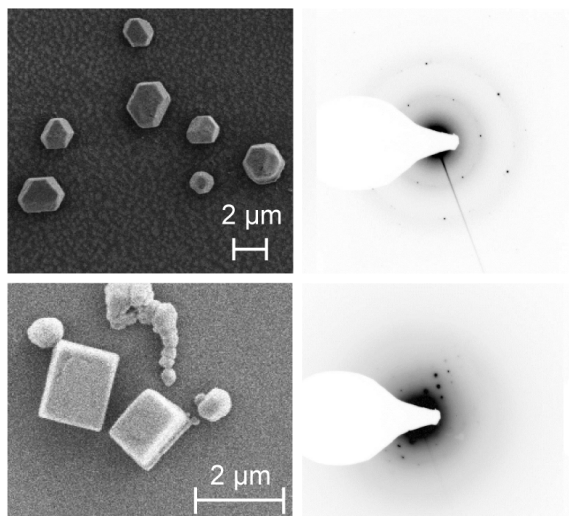


Figure 3.2: Micrometer sized rubrene crystals fabricated by precipitation from solution as imaged with a scanning electron microscope (left hand side). The crystalline character is confirmed by transmission electron microscopy diffraction images (right hand side). Two different types of microstructures can be fabricated that seem to differ in the orientation of crystallographic planes with respect to the substrate (top and bottom).

tetracene backbone [91], thin films of rubrene deposited under high vacuum grow x-ray amorphous thus adding another type to the range of structural morphologies that can be fabricated in a well-controllable manner. A photograph of an amorphous rubrene film is shown in Figure 3.3 (a) together with an x-ray diffraction measurement of the thin film (Figure 3.3 (b)). The XRD scan exhibits Kiessing oscillations, which can be used to determine the thickness of the layer and the absence of Bragg peaks confirms the amorphous character of the film.

3.1.2 Copolymer Donor Materials

While the high absorption coefficients of polymer-based donor materials allow for thin active layers of ≈ 100 nm, the relatively narrow absorption spectra, usually covering the ultraviolet (UV) and (partly) visible (VIS) range of the solar spectrum, inhibit the efficient harvesting of sunlight [15]. Furthermore a significant percentage of the energy of absorbed photons is lost in the light-to-charge conversion process as the difference between donor HOMO and acceptor LUMO level is directly proportional to the open-circuit voltage (V_{OC}) [101] thus defining the potential energy of extracted charges. A typical representative of these types of polymers is P3HT (Figure 3.4 (a)), which for a long time was the “working horse” for organic photovoltaics yielding efficiencies of up to

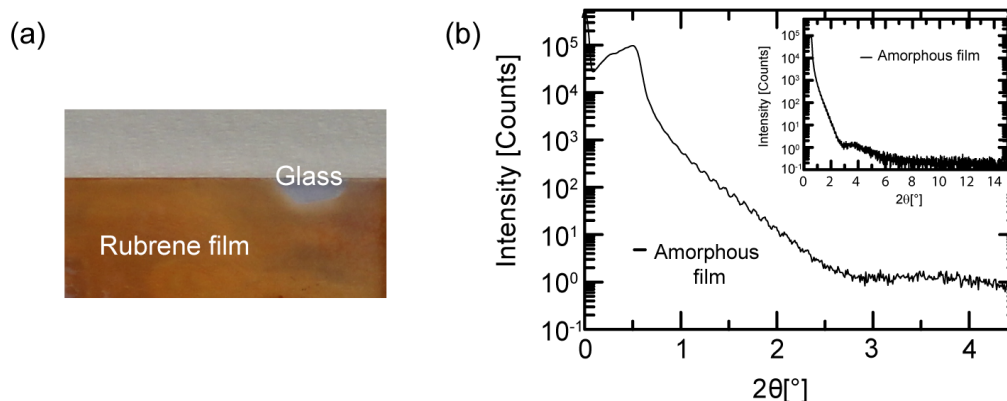


Figure 3.3: (a) Picture of a glass substrate covered with a thin amorphous film of rubrene. (b) The Kiessing oscillations appearing in the XRD scan can be used to determine the crystal thickness. The absence of Bragg peaks confirms the amorphous character of the film.

5 % [10]. Recently a new class of donor materials, the so-called copolymers, has been introduced. These materials exhibit a reduced bandgap and are designed for more efficient harvesting of the solar spectrum and an increased V_{OC} [102, 103, 104, 105]. As a result the performance of organic solar cells comprised of these new donor materials and fullerene acceptors could be significantly enhanced reaching efficiencies above 10 % [7]. These so-called third generation polymers exhibit a more complex molecular structure compared to their second generation counterparts, as for example P3HT, and their repeat units (comonomers) are usually comprised of two or more subunits (monomers). The two copolymers studied in this work are on the one hand poly[N-(1-octylonyl)-2,7-carbazole]-alt-5,5-[4',7'-di(thien-2-yl)-2',1',3'-benzothiadiazole] (PCDTBT) and on the other hand poly[4,8-bis-alkoxy-benzo[1,2-b:4,5-b']dithiophene-2,6-diyl-alt-4-(alkyl-1-one)thieno[3,4-b]thiophene-2,6-diyl] (PBDTTT-C). Their molecular structures are shown in Figure 3.4 (b) and (c), respectively.

PCDTBT is a prominent member of the group of carbazole-based polymers that together with fluorene-based polymers represent the widely studied family of donor-acceptor (D-A) copolymers [106, 107, 108]. It was first synthesized by Leclerc and co-workers [109] and exhibits an internal quantum efficiency approaching unity and yields solar cells with efficiencies of up to 7.2 % [110, 111, 112]. The repeat unit consists of a carbazole monomer (1), which exhibits good photoconductivity and increased chemical and environmental stability compared to fluorene [109, 113, 114], and a benzothiadiazole unit with two thiophene side-groups (DTBT, 2).

The copolymer PBDTTT-C, which was introduced by Yu and coworkers [115], is based on a benzodithiophene unit (1) which, combined with thiophene, exhibits very high hole mobilities compared to other conjugated polymers [116]. The second functional group is a thienothiophene monomer (2) that is expected to stabilize the quinoidal structure of the backbone which results in a smaller energetic gap and enhances the planarity of the copolymer chain [117]. Reported efficiencies of PBDTTT:fullerene solar cells are around 7 % [115] and a slightly modified version of PBDTTT-C, called PTB7 [118, 119], even yields efficiencies of more than 9 % in an inverted device structure [120].

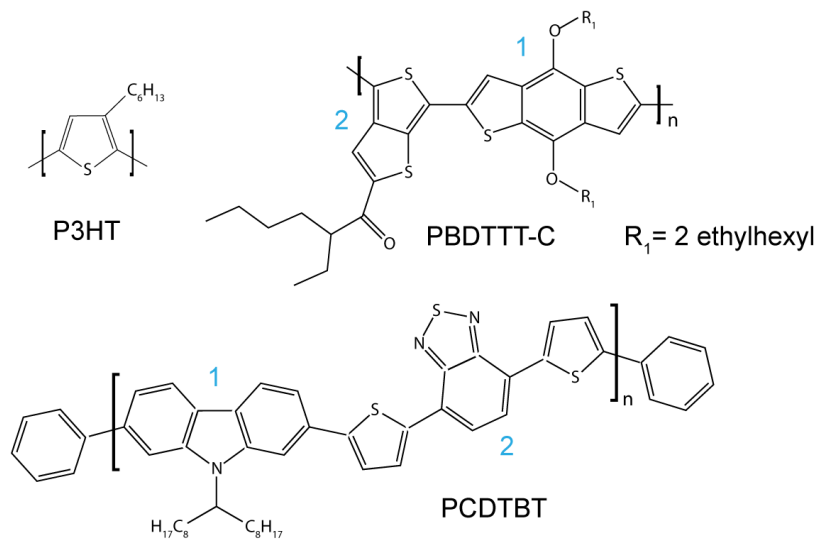


Figure 3.4: Molecular structures of the donor polymer and copolymer materials used in this work. The labeled copolymer subunits are discussed in the text.

The basic concept behind the copolymer approach for controlling the molecular energy level and hence the bandgap is schematically shown in Figure 3.5 (a). In accordance with the formation of molecular orbitals (compare section 2.1) the monomer subunits ($M_{1,2}$) can be described by their characteristic HOMO and LUMO levels. The corresponding levels of the comonomer, i.e. the copolymer, are then formed by the interaction of the monomer subunits resulting in a reduced bandgap compared to the monomers. By individually modifying the monomers and changing their energy levels, in principle, both bandgap and energetic positions of the copolymer HOMO and LUMO levels can be altered in a controllable way [104]. The ideal procedure is to lower the HOMO level in order to increase V_{OC} while at the same time reducing the bandgap to increase the number of generated charges [115]. However, the copolymer systems synthesized so far do not satisfy both criteria in equal measure. Comparing the absorption spectra

of PCDTBT with second generation polymer P3HT (Figure 3.5 (b)) one finds that the copolymer absorption is only slightly extended to lower energies compared to P3HT. The increased efficiency of PCDTBT-based devices can thus be primarily attributed to the improved chemical engineering of the energy levels (increased V_{OC}), while the harvesting of sunlight is still restricted to the 300-700 nm region. In contrast, PBDTTT-C exhibits an absorption spectrum that is extended to 800 nm and thereby combines both favored properties of copolymers — reduced bandgap and increased V_{OC} — which in principle explains the further increase in device efficiency. It has to be mentioned that in general the extension of copolymer absorption into the NIR is limited by the concurrent reduction of donor–acceptor LUMO offset that goes along with the bandgap reduction. Since this offset mainly defines the driving force for charge separation at the donor–acceptor interface, an optimized balance between extended donor absorption and sufficient driving force for charge separation is desirable from a material engineering point of view. However, the contributions of “hot” excitons dissociating at the interface as well as the role of excess energy of the CT state (compare section 2.4) have to be considered concerning the charge generation process as these processes could reduce the impact of the aforementioned LUMO offset.

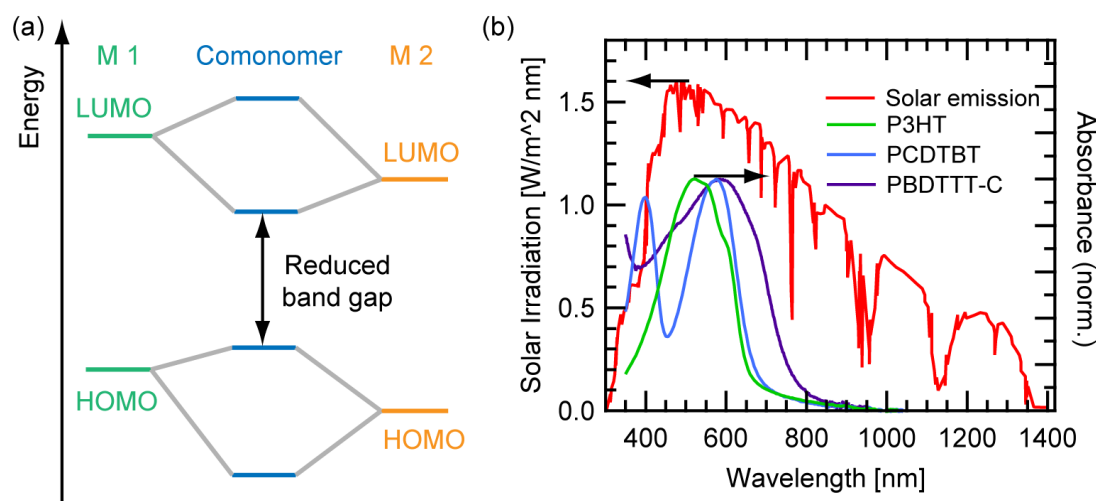


Figure 3.5: (a) Energy scheme illustrating the emergence of the copolymer band gap resulting from the interaction of the monomer subunits $M_{1,2}$. (b) Comparison of the absorption spectra of the analyzed donor materials with the solar irradiation spectrum. The use of new copolymer materials improves the matching of donor absorption and solar irradiation spectra.

3.1.3 The Fullerene Acceptor

While much effort is put into the design of better donor materials, the best electron acceptor materials so far are still the fullerene derivatives [6,6]-phenyl C₆₁ butyric acid methyl ester (PC₆₀BM) and [6,6]-phenyl C₇₁ butyric acid methyl ester (PC₇₀BM [121, 122]). These molecules are based on C₆₀ and C₇₀ fullerenes, respectively [63]. The molecular structure of PC₇₀BM that is used as electron acceptor in this work is shown in Figure 3.6 (a). The attached sidechain, which was chosen to be compatible with the electrophilic character of the fullerene, is needed to make the molecule soluble [121]. The electronic and optical properties of the molecule are defined by the fullerene. The reason why fullerene derivatives are still the most successful acceptor materials might be due to the spherical shape promoting an interdigitating donor–acceptor network and supporting the strong electron withdrawing character [123]. The advantage of PC₇₀BM compared to PC₆₀BM is the increased absorption in the visible range between 360 and 700 nm due to the less symmetric shape promoting the lowest-energy electronic transition [122]. As the active layer of organic solar cells contains a large amount of acceptor molecules which contribute to charge generation (see section 2.4), the increased absorption of PC₇₀BM promotes the device efficiency. Especially in the range between 300 and to 600 nm the acceptor absorption significantly contributes to the absorption of the blend (see Figure 3.6 (b)).

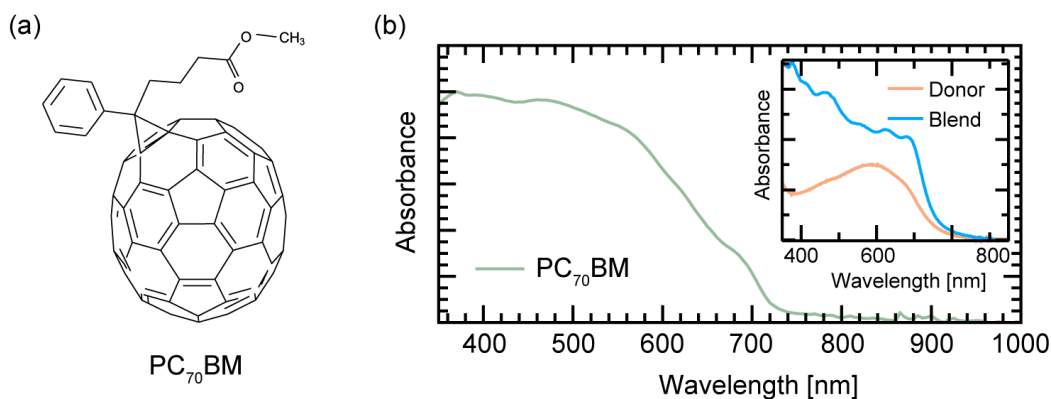


Figure 3.6: (a) Molecular structure of the fullerene-based acceptor PC₇₀BM used in this work. (b) Absorbance of a thin film of PC₇₀BM molecules. The inset shows a comparison of the absorbance of a neat copolymer film and a blend film with PC₇₀BM. The acceptor absorption significantly enhances the blend absorption in the 300 to 600 nm range.

3.2 Femtosecond Laser Setup

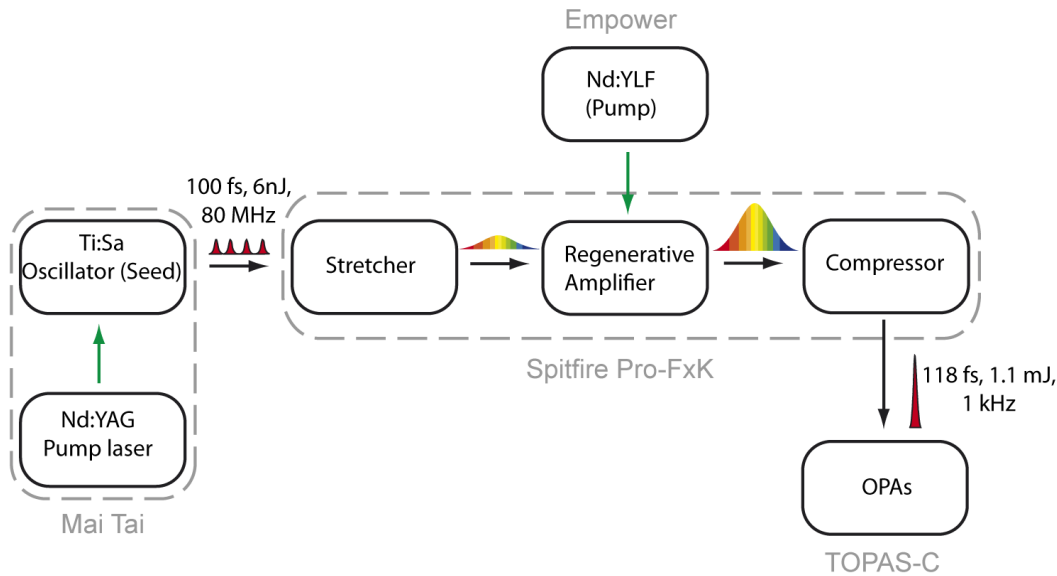


Figure 3.7: Scheme of the regenerative amplifier system used as the femtosecond laser source for both time-resolved spectroscopy setups.

The two different picosecond time-resolved experimental methods that were built and used in this work (see the following two sections) are based on a regenerative amplifier femtosecond laser system. A scheme summarizing the different components that are needed for this type of laser source is shown in Figure 3.7: A mode-locked titanium-sapphire (Ti:Sa) oscillator with an integrated diode pumped Nd:YAG solid state pump laser (Mai Tai VF-N1S, Spectra Physics) is producing laser pulses at 795 nm central wavelength with a duration of 100 fs and a pulse energy of 6 nJ at a repetition rate of 80 MHz. These pulses are used as seed pulses that are amplified within a regenerative Ti:Sa amplifier cavity. In order to increase the energy of the pulses without damaging the gain medium the seed pulses are stretched in time by passing an angular dispersive element (reflection grating) before entering the actual amplifier. The amplified pulse is then again compressed in time by the use of a second grating yielding 118 fs pulses centered at 795 nm with an energy of 1.1 mJ at a 1 kHz repetition rate. All three components — stretcher, amplifier cavity and compressor — are part of a one box system (Spitfire Pro-FxK, Spectra Physics). The amplifier cavity is externally pumped by a diode-pumped q-switched ND:YLF pulsed laser (Empower, Spectra Physics). The temporal width of the pulses generated by the amplifier can be monitored using an autocorrelator (Pulsescout, Spectra Physics). A

schematic drawing of the actual layout of the described components as installed on the laser table can be found in the appendix (A.3) while a detailed description of the laser components is given by the manufacturer in the respective manuals.

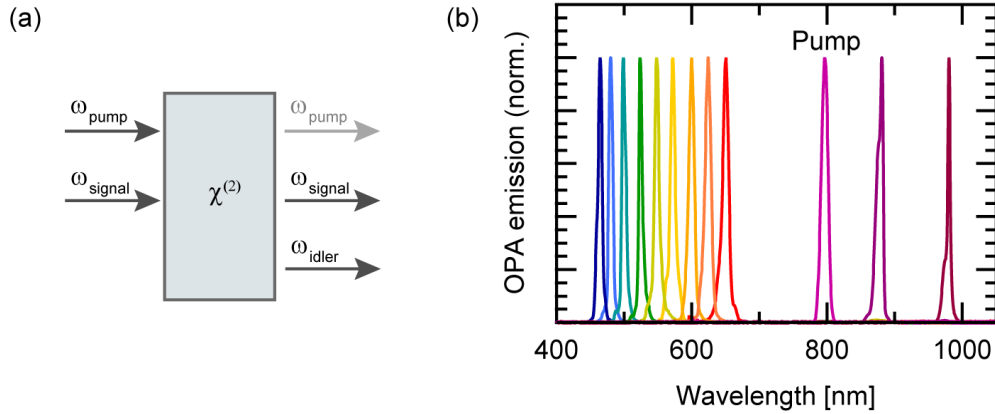


Figure 3.8: (a) Scheme illustrating the principle of frequency conversion of light within a non-linear optical crystal. (b) Emission spectra of one of the OPAs together with the spectrum of the pump pulse (Spitfire).

In order to be able to choose from a broad spectral range of excitation wavelengths used for the optical experiments, the laser pulses leaving the regenerative amplifier system are used to pump two optical parametric amplifiers (OPA) as indicated in Figure 3.7. An OPA is based on the principle of frequency conversion in non-linear optical crystals: A spectrally broad signal pulse (white light) and a pump pulse are spatially and temporally overlapped within the crystal. Due to the high photon densities within the pulses, a fraction of the pump-photons is converted to a signal- and an idler-photon (Figure 3.8 (a)) satisfying the conservation of energy:

$$h\omega_{\text{pump}} = h\omega_{\text{signal}} + h\omega_{\text{idler}} . \quad (3.1)$$

This means that the signal spectrum is amplified and in addition idler photons, which are of a different wavelength than the signal photons, are generated. In the OPA systems that are implemented in this setup (TOPAS-C, Light Conversion), the resulting signal (or idler) pulses are further boosted in a second non-linear crystal by overlap with a fraction of the pump beam. A subsequent frequency mixing process (for more details see the manual of the manufacturer [124] and additional literature on nonlinear optics [125]) finally leads to fs laserpulses with central wavelength covering the whole visible part of the spectrum up to $12 \mu\text{m}$ in the infrared region. Spectra of pulses generated by one of the OPAs in the

visible and near infrared spectral range are shown in Figure 3.8 (b) together with the spectrum of the pump pulse from the regenerative amplifier. Further details regarding the optical layout and working principle of the OPAs can be found in the TOPAS-C manual.

3.3 Time-resolved Photoluminescence Spectroscopy

3.3.1 Setup

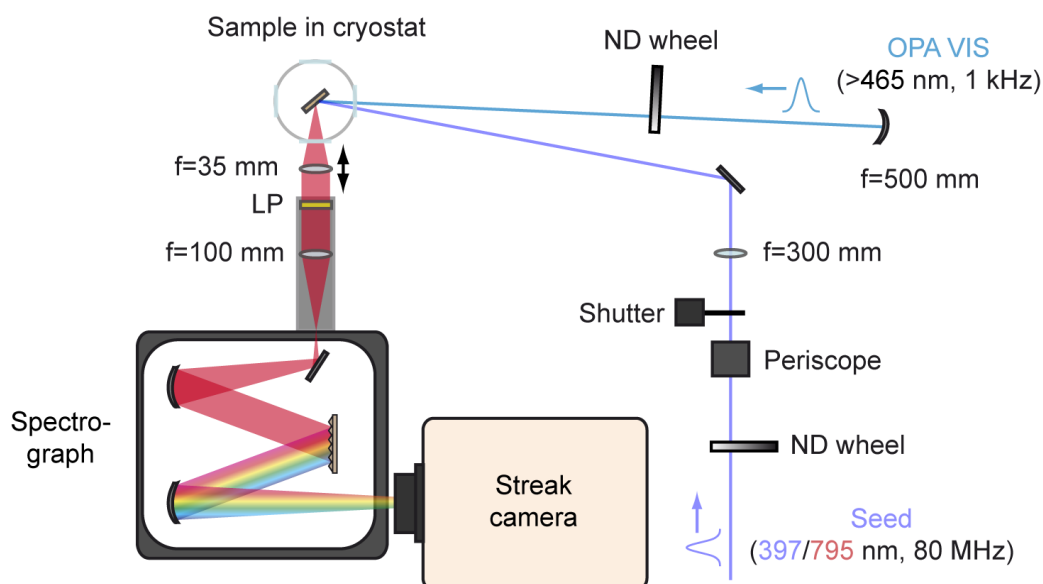


Figure 3.9: Setup built for carrying out temperature dependent time resolved PL measurements.

The layout of the picosecond time-resolved photoluminescence spectroscopy setup is shown in Figure 3.9. The sample is mounted to a coldfinger within a continuous flow liquid helium/nitrogen optical cryostat (ST-300, Janis Research). The cryostat itself is mounted to a x,y,z-linear stage module allowing for a precise manipulation of the sample position (see Figure A.2 in the appendix). The cooling medium is transferred to the cryostat through a vacuum isolated transfer line using a diaphragm pump (MP 601 E, Ilmvac). The temperature of the cold finger is controlled by an attached ohmic heater and monitored by a silicon sensor diode installed at the heater, both driven by a temperature controller unit (331 S, Lakeshore). The isolation vacuum and the measuring vacuum at room

temperature of 10^{-5} – 10^{-6} mbar, respectively is generated by a turbo molecular pumping station (HiCube 80 Eco, Pfeiffer Vacuum).

The sample is excited using either the partial output of the Mai Tai seed laser (only 50 % of the output power is used as seed for the regenerative amplifier) or the output of one of the OPAs as illustrated in Figure 3.7. Both sources yield pulses in the 100–120 fs range, thus satisfying the necessary condition of an ultra-short excitation source. The excitation power of both sources can be adjusted to the experimental conditions using a neutral density filter wheel and the beams can be blocked in front of the sample by a self-built automated shutter. After excitation of the sample the emitted photoluminescence signal is collected by a collimating achromatic lens and passes through a longpass filter (LP) to remove scattered laser light. The filtered PL is then focussed onto the entrance slit of a Czerny–Turner type spectrograph/monochromator (Acton SP2300i, Princeton Instruments) by a second achromatic lens. To minimize the influence of laser light, the sample is tilted so that reflected laser light does not enter the spectrograph. The filter and the second achromatic lens are mounted within a metal tube to prevent ambient light from entering the spectrograph. The first achromatic lens is mounted on a linear stage to optimize collimation and thus maximize the collected PL signal. Inside the spectrograph the light is spectrally dispersed yielding a spectral or energy resolution by mapping this information on a linear (horizontal) scale. Afterwards the spectrally resolved PL signal is projected onto a streak camera.

3.3.2 SHG Stage

While the high repetition rate of the Mai Tai is beneficial for the signal-to-noise ratio of a measurement, the fixed central wavelength of 795 nm is not convenient for many organic molecular systems having an absorption spectrum that is limited to the visible range. Therefore a stage for second harmonic generation (SHG) of input light from the Mai Tai was implemented on the desk in front of the seed laser yielding pulses with a center wavelength of 397.5 nm. A scheme of the SHG stage is shown in Figure 3.10 (a): The output of the Mai Tai is focused into a beta-bariumborate (BBO) nonlinear crystal (Type I, $d=500 \mu\text{m}$) cut for optimum SHG output at perpendicular incidence of the fundamental beam with respect to the crystal surface plane. In general the Rayleigh length z_R of the focused beam should be comparable or slightly smaller than the crystal thickness to guarantee for efficient SHG. For the used focusing lens the calculated value of $z_R \approx 560 \mu\text{m}$ matches well with the value of d (for details see additional literature on gaussian laser beam geometry for example [126]). The generated second harmonic signal, as well as the non-converted light are collimated by a second lens and the residual light at 795 nm central wavelength is removed using

a reflective shortpass filter (HC 680/SP, Semrock). The resulting spectrum of the second harmonic signal is shown in Figure 3.10 (b). The BBO-crystal is mounted in a rotation holder and on a rotation stage in order to optimize the crystal axes with respect to the incident laser beam according to phase-matching conditions ($\theta=29.2^\circ, \phi=90^\circ$). For a well adjusted stage the resulting second harmonic conversion efficiency is $\approx 15\%$. If needed, this value can be increased to 20–30% by reducing the Rayleigh length of the focused beam, for example by using a lens with a shorter focus.

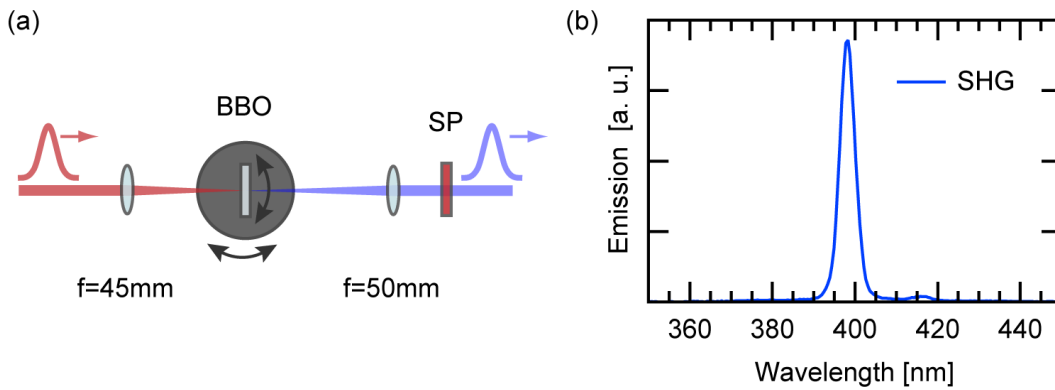


Figure 3.10: (a) Scheme of the SHG stage built for frequency doubling the pulses of the Mai Tai excitation source. (b) Resulting SHG spectrum measured after the SHG stage.

3.3.3 Streak Camera

In principle the temporal resolution of electronic photodetectors is limited to the nanosecond regime, as common photodiodes show response times of at least one nanosecond. With a streak camera as used in this work, however, it is possible to achieve temporal resolutions ≤ 2 ps. This is achieved by mapping the time on a vertical axis, meaning that the temporal information is transferred to spatial information. A schematic drawing of the important components of a streak camera visualizing its working principle is shown in Figure 3.11 (a): The spectrally dispersed light leaving the spectrograph passes through the entrance slit of the camera and is focused onto the photocathode by a lens pair. The incident photons create electrons that are accelerated and propagate through the streak tube, passing a pair of electrodes and hit a multichannel plate (MCP). Afterwards the multiplied electrons are detected on a phosphor screen with a CCD camera (Orca R², Hamamatsu). The spectral response of the camera is

hence defined by the cathode material. In this work two streak tubes with two different cathodes were used. One being sensitive in the 250–900 nm range (C5680-24, Hamamatsu) and one between 400–1600 nm (C5680-22, Hamamatsu). If a sweep voltage is applied to the electrodes, the electrons are being deflected while passing through the tube. Depending on their arrival time they “feel” a different electric potential and electrons arriving later get more deflected than those arriving earlier. The result is a vertical deflection pattern, that reflects the arrival time of the electrons and thus the detection time of the emitted photons. As a result the streak camera yields two-dimensional contour maps displaying the temporally and spectrally resolved photoluminescence of the sample. An exemplaric map is shown in Figure 3.11 (b). Horizontal cuts from these images resemble the spectral distribution of emitted photons for a certain point in time after excitation, while vertical cuts display the temporal evolution of photons of a given wavelength. As the number of emitted photons is proportional to the number of emitting species, i.e. singlet and/or triplet excitons, the measured maps directly contain spectrally and temporally resolved information about these excited states populations and their evolution with time.

Since the excitation of the sample is pulsed, the synchronization of the deflection voltage and the arrival time of the excitation pulse at the sample is crucial. Hence the pulse train of the Mai Tai laser is monitored as a reference signal by detecting a pick-off beam of the laser with a photodiode. The starting time of the linear increasing deflection voltage can then be adjusted with respect to the pulse arrival time using a delay unit for triggering the voltage ramp. A fundamental disadvantage of any electric circuitry in general is that the position of a trigger in time exhibits a certain inaccuracy, called trigger jitter. In order to minimize this jitter and achieve a temporal resolution in the low picosecond regime, the streak tube is customized to the exact repetition rate of the Mai Tai (79.86 MHz) by an integrated oscillating circuit yielding a sinusoidal voltage of the same frequency. The streak is triggered at the zero crossing point of the sine function using its linear part as voltage ramp. This procedure guarantees for a fixed phase relation of consecutive trigger events yielding the maximum temporal resolution of 2 ps at the full detection rate (≈ 80 MHz). However, using the linear part of the sine voltage limits the maximum detection window to 2.1 ns. This measurement modus is called synchro scan and the exact measurement scheme is illustrated in the Appendix (A.5). As the excitation pulse width is in the 100-120 fs regime, the overall temporal resolution of the time-resolved PL setup is limited by the response of the streak camera. Whenever a longer measuring window is needed the synchro scan module, i.e. the whole deflecting module, can be changed for a so-called single sweep module. Here a simple voltage ramp drives the deflecting electrodes. This mode limits the maximum detection rate to 1 MHz and also reduces the temporal resolution of the camera. The longest detection time win-

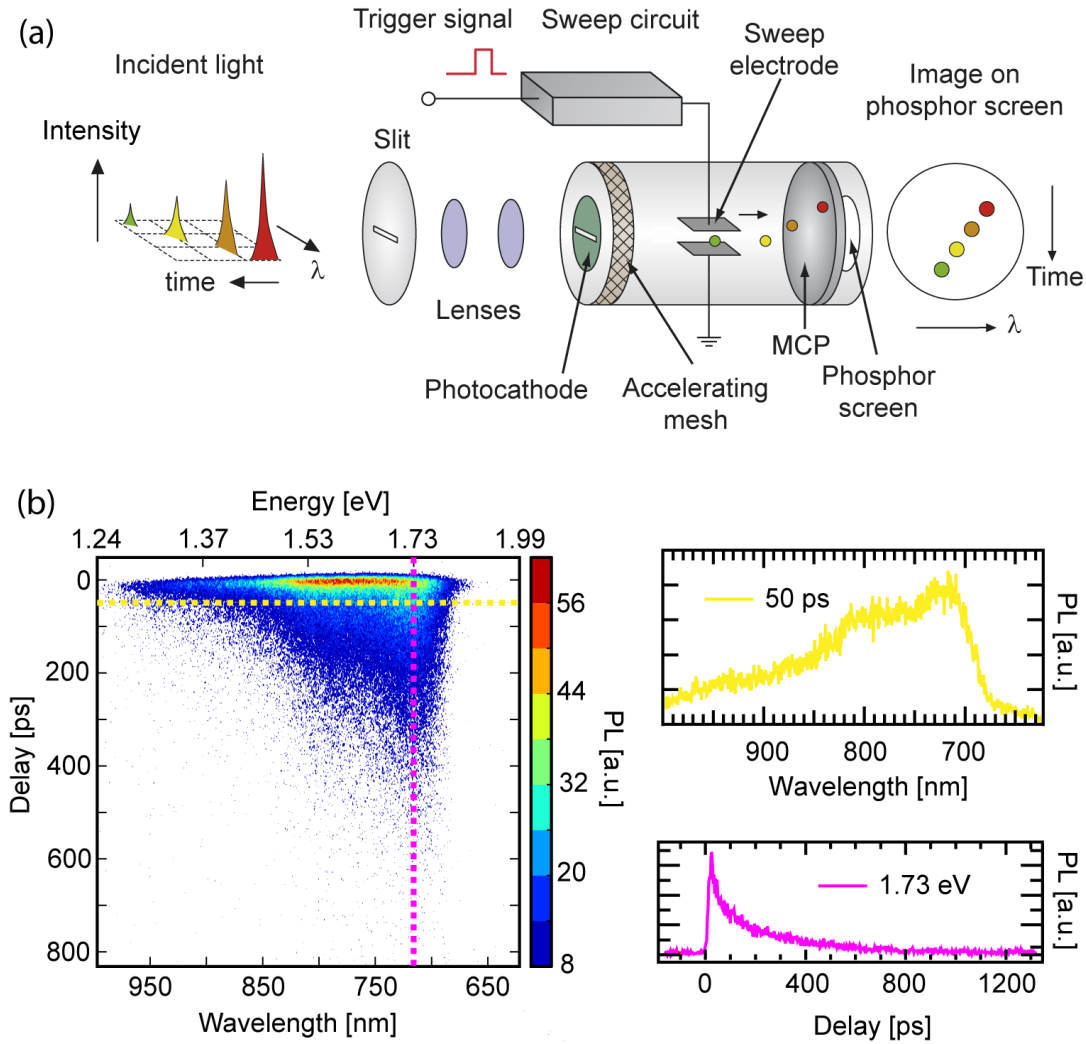


Figure 3.11: (a) Scheme showing the fundamental components of a streak camera (after [127]). (b) Exemplaric 2D contour map measured with the streak camera (left hand side). On the right hand side the extracted data for the horizontal and vertical cuts indicated by the dashed lines are shown.

dow is now limited by the time between excitation pulses of 12.5 ns. For slowly decaying PL signals and if specific excitation wavelength are needed, the output of one of the OPAs can be used. This intrinsically reduces the detection rate to 1 kHz. The synchronization of the internal oscillating circuit of the camera with the external reduced excitation frequency is achieved by the use of a dump-mode box (for measurement scheme again see Appendix A.5).

Since the streak camera is an imaging system, achieving the highest possi-

ble temporal resolution crucially depends on the optimization of the input and output optics. This includes the focussing of both the PL signal on the cathode as well as the phosphorescence from the screen on the CCD chip. Since the time axis is mapped to the vertical deflection axis, which is imaged by the CCD camera, the maximum resolution of the streak system corresponds to 5–6 (Vis tube) and 6–7 (IR tube) vertical pixel on the CCD chip, respectively. For different measuring windows the maximum temporal resolution can therefore be calculated using the number of vertical CCD pixel and the maximum detection time.

The temporal resolution Δt as well as the time zero t_0 , corresponding to the point in time where excitation of the sample by the laser pulse takes place, of a given measurement can be determined from the rising edge of a transient. Therefore the corresponding part of the data is fitted using the error-function. This function is a convolution of a Gaussian function and the Heaviside step function and it describes the finite response time of a detection system, characterized by the FWHM of the Gaussian function, while the step function depicts the theoretical instantaneous response. The expression for the fit function is given by:

$$PL(t)_{zero} = A + \frac{B}{2} \operatorname{erf} \left[\frac{\sqrt{2}(t - C)}{D} + 1 \right], \quad (3.2)$$

where A is the offset, B the amplitude, C the temporal offset (t_0) and D twice the standard deviation of the Gaussian function ($D = 2\sigma$). From the fit the temporal resolution can be calculated by:

$$\Delta t \hat{=} FWHM_{Gaussian} = \sqrt{2 \ln(2)} D. \quad (3.3)$$

Assuming an exponential decay behaviour of the emitting species, the complete transient data can be fitted using a function that is a convolution of the error-function and one or more exponential functions [128, 129]:

$$PL(t) = A + \sum_i \frac{B_i}{2} \left\{ \operatorname{erf} \left[\frac{\sqrt{2}(t - C - D^2/2\tau_i)}{D} \right] + 1 \right\} \times \exp \left(-\frac{t - C}{\tau_i} \right) \exp \left(-\frac{D^2}{4\tau_i} \right). \quad (3.4)$$

Here again A denotes the offset, B_i the corresponding amplitudes of the different exponential contributions, C the temporal offset, D twice the standard deviation and τ_i the time constants of the exponential decays.

3.4 Femtosecond Transient Absorption Spectroscopy

3.4.1 Method

The installed picosecond time-resolved spectroscopy setup, apart from all described advantages, has one considerable limitation: It can only be used for the detection of emitting species — singlets, triplets and CT states — and the mapping of their decay dynamics and only if there is sufficient emitted signal to be collected (especially the detection of CT PL is quite challenging for many organic systems). To be also able to monitor the temporal evolution of non-emitting excited states in organic semiconductors, especially polarons, with high detection sensitivity a second time-resolved spectroscopy setup using femtosecond laser pulses was built in this work. The method is called femtosecond transient absorption (TA) spectroscopy and is a form of pump-probe technique. It is based

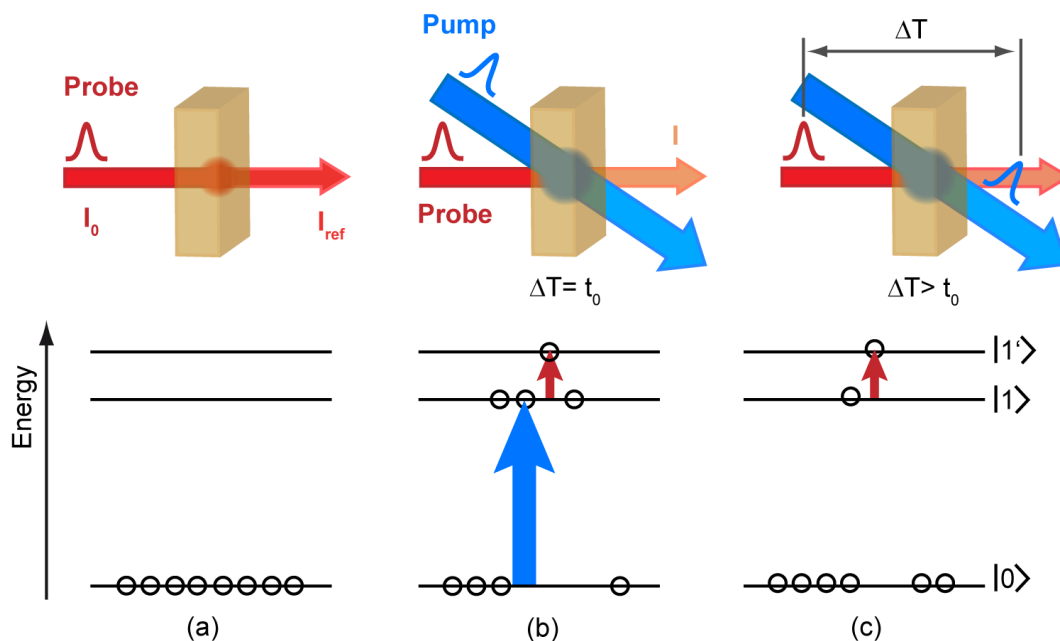


Figure 3.12: The concept behind transient absorption spectroscopy shown for a three-level system. In the absence of a pump pulse (a) the probe pulse is transmitted through the sample. Excitation of the sample (b) leads to absorption of the probe which is proportional to the number of excited states. For increased delays ΔT between pump and probe pulses the subsequent decay of excited state population leads to the reduction of absorption of the probe beam (c).

on the absorption of a probe pulse by (intermediate) states generated by a preceding pump pulse that is monitored as a function of the delay ΔT between both pulses. This delay is introduced by using a high precision linear stage changing the optical path length of the pump beam with respect to the probe beam. As a consequence the delay (time) axis is mapped to the linear axis of the stage. Due to the high spatial resolution of the stage, the temporal resolution of this method only depends on the pulse widths and not on the response of any electronic circuit, giving access to sub-picosecond response times. A scheme illustrating the principle behind TA spectroscopy for a three-level system is shown in Figure 3.12. Without the presence of the pump beam, the probe beam having an energy smaller than the energetic gap E_{01} between levels $|0\rangle$ and $|1\rangle$ is transmitted without significant losses (Figure 3.12 (a)). Applying an additional pump beam matching E_{01} creates an excited state population of $|1\rangle$. If the probe beam is chosen to be in resonance with the transition $|1\rangle \rightarrow |1'\rangle$ then the probe beam is partially absorbed by the excited sample (Figure 3.12 (b)). The absorption is proportional to the population of the excited state and with the decay from $|1\rangle$ back to $|0\rangle$ the induced absorption is continuously reduced (Figure 3.12 (c)). Applying perturbation theory it can be shown that the pump probe spectroscopy is based on a third order nonlinear polarization P^3 of the sample created by its interaction with the electrical fields of pump (twice) and probe pulses [130, 131]. This polarization is the source of an electric field:

$$\frac{\partial E(t)}{\partial z} = \frac{2\pi i}{\varepsilon_0 \lambda_{probe}} P^3(t) , \quad (3.5)$$

with λ_{probe} being the probe wavelength and ε_0 the electric constant. In the small signal limit an equation describing the resulting electric field that solves Equation (3.5) is given by:

$$E_{res}(t) = E_{probe}(t) + E_{gen}(t), \quad E_{gen}(t) = \frac{2\pi i L}{\varepsilon_0 \lambda_{probe}} P^3(t) . \quad (3.6)$$

Here L is the optical path length of the laser beams within the sample. The generated electric field within the sample ($E_{gen}(t)$) interferes with the probe field after the sample and, depending on the phase relation between both fields, reduces or magnifies it by destructive and constructive interference, respectively. The resulting signal is then monitored by a photodetector, whose response time is much slower than the ultrashort signal impulse. Therefore the detected signal is proportional to the time-integrated value of E_{res} :

$$\int_{-\infty}^{\infty} |E_{res}(t)|^2 dt = \int_{-\infty}^{\infty} \{|E_{probe}(t)|^2 + |E_{gen}(t)|^2 + 2Re[E_{probe}(t)E_{gen}(t)]\} dt . \quad (3.7)$$

The first term in this equation depicts the probe signal transmitted by the non-excited sample and can be subtracted if measured separately. The second term can be neglected in the small signal limit while the third term presents the probe signal modulated by the signal from the excited sample.

According to the Lambert–Beer law the intensity of light I transmitted through an absorbing medium of given thickness d can be expressed as

$$I(\lambda, \Delta T) = I_0(\lambda)e^{-\sigma(\lambda)N(\Delta T)d} , \quad (3.8)$$

with $I_0(\lambda)$ being the incident light intensity, $N(\Delta T)$ the number density of the absorbing excited species and $\sigma(\lambda)$ the corresponding absorption cross section. The Absorbance or optical density (OD) of the medium can then be derived giving the following expression:

$$OD(\lambda, \Delta T) = \log_{10} \left[\frac{I_0(\lambda)}{I(\lambda, \Delta T)} \right] = \frac{\sigma(\lambda)N(\Delta T)d}{\ln(10)} . \quad (3.9)$$

Using a reference beam to monitor the intensity transmitted by the sample in the absence of the pump beam $I_{ref}(\lambda)$, the change in absorption induced by the pump beam as a function of probing wavelength and delay time can be written as

$$\Delta OD(\lambda, \Delta T) = \log_{10} \left[\frac{I_{ref}(\lambda)}{I(\lambda, \Delta T)} \right] = \frac{\sigma(\lambda)[N(\Delta T) - N_0]d}{\ln(10)} . \quad (3.10)$$

This value is directly proportional to the number density of the absorbing species and thus measuring ΔOD as a function of delay time ΔT between excitation and probe pulse yields the information about the population dynamics of the probed species. If one is mainly interested in the identification of the generated transient species by their spectral signature, then it is sufficient to use continuous excitation (continuous wave laser) and probe sources (white light) and derive the photo-induced absorption (PIA) spectrum by comparing the transmitted probe light with and without the excitation.

The change in OD can be positive if absorption by an excited state takes place, as indicated in Figure 3.12 but it can also have a negative sign in the cases of the so-called *ground state bleach* and *stimulated emission*. Ground state bleach describes the situation where the probe wavelength is in resonance with the transition from the ground to the first excited electronic level of the analyzed system, i.e. in the spectral range of its absorption spectrum. As the population of the ground state is reduced by the preceding pump pulse, the absorption of the probe pulse is decreased by the pump resulting in a negative value of ΔOD . Increasing the delay between pump and probe, the excited electrons subsequently decay to the ground state resulting in an increase of absorption of the probe pulse called *bleach recovery*. If the probe wavelength is in the range of the PL

spectrum of the analyzed system, the probe pulse leads to stimulated emission by reducing the excited state population. This process results in a net increase of detected probe signal (negative ΔOD), since it is of the same wavelength as the emission from the sample. For obvious reasons the negative bleach and stimulated emission bands of organic semiconductors are usually in the visible spectral range.

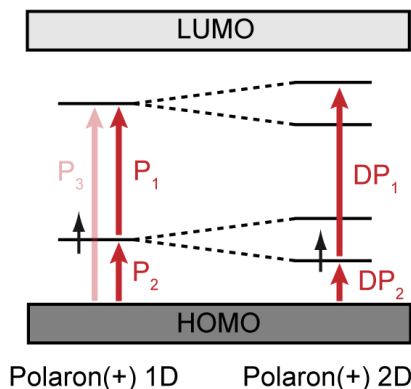


Figure 3.13: Additional optical transitions introduced by the presence of optically excited transient species, here hole polarons, within the organic semiconductor (after [62]). Significant intermolecular coupling effects give rise to additional delocalized (2D) states and additional transitions (right hand side).

The energetic levels and associated probe wavelength for transient absorbing species in organic semiconductors, such as polarons, can be described applying the energetic gap state picture introduced in Chapter 2. Following excitation of the sample, the presence of photogenerated charge carriers leads to the presence of specific associated states in the semiconductor bandgap. In Figure 3.13 these states are illustrated for a hole polaron for example in the polymer donor phase of a photovoltaic blend. The gap states give rise to new optical transitions P_1 to P_3 [58] that can induce absorption of probe pulses of the corresponding wavelengths. Experimentally, the predominantly observed transitions are P_1 and P_2 [58] that give rise to two transient absorption bands in the NIR — the first typically around ~ 1100 nm (P_1) and the second in the 2500 to 4000 nm region (P_2). Assuming significant interchain coupling effects, the presence of interchain or delocalized polarons (DP) [62] can give rise to additional transient polaron signatures ($DP_{1,2}$) as indicated in Figure 3.13. Besides transient absorption signatures of polarons (holes in the donor and electrons in the acceptor phase, respectively) also contributions by CT states [71, 75], triplets and interchain excitons [62] have been observed, resulting in quite complex PIA spectra with spectrally overlapping absorption bands, as for example for P3HT–fullerene

blends [62].

Especially when a broad probe spectrum, a so-called white light continuum, is used, an intense pump pulse can interact with the probe pulse in a dispersive medium like the transparent substrate of the sample films. The pump pulse induces a polarization in the medium that interacts with the probe pulse resulting in a transient absorption signature that overlaps with the true signal from the organic film [132, 133]. However, this effect is only relevant for delay times that are very small ($< 1\text{ps}$) compared to the decay dynamics in polymer–fullerene blends and thus can be neglected as, in addition, the probe spectrum used in this work is quite narrow.

A second measuring artifact that can be observed is the so-called perturbed free induction decay [131, 134]. It is relevant for probe wavelengths that are in resonance with present vibrational transitions. For negative delays, i.e. when the probe pulse is arriving before the pump pulse, the probe field induces a polarization that superimposes with the basic probe signal. The subsequent pump pulse can then change this polarization leading to a net change in detected transient absorption signal. Due to the causality principle this transient signal contains no useful physical information and, since only appearing for negative delays, can easily be neglected.

3.4.2 Setup

Figure 3.14 shows a detailed scheme of the femtosecond transient absorption setup that was built in this work. The pump and probe pulses, are each generated by the two installed OPAs (OPA VIS, OPA NIR). The pump pulse is delayed with respect to the probe pulse by the use of a motorized linear stage (UST 150 PP, Newport) being equipped with a retro reflector (U-BBR 2.5-5S, Newport). The stage yields a maximum delay of 300 mm corresponding to 1 ns delay time at a minimum step width of $0.3\ \mu\text{m}$ ($\hat{=}$ 2 fs) and an accuracy of $\approx 7\ \mu\text{m}$ ($\hat{=}$ 47 fs). After leaving the stage, the pump beam passes a 1:2 telescope and is focused onto the sample that is mounted inside the cryostat with a concave mirror. Before reaching the sample, the polarization of the pump beam is rotated using a half-wave plate and attenuated with a neutral density filter wheel. Residual spectral contributions from the Spitfire pump beam are removed using a cold mirror. The beam can be blocked right in front of the cryostat using a self-built automated shutter. Every second pump pulse is blocked using a chopper wheel (3501 Optical Chopper, Laser 2000) operating at 500 Hz to yield the reference probe pulses. A small amount of the pump beam is used to monitor the chopped signal with a silicon photodiode that is connected to a delay generator (DG 645, Stanford Research Systems) to yield a logical 500 Hz trigger signal that is needed for the data recording procedure. The small delay stage is used to adapt

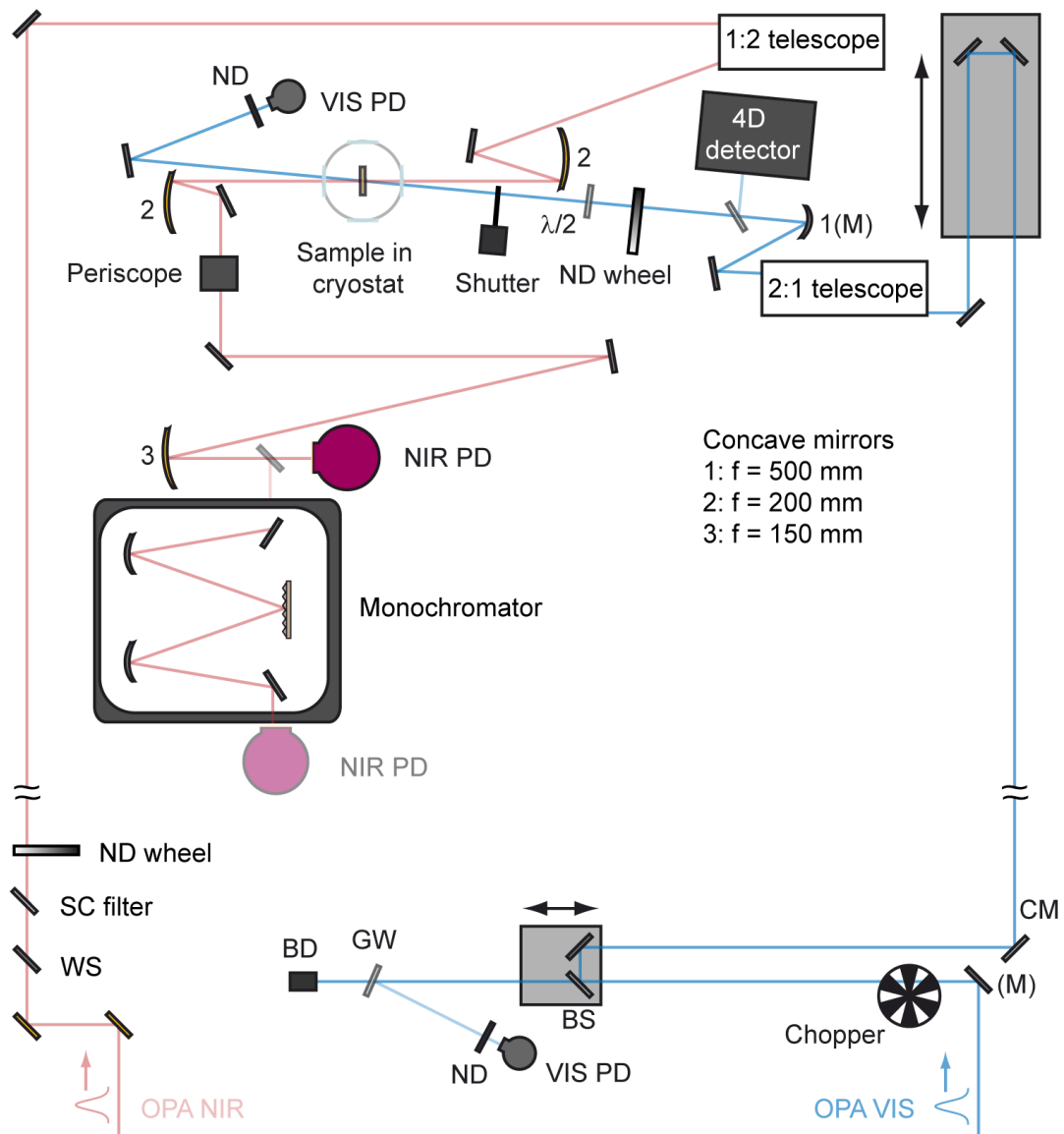


Figure 3.14: Layout of the transient absorption setup built in this work. ND: neutral density, PD: photodiode, GW: glass wedge, WS: wavelength selector, SC: semiconductor, BD: beam dump, BS: beam splitter, CM: cold mirror, (M): motorized holder.

the pump beam path length to the extended path length of the probe beam if OPA NIR is operated in the wavelength regime below 2600 nm. To prevent the pump beam spot on the sample from drifting during the measurement, an automated beam stabilization system (Aligna, TEM Messtechnik) is installed in the pump beam path. It corrects for changes of the pump beam path, introduced

by temperature gradients affecting the optics holders and the laser table itself, by using two motorized mirror holders and a so-called $4D$ detection unit.

The probe beam runs through a set of semiconductor filters to remove residual pump at 795 nm, passes through a 2:1 telescope and is focused onto the sample at the same spot as the pump beam using a concave mirror. The probe power can also be adapted using a neutral density filter wheel. The transmitted probe signal is then collimated using a second mirror and passes through a periscope, that adapts the beam height to the height of the entrance slit of the monochromator. Afterwards the signal is either directly focused onto the detector or first passes the monochromator. For the detection of the probe signal in the region ≥ 2500 nm a liquid nitrogen cooled preamplified mercury cadmium telluride detector (MCT-13-0.5, InfraRed Associates) is used. The resulting detector signal is time-integrated using a single channel boxcar averager (4121B, Signal Recovery), digitized and transferred to a computer that records the data using a customized LabVIEW-based evaluation procedure.

3.4.3 Measuring Procedure

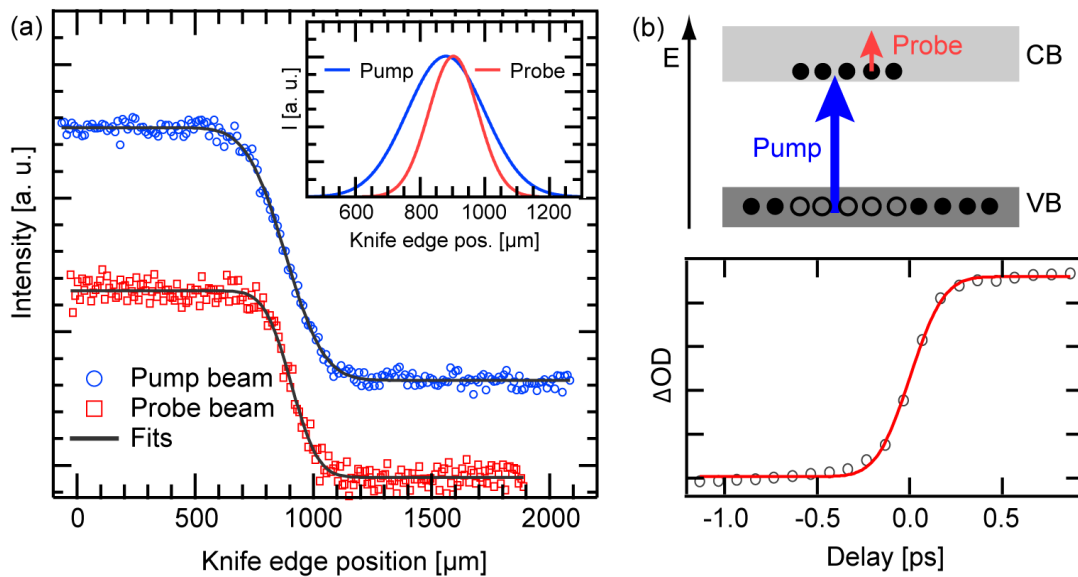


Figure 3.15: (a) Exemplary knife edge scans of pump and probe beam together with the reconstructed beam profiles (inset). (b) Cross-correlation scheme (top) and measured cross-correlation trace for determining time zero and temporal resolution of the TA setup using a germanium sample.

For a successful transient absorption measurement it is of utmost importance

to guarantee spatial overlap of both pulses at the sample position as well as their temporal overlap for an eligible position of the linear delay stage. Therefore, prior to every measurement, the spatial overlap of pump and probe beams at the exact position of the sample has to be optimized using a small pinhole (200 μm diameter). Afterwards the overlap of both beams can be checked using a self-built automated knife edge scanner (see Figure A.2 in the appendix). This beam characterization tool works as follows: A razor blade that is vertically mounted to an automated linear stage is gradually moved through the laser beam while the transmitted laser intensity is simultaneously being recorded with a photodiode. The resulting so-called knife edge scan (Figure 3.15 (b) top graph) is thus a convolution of the step function and the beam profile. Assuming a Gaussian shaped beam profile, the center position of the beam as well as its FWHM can be derived from the recorded data using the error function according to 3.2. Resulting reconstructed beam profiles for pump and probe beam are shown in the lower graph of Figure 3.15 (b). The data recording and evaluation for the knife edge scans is done using a customized LabVIEW program. Due to the two telescopes used in the beam paths of pump and probe beams respectively, the diameter of the pump beam ($\approx 520 \mu\text{m}$) at the sample position is larger than that of the probe beam ($\approx 350 \mu\text{m}$) guaranteeing the spatial overlap also when both beam positions slightly change during the measurement.

After optimization of the spatial overlap, the position on the linear stage corresponding to the exact spatial overlap of pump and probe pulses has to be determined. To achieve this, the cross-correlation of both pulses in a thin semiconductor sample (for example silicon or germanium) placed at the exact position of the sample is measured as a function of delay (see Figure 3.15 (c)). Pump pulses in the visible spectral range instantaneously generate free charge carriers in the semiconductor that subsequently absorb a part of the probe pulse intensity (Figure 3.15 (c) top graph). As excitation of charge carriers is expected to be instantaneous [135], the rising edge of the transient, corresponding to the region of temporal overlap between both pulses can be fitted using Equation (3.2). The temporal resolution Δt of the setup results from the convolution of the temporal shapes of pump and probe pulses, and, assuming Gaussian pulses, is also described by a Gaussian function. Thus, the derived values for the center position and the FWHM of the Gaussian function correspond to the time zero (t_0) and instrument response function of the setup, respectively, the latter being directly proportional the temporal widths of both pulses:

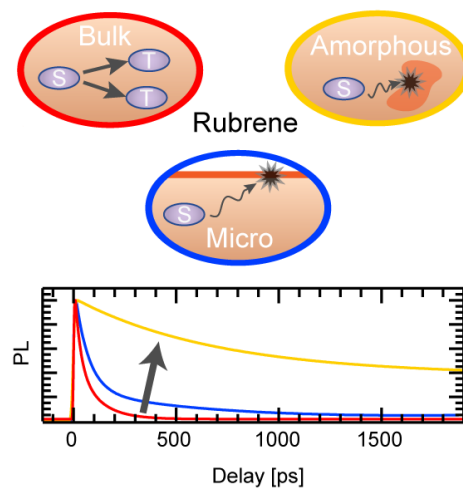
$$\Delta t = FWHM_{cross} = \sqrt{FWHM_{pump}^2 + FWHM_{probe}^2} . \quad (3.11)$$

The maximum temporal resolution achieved with the described transient absorption spectroscopy setup is around 400 fs. Temporal overlap of both pulses within

the range of the delay stage is guaranteed by carefully adapting both optical beam paths with respect to each other. For an optimal utilization of the linear stage, both beam paths were arranged in a way that for the maximum delay position the probe pulses arrive slightly before the pump pulses.

After spatial and temporal overlap procedures have been carried out, the real sample can be mounted within the cryostat and the measurement can be conducted. The described alignment, beam diagnostic and calibration measurement steps can all be carried out using the adjustment stage shown in Figure A.2 in the appendix. For this purpose it can be equipped with a sample holder module (for pinhole and semiconductor sample) and the knife edge module while the position of the razor blade, pinhole and semiconductor sample with respect to the incident beam are exactly the same. For standard measurement procedure, the pinhole and semiconductor sample can, however, also be mounted within the cryostat and the respective alignment and calibration steps can be carried out in this configuration. For changing between the two measurement types, Tr-PL and TA spectroscopy, the vertical position of the cryostat can be adapted to match the beam position with respect to the table of 160 and 200 mm, respectively. For this purpose it is mounted on an adjustable cryostat table (indicated in Figure A.2).

The Local Environment Affects the Exciton Dynamics in Rubrene Single Crystals



4.1 Singlet Fission for Organic Photovoltaics

The transport of excitation energy, i.e. the migration of excitonic states defines the key step in the light-to-charge conversion in organic semiconductor systems [136]. In principle, as discussed in Chapter 2, the short singlet exciton diffusion length of around 10 nm limits the yield of this step and calls for thorough device optimization. To overcome this bottleneck the harvesting of triplet excitons generated by singlet fission has been proposed within the organic photovoltaic community as a promising approach for enhancing solar cell efficiencies [137, 138]. This approach is motivated by the inherently fascinating fact that the fission process in principle allows for the generation and collection of two electrons and holes following the absorption of just one photon. In addition the generation of triplet excitons allows for long-range excitation transport as triplet lifetimes are found to be in the μs regime (compare Chapter 2). A second important issue

in the field of organic semiconductors arises from the further miniaturization of opto-electronic devices. This ongoing process shifts the correlation between exciton migration and device dimensions into the focus, as structural coherence significantly affects the dynamics of photoexcited states [136, 139, 140, 141].

Against this background rubrene is an ideal prototypical organic semiconductor to address both issues. On the one hand it offers the possibility of different well controllable structural morphologies (see section 3.1.1) to study the influence of confinement on the excitation dynamics and on the other hand there is clear evidence for the presence of singlet fission in rubrene single crystals [142, 143, 144]. In order to analyze the effect of characteristic length scales on the singlet exciton dynamics and in particular on the singlet fission process we measured the temperature dependent PL decay dynamics of three different hierarchies of morphologies — bulk crystals, microcrystals and amorphous thin films (see Figure 4.1). These different types of morphologies inherently exhibit an increasing degree of spatial confinement for the created singlet excitons.

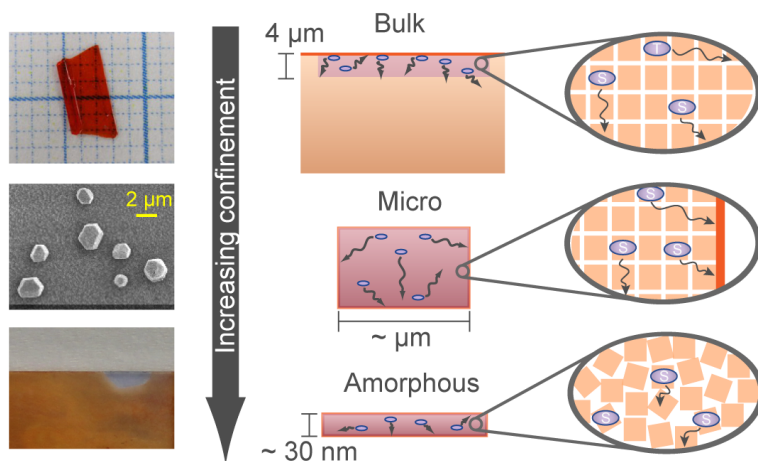


Figure 4.1: The three analyzed rubrene morphologies — i.e. bulk single crystals, microcrystals and amorphous films — exhibiting an increasing degree of confinement for the photoexcited singlet excitons.

Within both crystalline structures (bulk crystal and microcrystals), due to the high molecular order, excitons are expected to be mobile and able to travel large distances before recombining or being quenched at defects or undergoing singlet fission [143]. For rubrene single crystals a lower limit for the diffusion constant of $0.2 \text{ cm}^2/\text{s}$ at 4 K has been deduced by μ -PL measurements and values for other polyaromatic materials can be as high as $10 \text{ cm}^2/\text{s}$ at very low temperatures as determined by transient grating experiments [145, 146]. For

the employed excitation pulses centered at 400 nm the excitation depth can be calculated to be $\approx 4 \mu\text{m}$ [146] while the excitation spot size used in the experiment is around $360 \mu\text{m}$. Excitons created within this volume are only restricted by the top surface of the bulk crystal and can migrate into the crystal volume driven by the excitonic population gradient [142]. For the microcrystals, where excitons are trapped within the μm -sized structures, the spatial confinement is expected to significantly enhance the influence of the boundaries resulting in a change of the exciton decay dynamics. As an example the reduced molecular order at the interfaces might introduce low-energy traps for excitons reaching the boundaries. The amorphous film can be considered as exhibiting the largest degree of confinement as excitons are preferentially localized at a single molecular site, while their motion is significantly hindered by the structural disorder. This reduced singlet exciton diffusion length is in analogy to the observation of a reduced diffusivity of free charge carriers in disordered organic semiconductors [147].

4.2 Optical Sample Characterization

The steady state absorption and PL spectra of rubrene exhibit four dominant peaks (Figure 4.2). For the PL spectra these contributions are centered at approximately 2.16, 2.02, 1.88 and 1.74 eV resembling the dominant vibronic progression of $\approx 140 \text{ meV}$ [148, 149]. The origin of the high-energy peak has been the subject to controversial discussion and it has been assigned to either a charge transfer state [142] or a delocalized excitonic state [146, 150, 151] whereas the lower energetic peaks (2.02, 1.88 and 1.74 eV) are attributed to emission from localized molecular excitons. On the contrary, a recent publication suggests that differences observed in absorption and emission spectra of rubrene micro structures originate from the optical anisotropy of rubrene [152]. In our study we find no indication for the coexistence of two independent emitting species in rubrene. In particular the PL decay dynamics of the high-energy peak for a given temperature are almost identical with those of the lower energetic peaks. Therefore we consider the radiative decay of just one singlet excitonic state with different polarizations to be the only contribution to the measured PL signal.

In general the aforementioned anisotropy of rubrene was found to significantly affect its electronical properties — for example the anisotropy of charge carrier mobility [153] — as well as its optical properties like the absorption coefficient [142] or the exciton diffusion length [143]. These observations result from the herringbone packing of the rubrene molecules (compare Section 3.1.1) leading to different transfer integrals as well as oscillator strengths for the different crystallographic directions [142, 154]. The top graph of Figure 4.3 illustrates the

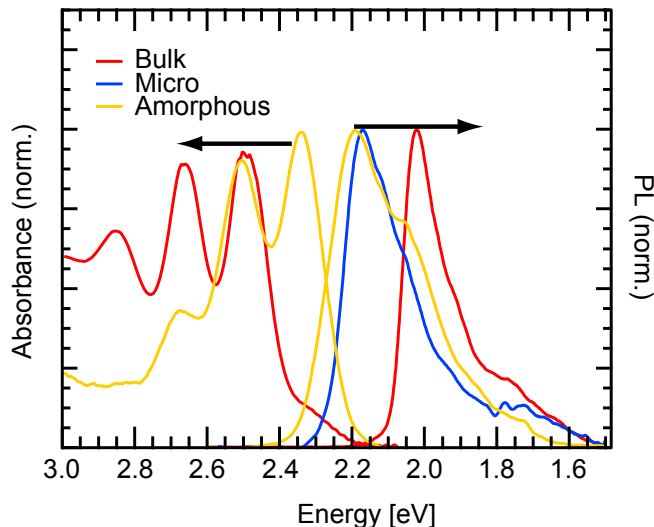


Figure 4.2: Absorption and PL spectra of the three sample morphologies. While the spectral shape of microcrystal and amorphous film PL is similar, the spectrum of the bulk sample differs significantly which might be related to anisotropy effects of the rubrene emission.

influence of anisotropy on the optical properties of rubrene by the example of the absorption coefficient. It can be clearly seen that choosing a polarization of the excitation light that is parallel to the \vec{a} -direction leads to an increase of the detected PL signal by a factor of almost two compared to \vec{b} -polarized excitation. These results are consistent with the larger absorption coefficient found for rubrene for \vec{a} -polarized light [142].

Comparing the time-integrated PL spectra of the bulk crystal and the microcrystals, the high-energy peak at 2.16 eV is significantly enhanced for the microstructures. This change is not the result of a blueshift of the whole spectrum but a redistribution of oscillator strength as is obvious from the lower graph of Figure 4.3. It can be interpreted as a result of the enhanced emission polarized parallel to the \vec{c} -direction from the side facets of the microstructures and reduced self-absorption compared to the bulk crystal [152].

Interestingly, the spectral shape of the microcrystals is very similar to that of the amorphous film. The fundamental difference is that due to the strongly enhanced energetic disorder of the film the peaks are significantly broadened (FWHM \approx 166 meV) compared to the microcrystals (116 meV) and the bulk crystal (102 meV), respectively. Due to the disorder within the film the PL spectrum is expected to be comparable to that of an isolated molecule in solution [155]. The similarity between the PL spectra of the amorphous film and the mi-

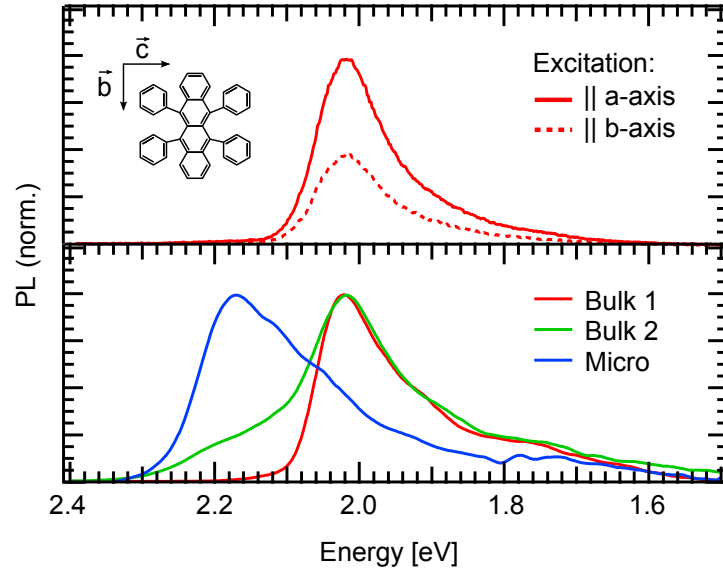


Figure 4.3: Top graph: Detected PL spectra for different polarization of the excitation light indicating the anisotropy of the absorption coefficient. Bottom graph: Comparison of the PL spectra of two different bulk crystals with the microcrystal PL.

crocrystals can be explained by the random orientation of the rubrene molecules within the film compensating for the directionality of emission and the enhanced out-coupling at the edges of the micro structures.

Cooling down the two crystalline morphologies leads to a gradual and pronounced increase of PL intensity and a blueshift corresponding to the reduction in thermal energy (20-25 meV) as shown in Figure 4.4. The amorphous film in contrast shows an initial increase of detected signal followed by a continuously dropping of PL intensity for temperatures below 150 K as well as a general slight redshift known from other disordered organic semiconductors (compare Chapter 5). The peak width for all three different morphologies is reduced with decreasing temperature (Figure 4.5). For the bulk and microcrystals the reduction is of the order of thermal excess energy (≈ 30 meV) and a result of the effective band-narrowing [12]. The temperature dependence of the FWHM for these samples can be qualitatively described assuming a Boltzmann-type temperature dependence of the population of the excitonic states. The strong decay of FWHM below ≈ 50 K might be due to the fact that this temperature range is below the Debye temperature which was found to be $T_D = 60$ K for rubrene single crystals [156]. The thermal energy calculated from T_D of around 5.2 meV as well as the energy associated with the cut-off frequency ω_D are in the energy range

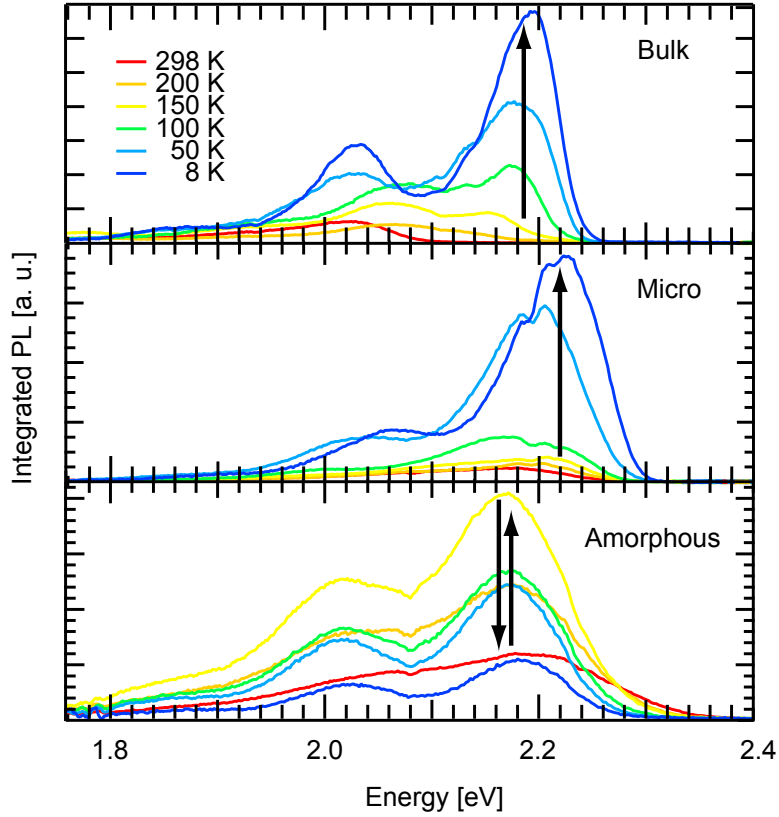


Figure 4.4: Temperature dependent PL spectra of the three morphologies. While both crystalline samples show a gradually increasing intensity, the amorphous film PL shows an initial increase followed by decreasing intensity for temperatures below 150 K.

of prominent lattice phonon modes observed by Raman spectroscopy on bulk rubrene crystals [157]. Hence it can be assumed that at temperatures below T_D these lattice phonon modes start to freeze out which might affect the population of the excited electronic state illustrating its vibronic nature. The associated energies derived from the fits of the two crystalline morphologies of around 1 meV confirm the non-local character of the vibrations coupled to the electronic transition. On the contrary, the amorphous film exhibits a continuous reduction of the FWHM of more than 50 meV which might be due to the inhomogeneous broadening of the transitions resulting from the present local vibrational modes and the energetic disorder of the film. Due to the absence of lattice phonon modes this almost linear decrease of the FWHM is not superimposed by effects resulting from contributions of the non-local vibronic motions.

The increase of the PL signal with reduced temperature points towards the

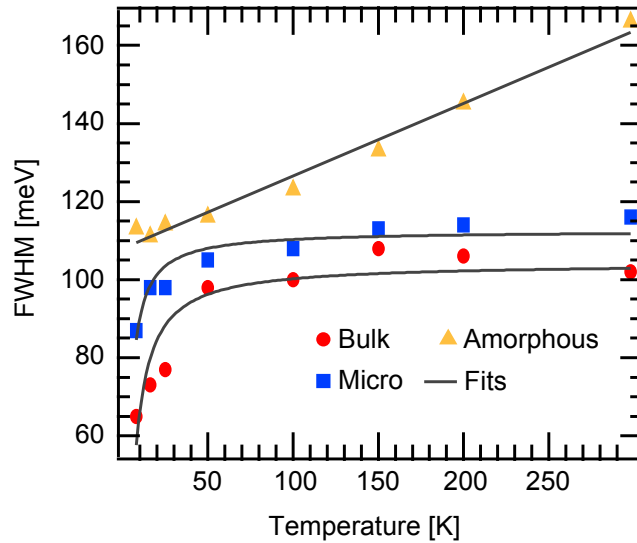


Figure 4.5: The FWHM of the PL peaks of the amorphous film is approximately linearly reduced with decreasing temperature. On the contrary the peak width of both crystalline morphologies stays almost constant for temperatures above ≈ 50 K and is strongly reduced below this temperature.

presence of thermally activated radiationless decay channels. Employing Equation 2.19 and assuming only one dominant radiationless channel the temperature dependence of the PL of both crystalline morphologies can be modeled as presented in Figure 4.6. Note that the values of the PL intensities at a given temperature correspond to the area under the respective peaks of the associated time-integrated PL spectrum. For a given morphology, bulk or microcrystals, both high-energy peak (H) and lower-energy peaks (L) show a similar temperature dependence yielding comparable values for the energy barriers. However, two different barrier heights of $\Delta E_1 \approx 44$ and $\Delta E_2 = 25$ meV are deduced for bulk and microcrystals, respectively (see also Table 4.1). These values are in good agreement with activation energies found for other organic single crystals such as α -PTCDA [158]. The temperature regime where the increase in PL intensities starts to saturate again coincides with the Debye temperature found for rubrene crystals. As discussed above it can be assumed that below T_D prominent lattice phonon modes start to freeze out which might affect the population of the vibronic sublevels of the excited state.

In accordance with the description of the temperature dependent PL intensity for the two crystalline morphologies, the initial rise of the PL signal detected for the amorphous film can be modeled employing the aforementioned equation yielding a barrier energy of $\Delta E_3 = 134$ meV. Here the presented values for the

PL intensity at a given temperature correspond to the area under the whole respective spectrum. The barrier energy is of the order of a molecular vibration thus pointing at the local character of this decay channel. For correctly describing the behavior below 150 K a temperature dependent prefactor Φ depicting the exciton formation efficiency has to be introduced to Equation 2.19 describing the promotion of additional decay channels e.g. by static impurity quenching, by the lack of thermal activation energy.

Comparing the relative spectral changes, i.e. high-energy peak versus lower energetic peaks, as a function of temperature (Figure 4.7) one finds that the

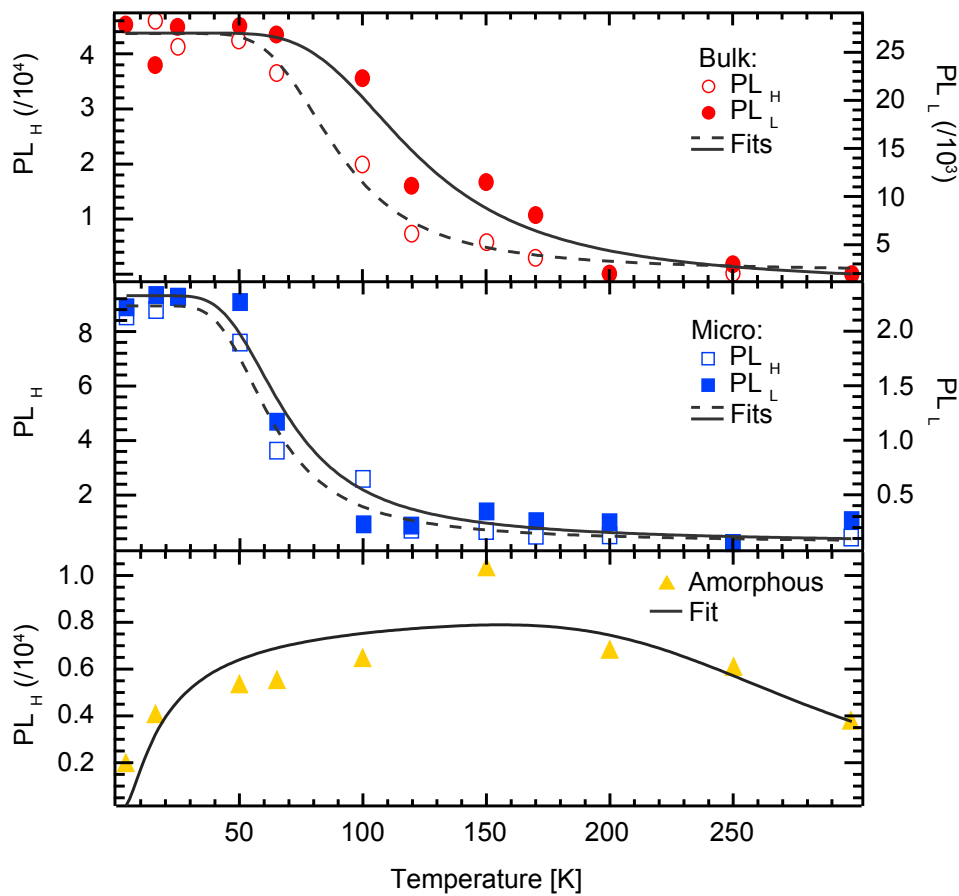


Figure 4.6: The changes of PL intensity as a function of temperature. Here H denotes the area under the high-energy peak and L the area under the lower energetic peaks of the corresponding PL spectrum. The changes can be modeled assuming one dominant but different thermally activated decay channel for each of the three morphologies (fits according to Equation 2.19).

contribution of the high-energy peak is gradually enhanced for the bulk and

micro crystal sample with reducing the temperature. This enhanced contribution follows the same trends as the corresponding absolute changes of the spectra. The fits yield values of $\Delta E_1^{rel.} = 42$ meV and $\Delta E_2^{rel.} \approx 17$ meV, respectively.

In principle the relative spectral changes might indicate the presence of two different emitting species. However, if the high-energy PL peak of both crystalline morphologies was due to emission from another emitting species, for example CT excitons, one would expect values for the energetic barriers $\Delta E_{1,2}^{rel.}$ that differ significantly from the ones derived from the absolute PL changes of the respective spectra. In particular if CT exciton and singlet exciton population were coupled but separated by an energetic barrier (compare Chapter 2) this additional barrier should be identified analyzing the relative PL changes. As this is not the case the results suggest that there is only one emitting species — namely singlet excitons. The observed relative spectral changes might be interpreted as resulting from the fact that the probability of overcoming the activation barriers of the decay channels depends on the excess energy of the generated singlet excitons or the fact that different excitonic states can be populated.

In contrast to the crystalline morphologies the PL spectra of the amorphous film do not show any observable relative changes. Here the relative spectral contributions of the different peaks stay fixed. This finding again underlines the different character of this morphology which is expected to be governed by the structural disorder and it indicates the presence of a different type of decay mechanism which is in agreement with the significantly higher energy barrier found for this morphology.

4.3 Exciton Dynamics

Following the analysis of the time-integrated spectra this section will focus on the PL decay dynamics as a function of temperature. This complementary set of information allows for the identification of the elementary decay channels for singlet excitons in rubrene which proves to be in tight correlation with the respective degree of spatial confinement. Applying the model of thermally activated radiationless decay channels utilized in the previous section, the PL decay rate for the bulk morphology is described assuming three distinct decay mechanisms characterized by their respective decay times $\tau = \gamma^{-1}$:

$$\gamma = \gamma_r + \gamma_{nr}^{(1)} e^{-\Delta E_1/kT} + \gamma_{nr}^{(2)} e^{-\Delta E_2/kT} + \gamma_{nr}^{(3)} e^{-\Delta E_3/kT} . \quad (4.1)$$

Here γ_r denotes the radiative decay to the ground state, γ_{nr}^i the respective non-radiative channel and ΔE_i the value of the associated energy barrier. The PL transients can therefore be described assuming a triexponential decay. It is important to note that the fluence used for all time-resolved PL experiments was 2.6

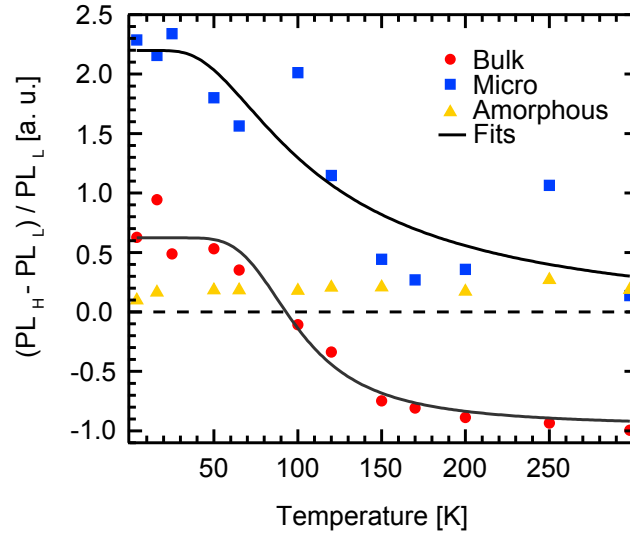


Figure 4.7: The relative spectral changes (high-energy peak versus lower energy peaks) for the crystalline samples follow the trends of the respective absolute changes while the amorphous PL spectra do not show relative changes (fits according to Equation 2.19).

nJ/cm^2 which corresponds to an excitation power of around $200 \mu\text{W}$. As the PL decay dynamics of the bulk crystal at a given temperature are found to be independent of the excitation power as well as the probe energy (see Figure 4.8 (a)), the detected emission can be solely attributed to the radiative recombination of singlet excitons. Furthermore the detected initial PL intensity around zero delay scales linearly with excitation power (Figure 4.8 (b)). This observation allows us to exclude bimolecular processes as additional decay pathways as well as the influence of delayed fluorescence result of triplet fusion processes for the analyzed time window [144].

The PL decay of the bulk morphology at room temperature (Figure 4.9 top graph) is dominated by a radiationless decay channel with a time constant of 20 ps ($1/\gamma_{nr}^{(1)}$). This observation is consistent with the picosecond component found by Stöhr et al [146]. In addition a second channel with an associated time constant of 100 ps ($1/\gamma_{nr}^{(2)}$) is present but has a much smaller contribution to the overall decay. The time constant for the dominant decay channel for the bulk morphology as well as its estimated activation barrier of $\Delta E_1 \approx 44 \text{ meV}$ are in excellent agreement with the reported time constant for singlet fission in rubrene single crystals and the associated offset between the first excited singlet state S_1 and the summed-up triplet energy $T_1 + T_1$ [155, 159]. A second $\approx 2 \text{ ps}$ time constant found by Ma et al. [155] cannot be observed in the measurements,

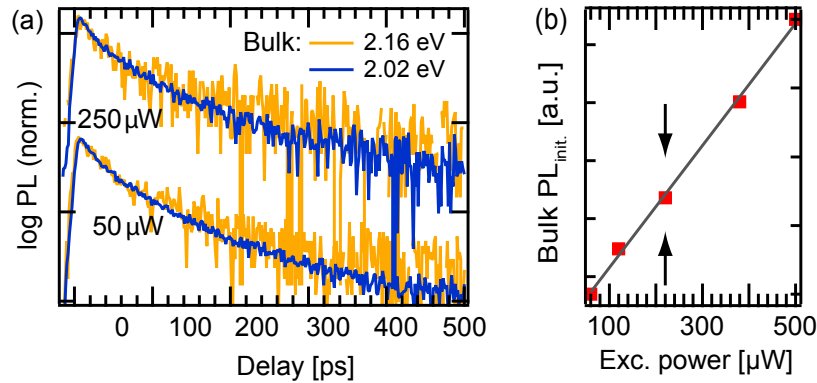


Figure 4.8: (a) The decay dynamics measured for the bulk morphology at room temperature are found to be independent of excitation power as well as probe energy. This indicates the presence of just one emitting species. (b) The initial bulk crystal PL signal height scales linearly with the excitation power indicating the absence of bimolecular decay mechanisms in the regime used in the measurements (arrows indicate the excitation power used for the presented measurements).

presumably due to the temporal resolution of our setup.

Interestingly, the decay channel with the 20 ps time constant cannot be identified for the microcrystal morphology. Here the dynamics are governed by the 100 ps decay time in agreement with the 25 meV activation barrier found for the temperature dependent time-integrated PL spectra of the microcrystals. These findings can be considered as the direct manifestation of the spatial confinement of singlet excitons within the crystals and points towards a surface or interface related quenching mechanism, respectively. This assumption is supported by the absence of lattice vibrational modes in the energy range around 25 meV as examined by Raman spectroscopy [157] indicating a local quenching mechanism. Tao et al. found a transient absorption feature with a rise time of 100 ps for single crystalline rubrene and assigned it to polaron formation upon exciton dissociation [160]. Although not being able to identify the nature of the dissociation mechanism Tao et al. mention that their results point towards a material-inherent mechanism. This statement is in agreement with the assumption of a surface or interface related quenching mechanism. However, probing in the same wavelength range Furube et al. reported exciton generation with a rise time of 10 ps [161]. Another plausible loss mechanism explaining the 100 ps channel is the conversion of excitons into dark states, i.e. excitonic states with optically forbidden transitions, at the interfaces. This scenario resulting from the local molecular disorder at the boundaries has been theoretically predicted

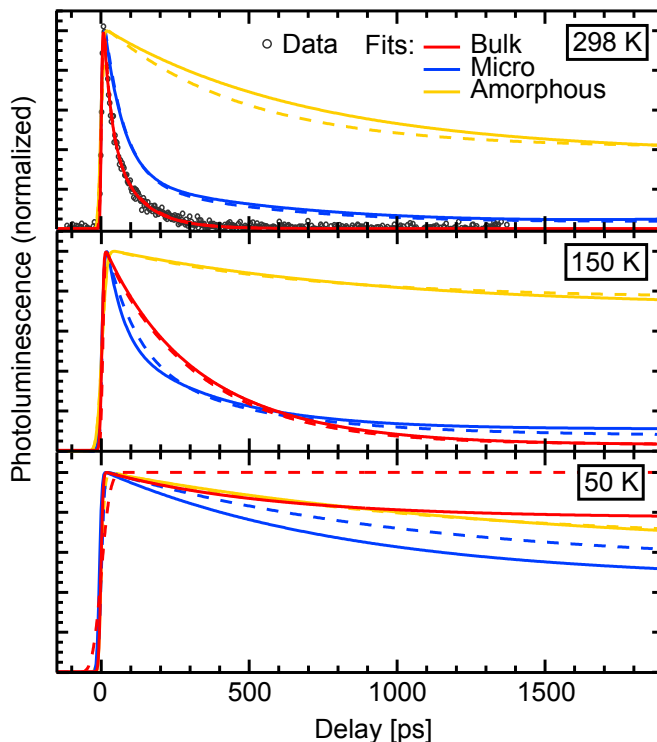


Figure 4.9: Transients recorded at 2.16 eV (dashed lines) and 2.02 eV (solid lines) for the three morphologies as a function of temperature. The slower decay at lower temperatures clearly indicates the presence of thermally activated radiationless decay channels.

for several hydrocarbons [24]. It is important to mention that due to the precipitation growth method the microcrystals might exhibit a slightly larger amount of defects compared to the bulk crystal that might lead to the presence of subdomains. Since - especially for excitons generated far from the interfaces - the interaction with quenching sites at grain boundaries or dislocations as well as local defects has to be taken into account. In addition — since we measured an ensemble of microcrystals — the degree of crystallinity as well as the spatial extent of the crystals might slightly vary. Therefore, considering the large diffusion constants found for polyaromatic systems a major part of singlet excitons is expected to reach an interface before undergoing the singlet fission process. At these interfaces, due to the difference in activation energy between $1/\gamma_{nr}^{(1)}$ and $1/\gamma_{nr}^{(2)}$ of a factor of two, singlet fission is effectively suppressed and the decay of the singlet excitons is dominated by the surface quenching mechanism. This results in an enhanced effective exciton lifetime by a factor of five for the microcrystalline morphology (see Figure 4.9 top graph). The promotion of the

surface/interface quenching channel might be also due to the fact that the singlet fission rate is reduced at these interfaces compared to the bulk as a result of the increased degree of disorder. This assumption is supported by the observation of a significantly smaller singlet fission rate in amorphous rubrene films reported by Bardeen and coworkers [162].

Analyzing the PL decay dynamics in bulk rubrene crystals Wen et al. report a 6.2 ps component attributed to singlet fission and a second time constant of 47 ps [163]. While the fast channel cannot be detected due to the temporal resolution of our setup, the 47 ps time constant is significantly larger than the 20 ps fission channel observed for bulk crystals in this work. The slower ps channel together with the associated activation barrier of 30 meV determined by Wen et al. point towards a stronger contribution by interface quenching and illustrates the impact of morphological details on the exciton dynamics.

The third time constant present at room temperature of ≈ 0.5 ns ($1/\gamma_{nr}^{(3)}$) is almost negligible for the bulk morphology but becomes relevant as decay path for excitons within the microcrystal structures. It is in the range of the effective radiative lifetime at room temperature [97, 146, 150] (intrinsic radiative lifetime 16.5 ns [164]) and results from quenching at inhomogeneities within the crystal. Therefore the increased contribution of this channel for the microcrystals compared to the bulk morphology might indicate a lower crystalline quality of the microcrystalline structures presumably caused by the faster growth speed occurring for the precipitation method.

For the amorphous film the decay at room temperature can be described by assuming solely the channel $\gamma_{nr}^{(3)}$. This observation can be interpreted as being the result of the strongly localized character of the excited states. The decay dynamics completely change as soon as a significant amount of interfaces is introduced to the film morphology (Figure 4.10 (a)). Although being of comparable height (≈ 30 nm) and of similar surface flatness, an amorphous rubrene film prepared on a glass substrate exhibits a strongly increased interface-to-volume ratio. The increased ratio is due to additional dislocations and grain boundaries. On the contrary an amorphous film on sapphire only shows smooth surface plateaus (Figure 4.10 (b)). The increase of surface area results in the introduction of the additional rate $\gamma_{nr}^{(2)}$ which dominates the PL decay of the amorphous film on glass. For the amorphous film on sapphire this channel cannot be observed. This finding can be explained by the fact that the number of singlet excitons generated close to boundaries is significantly enhanced for the film on glass increasing the total number of excitons reaching trapping sites during migration and subsequently being quenched. Although being derived for the amorphous morphology these results indicate a direct correlation between the presence of the 100 ps channel and the significant increase in interface area which strengthens the assignment of this channel to a surface quenching mechanism. In addition, as the decay time

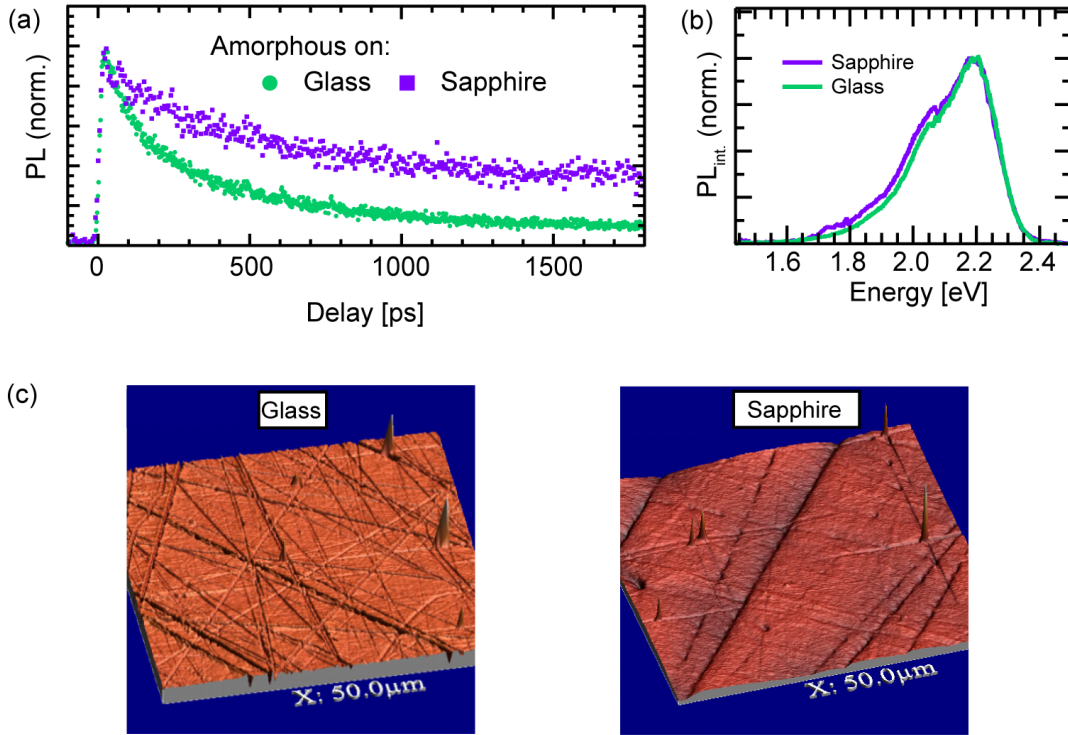


Figure 4.10: (a) The PL decay of the amorphous film crucially depends on the substrate used while the spectral shape (b) remains unaltered. (c) The changes in the decay dynamics can be directly correlated with the amount of grain boundaries and dislocation the film sample exhibits.

is identical with the dominant time constant found for the microcrystals it can be assumed that the involved channels are comparable and moreover that the mechanism depicted by $\gamma_{nr}^{(2)}$ is of general nature and not morphology specific.

Piland et al. observed an additional time constant for amorphous rubrene films of around 2.2 ns [162] but as the presented time-resolved measurements are restricted to a 2 ns window and in addition the reported time constant is of the order of the exciton lifetime we probably cannot identify this component. Although the triplet yield is expected to be low due to a small inter-system crossing rate [155, 165] Piland et al. report the presence of triplet excitonic states in the amorphous film and they assign the 2.2 ns decay time to the presence of a singlet fission mechanism [162]. Compared to the studies by Ma et al. [155] and the results presented by us, this rate is smaller by two orders of magnitude which might be explained by the influence of structural disorder on the fission process. Another possible explanation could be that the mechanism itself is of different nature.

As a consequence of the thermally activated character of the radiationless decay channels, reducing the temperature results in an increase of the average lifetime of singlet excitons within the bulk and the microcrystal morphologies. Around 150 K the picosecond channels start to freeze out as the phonon density is diminished (Figure 4.9 middle graph) and at even lower temperatures (Figure 4.9 bottom graph) $\gamma_{nr}^{(3)}$ represents the only remaining radiationless decay channel. In this temperature regime the transient behavior of both crystalline morphologies is comparable to the decay dynamics of the amorphous film. Further reducing the temperature results in an increase of the observed average exciton lifetime since exciton diffusion is hindered making quenching events at inhomogeneities less common. These lifetimes are of the order of several nanoseconds which is in agreement with literature [144, 146, 150], but cannot be determined more precisely due to the 2 ns detection window of the measurement. Comparing the transients at 50 K however indicates that the lifetime of singlet excitons generated within the microcrystals is slightly reduced compared to the other two morphologies. This might be due to the enhanced influence of the interfaces especially compared to the bulk crystal.

For temperatures > 50 K the decay dynamics of the high-energy peak (dashed lines in Figure 4.9) and the lower-energetic peaks (solid lines in Figure 4.9) are identical while for temperatures ≤ 50 K the lifetimes derived from the high-energy peak are slightly larger for both crystalline morphologies. This observation coincides with the increased relative contributions of the high-energy peaks to the corresponding PL spectra with decreasing temperature. It might again be interpreted as a consequence of the difference in the exciton excess energy affecting the influence of the thermally activated decay channels.

In order to analyze the slower ns decay dynamics within crystalline rubrene also the PL decay within a 10 ns window was measured for bulk rubrene. Figure 4.11 shows a transient taken at 2.02 eV at room temperature. Most of the PL signal decays within the temporal resolution of this measuring mode which is around 150 ps. According to the previously presented results this initial decay is expected to be dominated by the 20 ps component which cannot be resolved. A second slower time constant that is present can be identified with $\gamma_{nr}^{(3)}$ but its contribution is very small. We find no indication of the 2.2 ns singlet fission channel reported for amorphous rubrene films [162] indicating that the decay mechanism associated with this channel is only present in the disordered rubrene morphology. The decaying PL signal is overlapped by a very slowly decaying component with a time constant > 10 ns that results in an effective offset of the whole transient. This long-lived component can be interpreted as resulting from singlet emission as well as delayed fluorescence due to triplet fusion [144]. Being limited by the dynamic range of the streak camera, these slow dynamics could not be analyzed in more detail in this work.

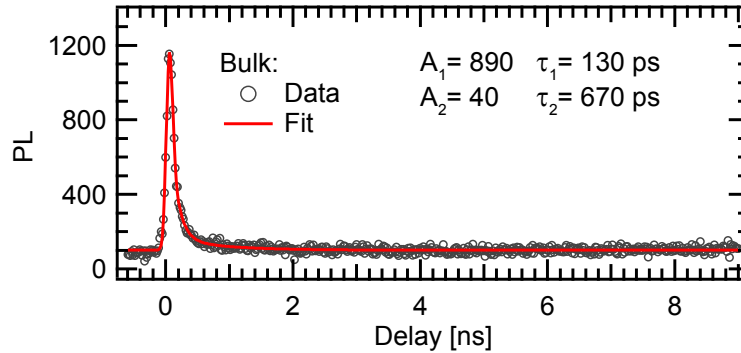


Figure 4.11: Transient taken at 2.02 eV at room temperature for the bulk rubrene single crystal applying a 10 ns delay time-window. The dynamics are dominated by an initial decay within the temporal resolution of the measuring modus.

4.4 Nanocrystalline Rubrene Film

The model describing the exciton dynamics in rubrene deduced from the careful analysis presented in the preceding sections now can be employed for a nanocrystalline rubrene film. Films of rubrene were found to grow nanocrystalline on sapphire substrates if a pentacene buffer layer of at least one monolayer was deposited prior to the rubrene film using molecular beam epitaxy [166]. Figures 4.12 (a) and (b) show the absorption and emission spectra of the pentacene-rubrene film (Pen/Rb film) analyzed in this work, respectively. For comparison also the absorption spectra of the bulk crystal and amorphous film as well as the emission spectra of the amorphous film and the microcrystals are shown. Qualitatively both the shape as well as the peak width of the absorption and PL spectra of the crystalline film are comparable to those of the amorphous film. In particular the FWHM of the Pen/Rb film PL peaks is bigger than that of the microcrystals indicating a significant contribution of disordered regions to the nanocrystalline film emission. At this point it has to be mentioned that PL from the pentacene layer is expected to contribute to the spectrum below ≈ 1.9 eV explaining relative changes in this spectral region compared to the PL spectra of the two other morphologies. In contrast to the optical studies however, the presence of nanocrystals within the Pen/Rb film is clearly indicated by the Bragg peaks appearing in its XRD diffractogram (Figure 4.13 (a)). The height of these crystals can be calculated from the FWHM of the (001) peak and the derived value of ≈ 44 nm is of the order of the film thickness of around 30 nm. This means that the measured pentacene-rubrene film probably exhibits both: amor-

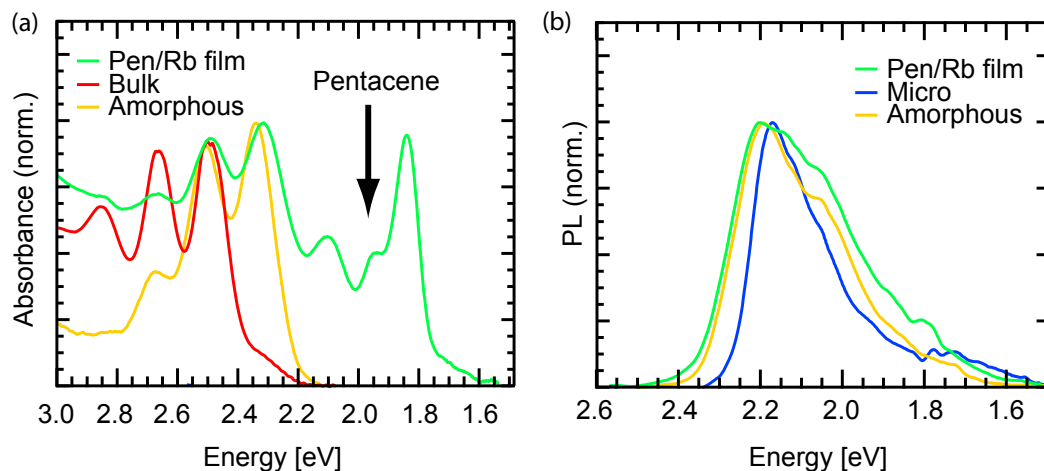


Figure 4.12: Comparison of the absorption (a) and PL (b) spectra of the nanocrystalline pentacene-rubrene film (green) with the previously discussed rubrene morphologies. The spectra of the Pen/Rb film are found to be similar to the corresponding spectra of the amorphous film.

phous regions and nanocrystals (see Figure 4.13 (b)). This type of morphology is similar to the one present in many polymer systems (compare Chapters 2 and 5).

Figure 4.14 shows the decay dynamics measured for the Pen/Rb film. The recorded transient looks like an intermediate between the respective transients of the microcrystals and the amorphous film. The decay is found to be biexponential with time constants of around 100 ps and 0.5 ns, respectively while the amplitude ratio is around 1:1. Whereas the PL decay of the amorphous film only exhibits the slower 0.5 ns component, both time constants can also be found for the microcrystals. Here however, the dynamics are dominated by the 100 ps time constant resulting in an amplitude ratio $A_{100 \text{ ps}}/A_{0.5 \text{ ns}}$ of around 3:1. These findings indicate that in the nanocrystalline film amorphous and nanocrystalline regions coexist. Due to the intermediate character of the Pen/Rb film the PL decay dynamics are influenced by the quenching at interfaces (100 ps) and local inhomogeneities/impurities (0.5 ns) at equal measure. As the influence of the interfaces is expected to be enhanced for the Pen/Rb film compared to the microcrystals, in particular by the significant amount of interfaces between crystalline and amorphous regions, a contribution of the 20 ps component, cannot be observed. This finding again indicates that the presence of singlet fission in rubrene critically depends on the morphology of the analyzed sample. Furthermore the presented results confirm the microscopic model describing the decay

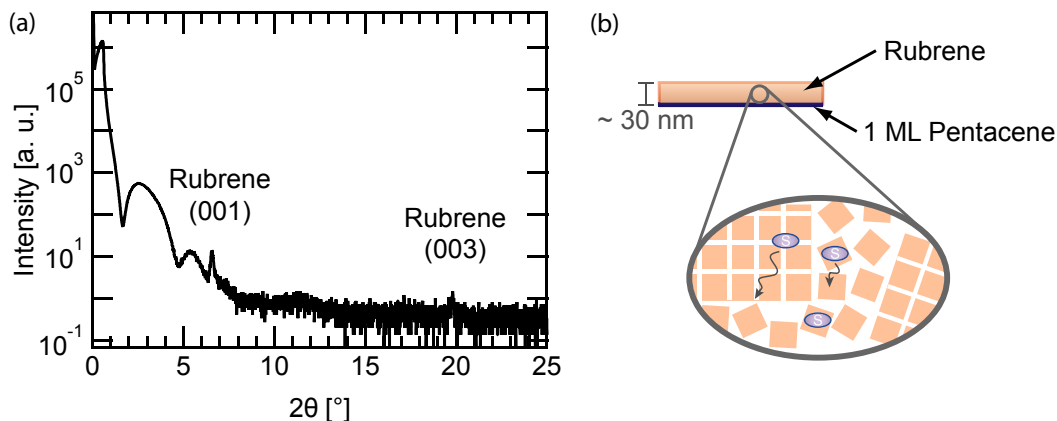


Figure 4.13: The XRD diffractogram (a) clearly indicates the presence of crystallites within the film. (b) Therefore the crystalline film can be assumed to exhibit nanocrystallites embedded in an amorphous surrounding representing an intermediate case between an amorphous sample and a spatially confined crystalline sample.

dynamics in various rubrene morphologies that has been derived in the preceding section. It can be speculated that this model allows for a prediction of the decay dynamics if the morphology of the rubrene sample is known.

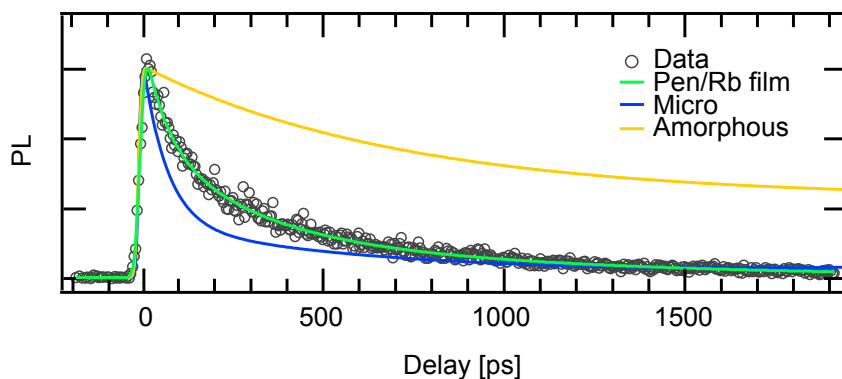


Figure 4.14: Comparison of the PL decay of the crystalline rubrene film with the decay dynamics measured for the amorphous film and the microcrystals.

4.5 Summary

In this chapter it was shown that the inherent length scales of different rubrene morphologies have a significant impact on the decay dynamics of photogenerated singlet excitons within these structures. The temperature and time-dependent PL characteristics can be described by assuming the presence of three thermally activated non-radiative decay channels and their respective predominance in the various morphologies (see Figure 4.15). The non-radiative decay in rubrene sin-

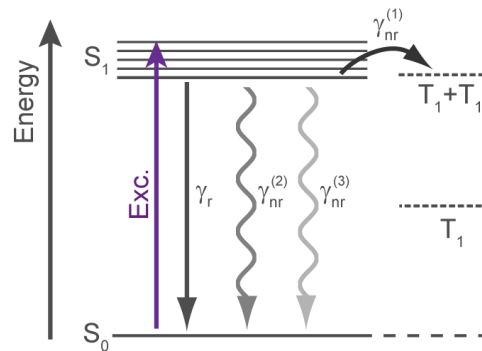


Figure 4.15: Energy level scheme illustrating the dominant decay channels in rubrene single crystals.

gle crystals is dominated by singlet fission with a time constant of 20 ps and an associated energetic barrier of ≈ 44 meV resembling the energetic offset between the S_1 and the $T_1 + T_1$ state. This channel is effectively suppressed if interfaces are accessible for excitons as being evident from the analyzed decay dynamics of rubrene microcrystals. It can be assumed that in the micro structures most of the excitons reach the interfaces or domain boundaries and subsequently undergo quenching by dissociating into charges or being converted into dark excitonic states within 100 ps. Since the 100 ps channel has an activation energy of only half the singlet fission barrier, the latter process is effectively suppressed. A third relaxation channel with a time constant of ≈ 0.5 ns becomes only relevant for highly ordered rubrene systems at low temperatures. This channel can be identified with quenching at inhomogeneities and its local character is confirmed by the activation barrier which is close to the dominant vibrational mode found for rubrene. It is the only radiationless decay mechanism to be found in amorphous rubrene where excitons are preferentially localized on molecular length scales and their migration is hindered by the structural disorder. The observed time constants and associated energy barriers of the three identified decay channels are summarized in Table 4.1.

76 Chapter 4. Influence of Local Environment on Exciton Dynamics

The vibronic nature of the energetic levels associated with the optical transitions is indicated by the saturation of the PL intensity and the strong reduction of PL peak width observed for the crystalline rubrene morphologies when decreasing the Debye temperature of around 60 K. The associated cut-off frequency is in the energy range of characteristic lattice vibrational modes identified for bulk rubrene crystals indicating the influence of non-local vibrational motions on the electronic structure of rubrene crystals.

As the dimensions influencing the exciton dynamics in rubrene are found to be on typical length scales of organic thin film devices this correlation has to be taken into account for the ongoing optimization and miniaturization of organic optoelectronic devices. In particular the presented results indicate that the presence of interfacial states within triplet-based photovoltaic blends — for example at the D-A interface, between ordered and disordered regions within the polymer face or introduced by defects or impurities — might suppress the desired singlet fission process.


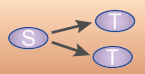

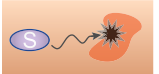
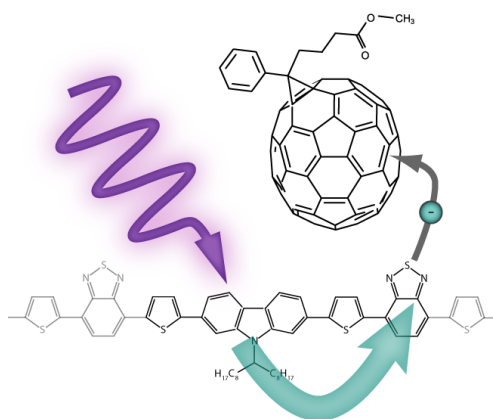
							
sample type	$1/\gamma_r$	$1/\gamma_{nr}^{(1)}$	ΔE_1 [meV]	$1/\gamma_{nr}^{(2)}$	ΔE_2 [meV]	$1/\gamma_{nr}^{(3)}$	ΔE_3 [meV]
bulk	few ns	20 ps	44	100 ps	25	~ ns	134
micro	few ns	—		100 ps	25	~ ns	134
amorphous	few ns	—		—		~ ns	134

Table 4.1: Parameters for the energetic barriers and the lifetimes (inverse rates) determined from the analysis of the temperature dependence of the integrated spectra and PL transients describing the sub-ns to ns dynamics in the different rubrene samples. The lifetimes in bold letters correspond to the dominant channel at room temperature found for each type of morphology.

Excitation Dynamics in Low Band Gap Donor-Acceptor Copolymers and Blends



5.1 Third Generation Polymers

The synthesis of new copolymer donor materials has proven to be one of the most successful approach for improving the efficiency of organic solar cells. The basic idea behind these new polymers is the combination of at least two different functional comonomer units in order to tune and optimize the optical and electrical properties of the donor (see Section 3.1.2). In general this concept represents a completely novel route for molecular engineering compared to the existing monomer-based donors as for example P3HT. Due to this reason the copolymer donors are also termed third generation polymers [40] while the standard phenylene-vinylene or thiophene based materials are called second generation polymers. While the enhanced device performance of copolymer-fullerene solar cells is obvious only little is known about the intrinsic processes following the photoexcitation of these blends. This aspect is primarily due to the complexity of the repeat units these new materials are comprised of. However, to further

optimize third generation polymers it is of great importance to understand the excitation dynamics of these systems.

In this chapter the nature of the excited states and the relaxation dynamics following photoexcitation of the copolymer PCDTBT (Figure 5.1) are analyzed by means of steady state absorption and PL as well as time-resolved PL measurements. All steady state measurements were carried out in the liquid phase with the molecules dissolved in chloroform unless otherwise noted. For the absorption measurements a JASCO V-670 UV/Vis/NIR spectrometer was employed while for the PL studies a PTI (Photon Technology International) QM-2000-4 fluorescence spectrometer with a cooled photomultiplier (R928 P) and a 75 W Xe short arc lamp (UXL-75XE, Ushio) was used. The time-resolved PL measurements were carried out using the aforementioned streak setup (Section 3.3).

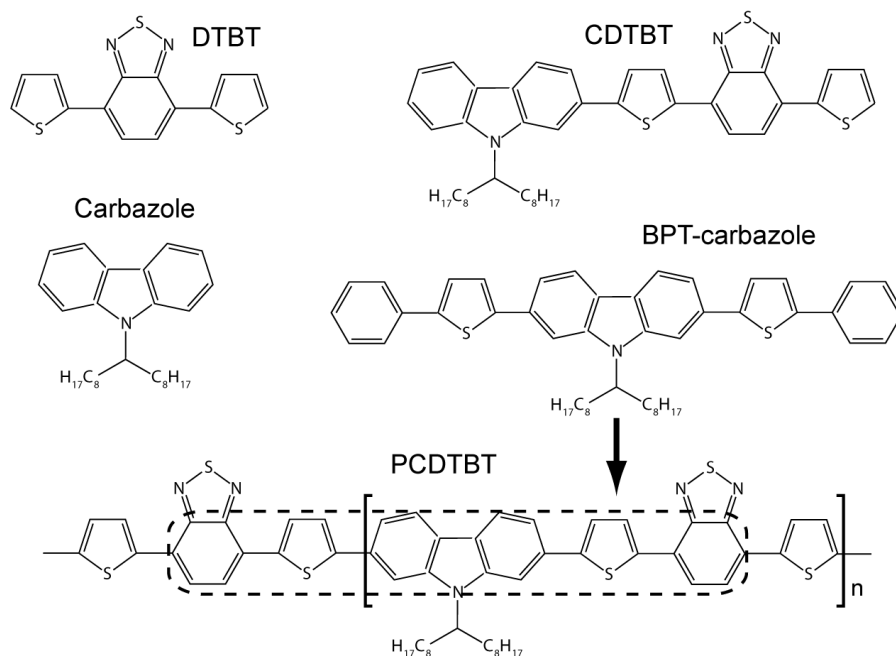


Figure 5.1: Molecules analyzed within the comparative steady state absorption and PL study. Carbazole and DTBT are the fundamental building blocks yielding the CDTBT repeat unit while BPT-carbazole resembles a segment of the PCDTBT backbone without the thiadiazole groups.

PCDTBT is a prominent member of the carbazole-based D-A copolymers (see Section 3.1.2). These polymers, in contrast to typical second generation polymers, exhibit two distinct absorption bands that have been assigned to π - π^* transitions into the first and second excited singlet state [167]. The nature of both electronic levels was reported to exhibit a CT character [168] while theoretical

calculations for the polyfluorene-based copolymer DiO-PFDTBT indicated that only the lower-energy excited state has CT character [169].

We identify the two prominent absorption bands by carrying out a comparative absorption and PL study of PCDTBT and its building blocks used for the synthesis [109], the monomers carbazole and 4,7-di(thien-2-yl)-2,1,3-benzothiadiazole (DTBT), the repeat unit (comonomer) N-(1-octylonyl)-2,7-carbazole-alt-5,5-[4',7'-di(thien-2-yl)-2',1',3'-benzothiadiazole] (CDTBT) as well as the newly synthesized molecule N-(1-octylonyl)-2,7-bis-[(5-phenyl)thien-2-yl]-carbazole (BPT-carbazole) (see Figure 5.1). BPT-carbazole resembles a segment of the PCDTBT backbone with a carbazole group in the center but without the thiadiazole groups. The latter molecule is required to prove whether the copolymer exhibits CT character or not as we will see in the following section.

5.2 Comparative Steady State Absorption and PL Study

For PCDTBT the two prominent absorption maxima are found at around 390 and 560 nm, respectively (Figure 5.2 top graph). Comparing the absorption spectrum in solution with the thin film spectrum, the latter exhibits a slight redshift and broadening of the low-energy band (LEB) while the high-energy band (HEB) remains unaltered. The spectral changes upon thin film formation indicate the sensitivity of the LEB to interchain coupling effects [49] compared to the HEB. Both building blocks — carbazole and DTBT — exhibit an absorption band in solution at approximately 308 nm and an additional band below 280 nm which is the typical wavelength regime for benzene absorption [170] (Figure 5.2 middle graph). Only DTBT exhibits an additional absorption peak at 446 nm. This peak has a broad and featureless shape that is typical of benzothiadiazole containing molecules and polymers [171]. Linking both building blocks to synthesize the CDTBT repeat unit results in an absorption spectrum that looks very similar to the DTBT absorption (see Figure 5.2 bottom graph). The striking difference is the redshift of approximately 40 nm for the CDTBT spectrum which can be explained by the delocalization of π -electrons due to the spatial overlap of the electronic wave functions of both monomer units [46]. In addition a slight broadening of the absorption bands of CDTBT compared to DTBT can be observed. This observation is possibly due to conformational isomerism of the repeat unit molecules. Especially the shape of the LEB of CDTBT is nearly identical to the one of the DTBT comonomer thus indicating the same origin of the latter which is supported by calculations by Heeger and coworkers [168]. Considering the absorption of carbazole, the high-energy absorption of CDTBT below 280 nm and the shoulder of the HEB at around 300 nm can be inter-

puted as originating from the carbazole unit. However, it is important to notice

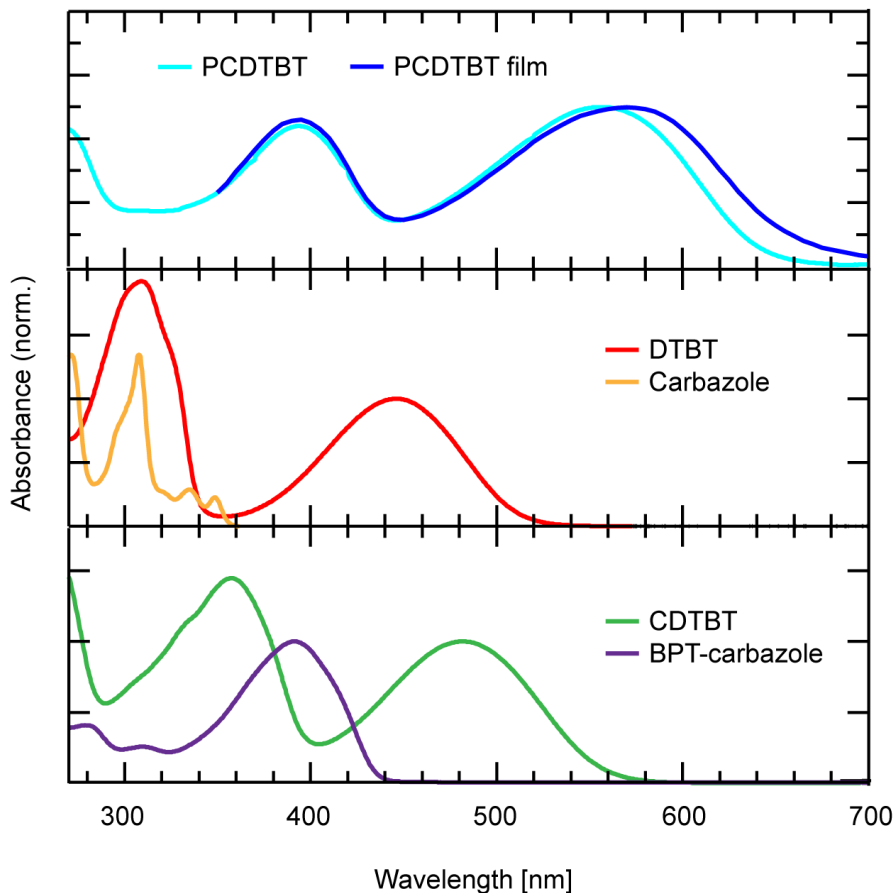


Figure 5.2: Comparison of the absorption spectra of PCDTBT in solution and thin film (upper graph) with its building blocks (middle graph), as well as the repeat unit and BPT-carbazole in solution (lower graph). The low-energy absorption band present in the DTBT spectrum is similar in shape to the low-energy bands present in both CDTBT and PCDTBT spectra.

that the resulting CDTBT spectrum cannot be seen as a simple superposition of the two monomer spectra. Upon polymerization the two distinct absorption bands that are already present in the spectra of DTBT and the CDTBT repeat unit are preserved (compare Figure 5.2 upper graph). The distinct redshift of around 70 nm that can be observed for PCDTBT compared to CDTBT can again be attributed to the increased delocalization of the π -electrons. Apart from the redshift both peaks are slightly broadened which might be due to an effective distribution of conjugation lengths within the copolymer chains, which is an often reported phenomenon for other polymers such as P3HT [172, 173].

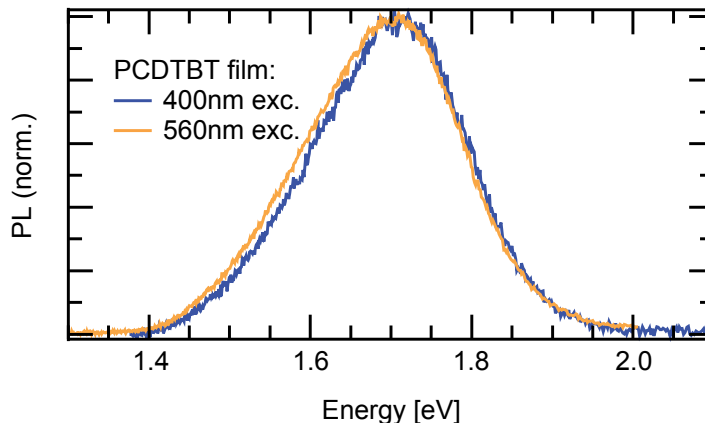


Figure 5.3: The emission from PCDTBT is independent from the excitation wavelength indicating the existence of a final emissive state.

In general, the relative contribution of the LEB to the absorption spectrum, i.e. the oscillator strength of this transition, continuously increases from DTBT to CDTBT and finally to PCDTBT.

The shape and spectral position of the PL from PCDTBT is independent of the excitation wavelength and in particular does not depend on whether one excites the LEB or HEB. As indicated in Figure 5.3 both PL spectra, the one resulting from excitation centered at 398 nm as well as the one resulting from excitation centered at 560 nm, are almost identical. This finding implies the presence of an initial efficient relaxation mechanism from the second to the first excited electronic state followed by the radiative decay to the ground state. According to the analysis of the absorption spectra of PCDTBT and its subunits, such a relaxation mechanism should be present in all analyzed molecules containing the benzothiadiazole group. Indeed, comparing the PL spectra (Figure 5.4) the shapes of DTBT, CDTBT and PCDTBT PL one finds that they are almost identical but gradually shifted to higher wavelengths due to the increased spatial extent of the delocalized π -electron system. Concerning the spectral broadening of the peaks, the same trend as for the absorption spectra is observed for the PL spectra going from DTBT to PCDTBT. Nevertheless, the similarity of these spectra strongly indicates a common emissive state for all of these molecules. The carbazole PL in contrast has a completely different shape and spectral position compared to the other building blocks.

The shape of the PL spectra of DTBT, CDTBT and PCDTBT at room temperature is structureless but asymmetric with a steeper edge at smaller wavelength. When reducing the temperature of the PCDTBT film down to 4.2 K,

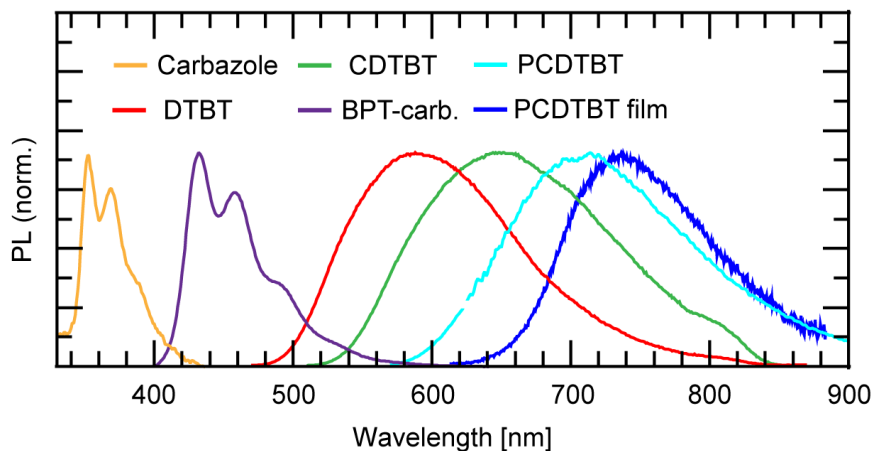


Figure 5.4: Comparison of the PL spectra of PCDTBT and its building blocks. The similar shape of emission from all molecules containing benzothiadiazole indicates that the emissive state is related to this functional group.

however a vibronic progression becomes visible (Figure 5.5 left hand graph). In addition the low temperature spectrum of PCDTBT is redshifted by ≈ 20 meV which is of the order of the loss of thermal excess energy of the system. Both spectra can be fitted assuming three Gaussian peaks representing the three dominant vibronic transitions to the ground state (Figure 5.5 right hand graph). The resulting vibronic progression found is about 150 meV which is in the range of typical breathing modes found for polymeric systems [12, 48]. The FWHM of the peaks is reduced by ≈ 80 meV when cooling down to 4.2 K which is possibly due to a dynamic inhomogeneous broadening of the transitions indicating the influence of vibrational modes on the electronic properties of the system, i.e. the electron-phonon coupling. It has to be mentioned that the low-energy part of the spectrum is possibly influenced by the self-absorption of the optically thick film sample in this range resulting in an altered spectral shape of the high-energy edge (see also section 5.4).

Since the emissive state is supposed to be the same for all molecules containing benzothiadiazole, the same dominant vibronic progression should be found when fitting the spectra. As shown in Figure 5.6 fitting the spectra of DTBT, CDTBT and PCDTBT assuming one dominant vibronic progression yields a spacing of ≈ 170 meV which is similar to the value found for the PCDTBT film. In addition the trend of the increasing spectral width of the PL spectra going from DTBT to PCDTBT is supported by the increase in peak width (FWHM) found for the fits. These results strengthen the assumption that there is one common emissive state for all of these molecules. The number of peaks found to contribute

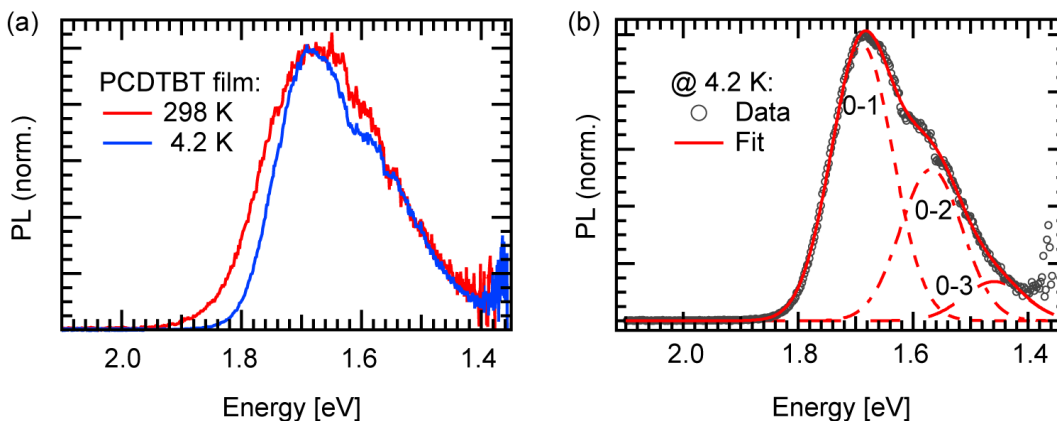


Figure 5.5: (a) While being quite unstructured at room temperature, the PL spectrum of a PCDTBT film at 4.2 K exhibits a vibronic progression. (b) The film spectra can be modeled assuming three Gaussian shaped vibronic transitions with a spacing of around 150 meV.

to the film PL spectrum is smaller than the one found for the PL spectra in solution which might be due to the fact that the detector used for measuring the film PL underestimates the low-energy part while the high-energy part of the spectrum is attenuated by self-absorption of the optically thick film and thus also underestimated. As a result the actual shape of the spectrum is altered and additional peaks contributing to the PL at the high- and low-energy edge might not be detected properly (see also section 5.4). This fact might also explain the slight deviation from the values found for the vibronic progression.

For examining the origin of the two absorption bands in more detail and for being able to identify their nature as well as the coupling mechanism involved, we analyzed the absorption and PL spectra of the newly synthesized molecule BPT-carbazole (Figure 5.1). As already mentioned this molecule resembles a segment of the copolymer backbone, i.e. a segment centered around a carbazole group with phenyl instead of benzothiadiazole units. As a result of the missing thiadiazole group the LEB of PCDTBT completely vanishes in the absorption spectrum of BPT-carbazole (see Figure 5.7). This observation directly points towards a connection between the LEB and the presence of the benzothiadiazole unit in the copolymer. The HEB of PCDTBT, however, is almost identical with the lowest absorption band of BPT-carbazole. This indicates that the HEB of PCDTBT can be described by an excited state which is mainly delocalized along this backbone segment. The BPT-carbazole PL spectrum is in shape similar to the one of polycarbazole [174]. The fact that the BPT-carbazole PL spectrally

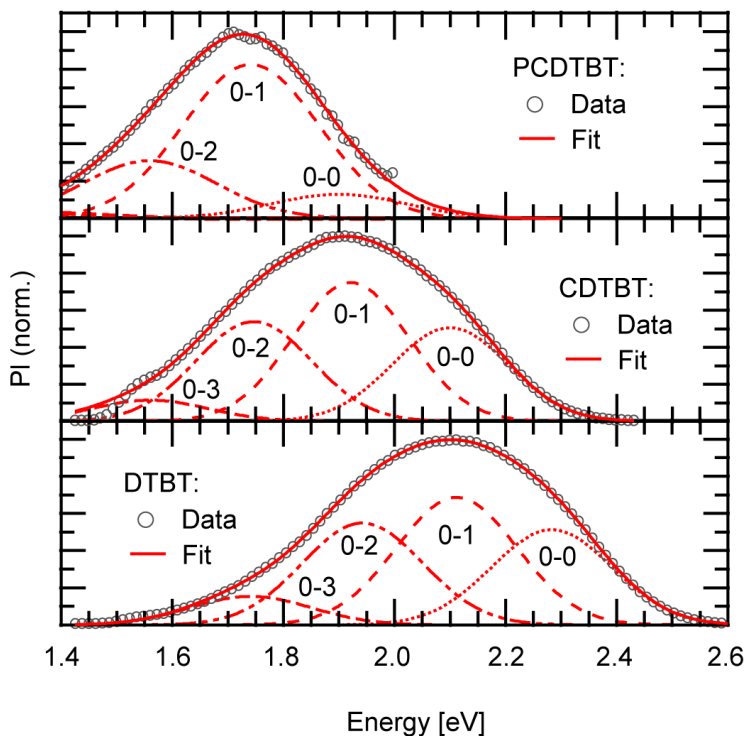


Figure 5.6: Assuming the presence of the same vibronic progression found for PCDTBT the PL spectra of the other benzothiadiazole containing molecules can be modeled again indicating the presence of one final emissive state in all of these molecules.

overlaps with the LEB of PCDTBT raises the question if the coupling mechanism between both excited electronic states is of Förster-type. An alternative scenario is the presence of a (partial) CT mechanism being responsible for the internal relaxation between both excited states.

In order to identify the nature of the coupling mechanism the influence of the solvent polarity on the peak position of the PL spectra, called solvatochromism, was analyzed. In general the geometry of the ground and first excited electronic state of a molecule are different (compare Section 2.2) and as a result also the polarities of both conformations differ, if the molecule exhibits a (partly) polar character. Thus changing the polarity of the solvent leads to a different interaction strength of the molecule with its surrounding, i.e. the polar solvent molecules. This results in an energetic shift of ground and first excited state and also a net shift of the energetic gap as a function of solvent polarity. If this energetic shift is to higher (bathochromic shift) or smaller wavelengths (hypsochromic shift) depends on the difference in dipole moment between the ground

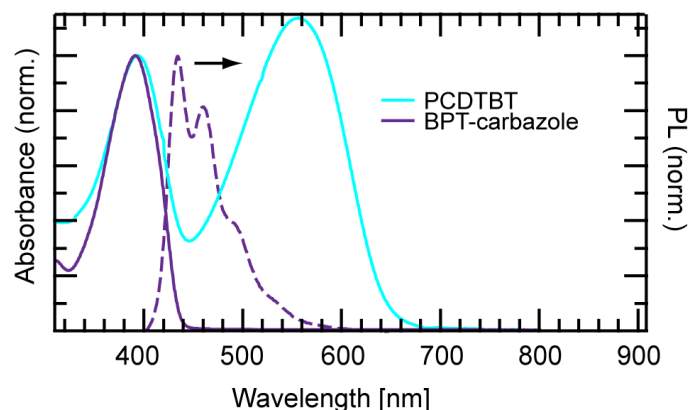


Figure 5.7: The HEB of PCDTBT can exactly be described by the absorption of the BPT-carbazole molecule indicating that excitation of the HEB leads to a neutral excitation located at this backbone segment. The spectral overlap of BPT-carbazole PL and the LEB of PCDTBT would in principle allow for a Förster-type energy transfer.

and excited state. In general, however the presence of solvatochromism indicates that the analyzed molecule exhibits a CT character.

Here we used three different solvents namely cyclohexane, chloroform and acetonitrile. These solvents exhibit an increasing polarity defined by the solvent polarity function as 0.10, 0.25 and 0.39, respectively. The polarity function is defined as $f(D) - 0.5 f(n^2)$ with $f(D) = (D - 1)/(2D + 1)$ and $f(n^2) = (n^2 - 1)/(2n^2 + 1)$, where n is the refractive index and D the dielectric constant of the solvent [175]. The position of the PL maxima of CDTBT (circles), monomer DTBT (squares) and BPT-carbazole (triangles) as a function of the solvent polarity is shown in Figure 5.8. The PL peak position for the comonomer CDTBT is clearly shifted to higher wavelengths with increasing solvent polarity strongly indicating the CT character of the LEB of CDTBT. This solvatochromic redshift can also be observed for the benzothiadiazole containing DTBT while it is completely absent for BPT-carbazole. Hence it can be concluded that the LEB of PCDTBT is of (partial) CT character which is supported by theoretical and experimental results for a donor-acceptor type molecule containing benzothiadiazole [176]. The presented results on BPT-carbazole strongly indicate that the HEB of PCDTBT has no significant CT character but represents a π - π^* transition which contradicts the work of Banerji et al. where both bands were associated with a CT mechanism [168]. Absorption within HEB leads to an excitation which is delocalized between two adjacent benzothiadiazole units and

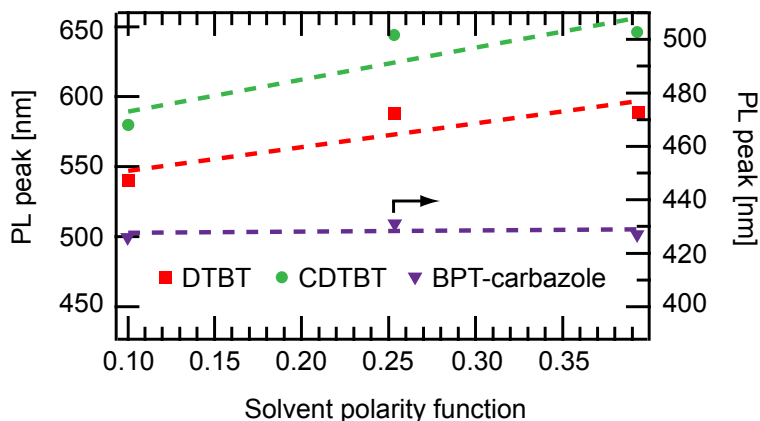


Figure 5.8: The observed solvatochromic shift of the PL peak position for the molecules containing benzothiadiazole strongly indicates that the LEB is of CT type.

thus inhibits a further delocalization of the π -electrons. This fact explains the quite small redshift of absorption observed upon polymerization of CDTBT.

The internal relaxation mechanism from the HEB to the LEB following photoexcitation of the HEB can therefore be considered as a (partial) CT transfer process from the BPT-carbazole backbone segment towards the adjacent (benzo)thiadiazole coupling the two excited electronic states. This coupling mechanism can be considered to be the dominant decay mechanism from the HEB as confirmed by a photoluminescence excitation (PLE) measurement. This measurement is carried out by measuring the PL of PCDTBT at a fixed wavelength while scanning the excitation wavelength in the range of the copolymer absorption. If a significant loss channel from the HEB was present, the high-energy peak of the PLE spectrum would be smaller than the corresponding peak of the absorption spectrum. The shape of the absorption spectrum of PCDTBT, however, can be reproduced by its PLE spectrum very well (Figure 5.9) indicating the efficient coupling between both electronic levels.

5.3 Exciton Dynamics in Copolymer Films

The decay dynamics of the PL spectrum of PCDTBT films excited at 397.5 nm exhibits a significant redshift as can be seen in Figure 5.10 (a). As already described for the steady state PL the transient spectra can be fitted assuming a dominant vibronic progression (compare Section 5.2). Evaluating the energetic position of the 0-1 and 0-2 peaks for various delay times (Figure 5.10 (b)) yields

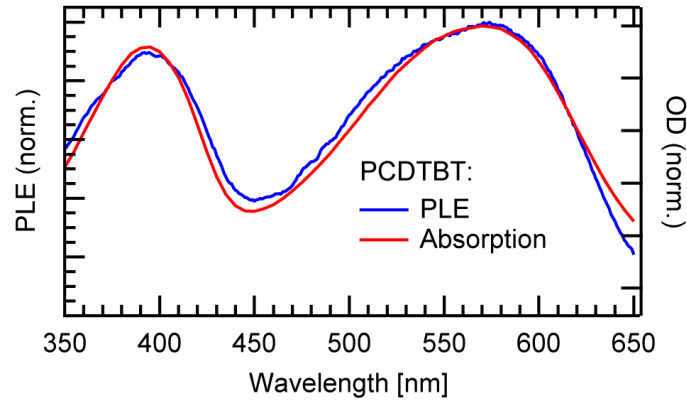


Figure 5.9: The PLE spectrum of PCDTBT reproduces its absorption spectrum very well which indicates that there is an efficient internal conversion within the copolymer.

a comparable redshift of both peaks of about 70-80 meV whose dynamics is strongest for the first 500 ps and completed within a 1 ns time window. This finding indicates that the overall redshift of the PL spectrum is not due to a redistribution of oscillator strength, i.e. change in the relative heights of the two peaks but a shift of the whole spectrum. The found shift is in good agreement with the one observed for a similar PCDTBT-type copolymer with longer side chains [177]. It can be interpreted as being the result of excited singlet excitons migrating to more ordered regions within the copolymer film during their lifetime.

In contrast, the time-resolved PL spectrum of P3HT at room temperature only exhibits a dynamic redshift of around 30 meV (Figure 5.11 (a)). The spectrum exhibits three dominant transitions (0-0 to 0-2) [178] with an energetic spacing of ≈ 160 meV which is again the typical region for the phenyl and thiophene ring breathing modes [12, 48]. Carrying out an analysis of various transient spectra according to the procedure described for PCDTBT, we find that this net energetic shift is also due to a gradual shift of the whole spectrum (Figure 5.11 (b)). However, the observed redshift of the P3HT PL is strongest for the first 200 ps and completed after ≈ 750 ps. Assuming the same mechanism responsible for the redshifts observed, i.e. the migration of singlet excitons to more ordered regions, the different spectral relaxation times found might be a result of the different film morphologies.

As shown in Figure 5.12 the XRD diffractogram of P3HT exhibits a clear peak around $2\theta = 5.4^\circ$. This peak can be attributed to highly ordered regions of polymer chains forming a lamella-like structure [179] resulting in a significant

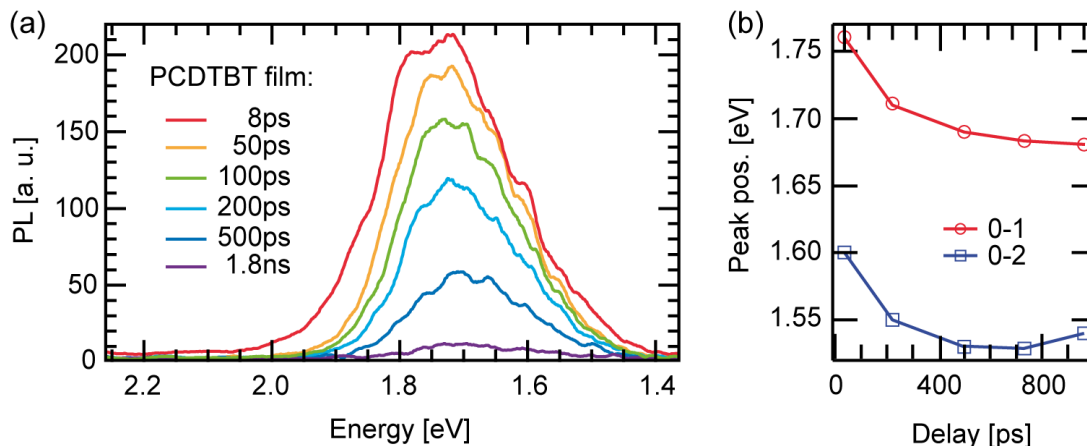


Figure 5.10: (a) The time-resolved PL spectrum of PCDTBT at room temperature exhibits a prominent redshift. (b) This redshift is due to a shift of the whole spectrum rather than a redistribution of oscillator strength between the involved transitions.

interchain or two-dimensional character of the optical and electronic properties of the polymer and its blends [62, 179, 180]. In contrast the XRD spectrum of PCDTBT shows only a very broad and weak feature around $2\theta = 6^\circ$ which indicates that the copolymer film only exhibits nanocrystalline regions embedded in a quite disordered surrounding [114, 181]. This observation is possibly related to material-specific parameters like the bended PCDTBT backbone [168, 181], a possible torsion of the thiadiazole group with respect to the backbone as observed for polyfluorene [182] and the fact that PCDTBT chains might tend to form bilayers due to the immiscibility of the different building blocks with each other as suggested by Ocko and coworkers [181]. As a consequence the “gradient of order” within PCDTBT — i.e. the energetic difference between ordered and disordered regions — might be larger compared to P3HT resulting in a larger net dynamic redshift of the copolymer PL spectrum.

To get a deeper insight into the exciton dynamics in PCDTBT films we analyzed the transients taken at the initial peak positions (8 ps) of the spectra at room temperature and 4.2 K (see Figure 5.13 (a)). The dynamics can be modeled assuming a biexponential decay and the results of the fits are found in Table 5.1. In agreement with the observed dynamic redshift, the time constants derived from fitting the transient at 1.61 eV are slightly larger than the values obtained from the 1.77 eV transient. The average values found for τ_1 and τ_2 are 98 ps and 425 ps, respectively. These values are in good agreement with the two large decay times found for PCDTBT by Banerji et al. [183]. They were both attributed to polymer backbone relaxation as well as exciton migration towards

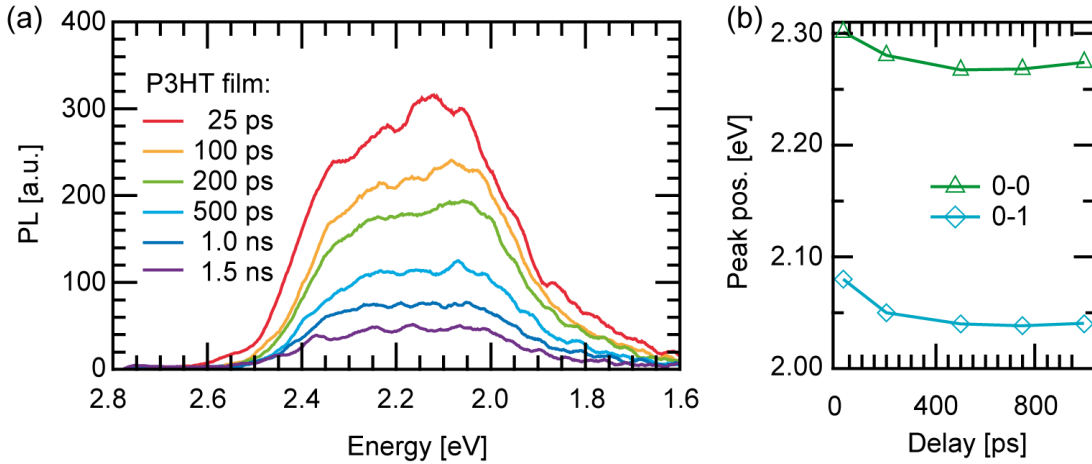


Figure 5.11: (a) P3HT exhibits a weaker dynamic redshift which might be due to the differences in morphology between the two polymers. (b) The shift is again due to a dynamic shift of the whole spectrum.

lower energetic sites. The residual PL signal for maximum delay indicates that a third \approx ns component is present but does not significantly contribute to the decay within the measured time-window. Reducing the temperature of the copolymer film to 4.2 K slows down the PL decay and the effective time constants observed are $\tau_1 = 350$ ps and $\tau_2 = 1.1$ ns while no signature of the 100 ps component can be identified. This indicates that the two dominant picosecond channels observed in the room temperature measurement are dominated by a single but different mechanism which is in contrast to the results presented by Banerji and coworkers. Furthermore the absence of the 100 ps component points towards a thermally activated, diffusion assisted decay mechanism as origin of this channel. Interestingly, when reducing the excitation power by two orders of magnitude (Figure 5.13 (b)), i.e. reducing the number of created excitons, the 100 ps channel also vanishes at room temperature and the time constants found are $\tau_1 = 280$ ps and $\tau_2 = 1.2$ ns, respectively. These values are in good agreement with the decay times found for the high excitation power measurement at 4.2 K. These results imply that the 100 ps channel might be due to bimolecular recombination processes like exciton-exciton or exciton-polaron quenching instead of polymer backbone relaxation. Both mechanisms are expected to become relevant for excitation densities of $\geq 10^{18}$ cm $^{-3}$ [184, 185, 186]. However, even the high excitation power of 5 mW results in an excitation density that is smaller than the mentioned threshold by three orders of magnitude and especially the interaction of excitons with charges in neat copolymer films is expected to be of minor importance. Thus it can be speculated whether or not the 100 ps channel depicts

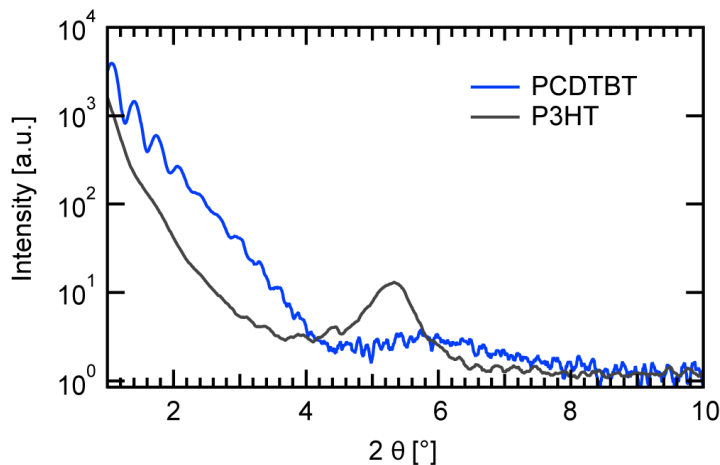


Figure 5.12: While the P3HT film clearly shows ordered, lamella-like regions as indicated by the peak in the XRD diffractogram, PCDTBT resembles a rather disordered polymeric system with only small crystalline regions in the nanometer regime.

a bimolecular recombination process or phonon-assisted quenching due to the polymer backbone relaxation. Regardless the actual nature of the decay channel it can be considered to be an extrinsic pump-induced decay mechanism. On the contrary the two time constants found for the low excitation power measurements resemble intrinsic relaxation pathways. τ_1 is of the order of the inhomogeneity induced quenching channel that was identified for rubrene (compare Chapter 4) while the second time constant (τ_2) is of the order of typical singlet exciton lifetimes observed in organic systems (see Chapter 2). The fact that it matches the timescale of the observed spectral redshift found for PCDTBT strengthens the aforementioned statement.

For temperatures ≤ 150 K the picosecond component vanishes indicating that this channel is related to a thermally activated decay mechanism like diffusion assisted quenching at inhomogeneities such as defects, impurities or interfaces between disordered and ordered regions. The absence of τ_1 at low temperatures can then be explained by hindered exciton migration for example by the deactivation of torsional motions of the polymer backbones trapping excitons at certain chain segments. As a result the probability of excitons being quenching at defects and/or inhomogeneities within the film is highly reduced. In this case it can be speculated that long-lived excitonic states at room temperature (τ_2) resemble rather immobile excitons that are trapped or located within ordered regions of the copolymer.

For comparison the transients of the P3HT films excited with $30 \mu\text{W}$ and

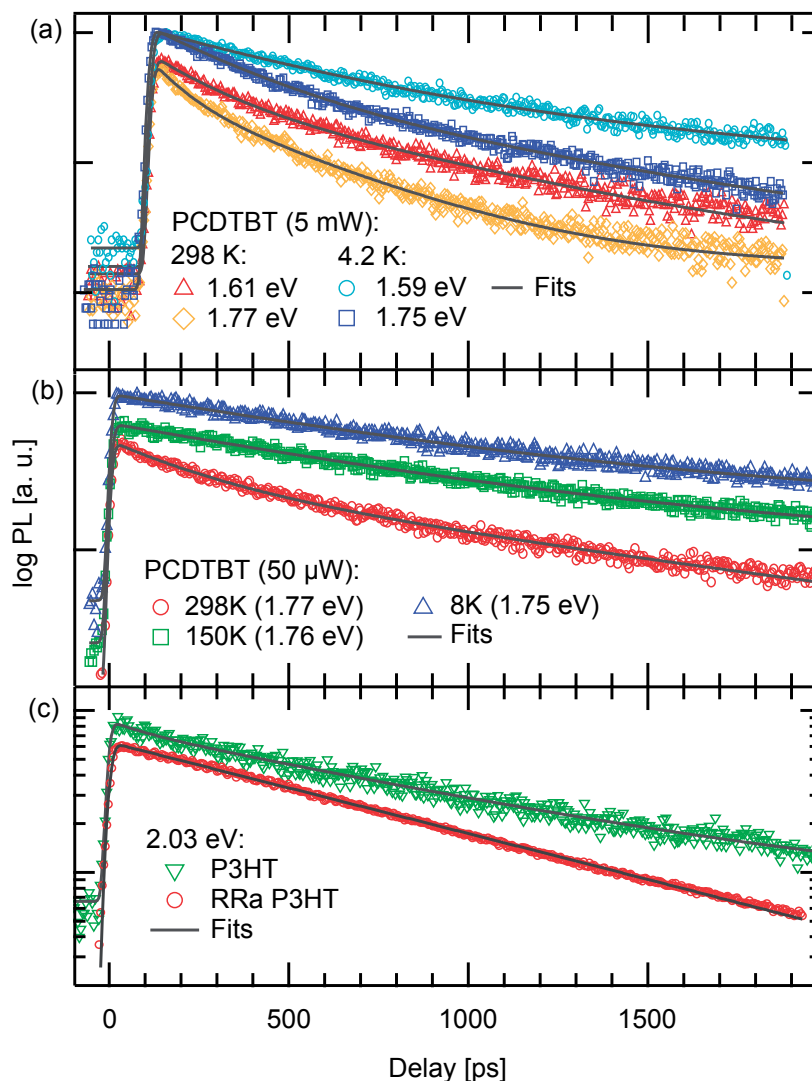


Figure 5.13: Transient behavior of the PCDTBT and P3HT PL taken at specific energies. For the sake of clarity the transients are vertically shifted with respect to each other. PCDTBT transients for different temperatures taken at two different energies (a) as well as for reduced excitation power (b). For comparison a P3HT transient is shown together with the PCDTBT transient measured with comparable excitation power (c).

measured at room temperature were also analyzed (see Figure 5.13 (c)). Again the decay behavior can be fitted assuming a biexponential decay. The two time constants of around 96 and 730 ps, respectively are smaller than the ones observed

for PCDTBT, which is consistent with the slightly faster redshift observed for P3HT. As τ_2 is of the order of the aforementioned spectral redshift of P3HT, it can be identified with the effective singlet exciton lifetime. Considering the low excitation power used, the lower picosecond channel τ_1 is not expected to be a pump-induced quenching process but of intrinsic nature. It might also be due to quenching at inhomogeneities within the film. Compared to the PCDTBT film, the relative contribution of the aforementioned fast decay channel to the overall decay dynamics is much smaller for P3HT. This observation can be interpreted as the P3HT film exhibiting a higher degree of order compared to PCDTBT thin films. Interestingly, the PL transient of a regiorandom P3HT (rra P3HT) film is found to decay monoexponentially with a time constant comparable to the τ_2 of the ordered P3HT film. Compared to the “normal” regioregular P3HT film the regiorandom film is rather disordered and is not expected to exhibit a significant amount of ordered lamella-like regions due to the non-planar polymer backbone [180, 187]. Since it can be speculated that τ_1 originates from exciton quenching via dissociation at interfaces between ordered and disordered regions as high exciton dissociation yields within lamellae structures [188] and in particular the dissociation at the interfaces [189] has been reported in literature. The results of the fits are summarized in Table 5.1 while Figure 5.14 schematically illustrates the model for exciton migration in PCDTBT thin films derived from the analysis of the time-resolved PL data.

Sample	T [K]	E [eV]	A_1/A_2	τ_1 [ps]	τ_2 [ps]
PCDTBT (5mW)	298	1.61	0.38	104	480
		1.77	0.53	92	368
	4.2	1.59	1.47	420	1300
		1.75	1.93	287	910
PCDTBT (50 μ W)	298	1.77	0.80	280	1190
	150	1.76	—	—	906
	8	1.75	—	—	948
P3HT	298	2.03	0.13	96	730
rra P3HT	298	2.03	—	—	614

Table 5.1: Summary of the results from fitting the transients shown in Figure 5.13 assuming a biexponential decay.

Compared to the exciton dynamics analyzed for the different rubrene morphologies presented in Chapter 4, the PL decay of the PCDTBT film is qualitatively comparable to the results for the nanocrystalline film. This might be due to the fact that both morphologies exhibit a similar “gradient of order” because they both exhibit nanocrystalline regions embedded in an amorphous surrounding. The actual morphology, however and in particular the size of the crystalline

regions is expected to be different for the PCDTBT film and the nanocrystalline rubrene film. In contrast, the exciton dynamics measured for the P3HT films are in principle more similar to the decay dynamics of the amorphous rubrene film. This similarity, however, can again be seen as a consequence of the homogeneous character of both film systems and is not expected to result from comparable morphologies of the respective thin films.

Since only emission from the LEB of PCDTBT can be observed for the time-resolved PL measurements, the internal relaxation mechanism between HEB and LEB is expected to be faster than the temporal resolution of the setup, i.e. < 8 ps. This observation is in agreement with the results by Banerji et al. indicating a sub-picosecond relaxation time [183].

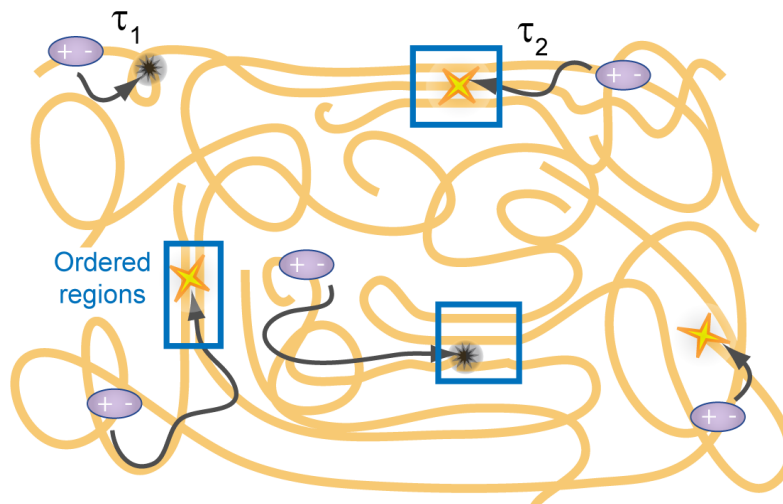


Figure 5.14: Scheme illustrating the singlet exciton dynamics within the PCDTBT film as analyzed in this section.

5.4 Relaxation Dynamics in Copolymer:Fullerene Blends

The PL signal collected from a 1:1 blend of PCDTBT with PC₇₀BM is strongly quenched due to the dissociation of singlet excitons generated in the PCDTBT phase at the donor-acceptor interface by electron transfer towards the fullerene (Figure 5.15 (a)). Since PC₇₀BM has significant absorption around 400 nm the excitation of the blend at 397.5 nm leads to excitation of both donor and acceptor molecules resulting in a blend PL signal which is a superposition of both contributions. Hence the PL spectrum of a neat fullerene film was measured separately

for being able to estimate the relative contributions of donor and acceptor PL to the blend spectrum. We find that at 50 ps the PL spectrum of the blend can be completely described by the fullerene PL while the initial transient spectrum clearly shows copolymer contribution. This indicates a complete quenching of PCDTBT PL within the first 50 ps after excitation of the blend film. The exact time constant for the PL quenching cannot be determined within the temporal resolution of the setup.

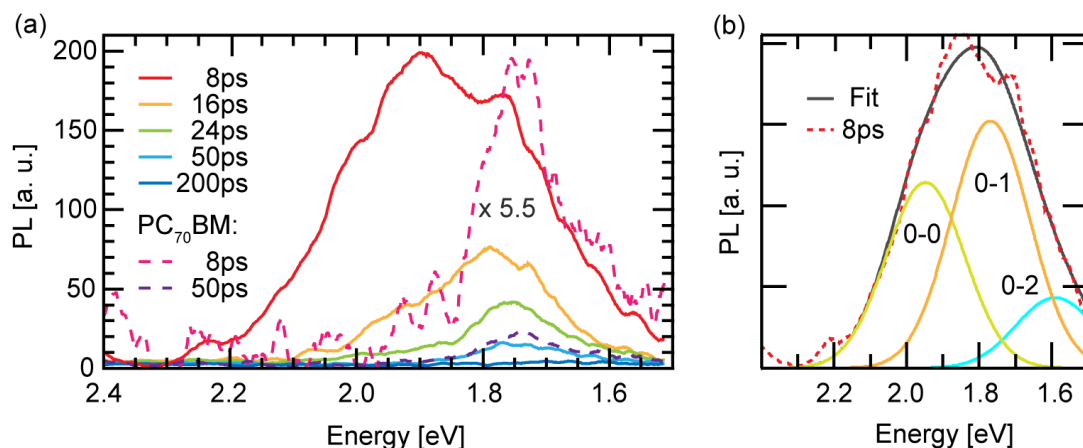


Figure 5.15: (a) Transient spectra of 1:1 blend of PCDTBT with PC₇₀BM. While the initial spectrum shows clear copolymer contribution, the spectra for larger delays can be identified with fullerene emission (dashed lines). (b) the initial blueshift of the blend spectrum can be explained with an increased relative contribution of the 0-0 transition possibly due to a reduced self-absorption of the blend film.

Interestingly, the blend PL spectrum is initially blueshifted compared to the neat PCDTBT film spectrum. As shown in Figure 5.15 (b) this shift can be explained by a dominant contribution of the 0-0 transition to the initial spectrum resulting from a reduced self-absorption of the copolymer PL in the blend film due to the reduced absorption of PC₇₀BM compared to PCDTBT in this spectral range. In addition the increased disorder in the intermixed donor-acceptor regions might cause an increase of the relative contribution of the 0-0 transition. For the blend spectrum no dynamic redshift can be observed which is possibly due to the highly reduced effective exciton lifetime in the blend film due to an efficient separation at the interfaces. It also indicates that the majority of singlet excitons created in the donor phase reaches an interface without traveling large distances.

Although the fullerene content of the measured 1:1 blend is much lower than

the one for an optimized photovoltaic blend (D:A = 1:4) [109, 110], the copolymer PL is efficiently quenched. As shown in the top graph of Figure 5.16 the transient taken at 2.0 eV, which is the spectral region dominated by copolymer emission, decays within the temporal resolution of 8 ps. This might be due to the fact that

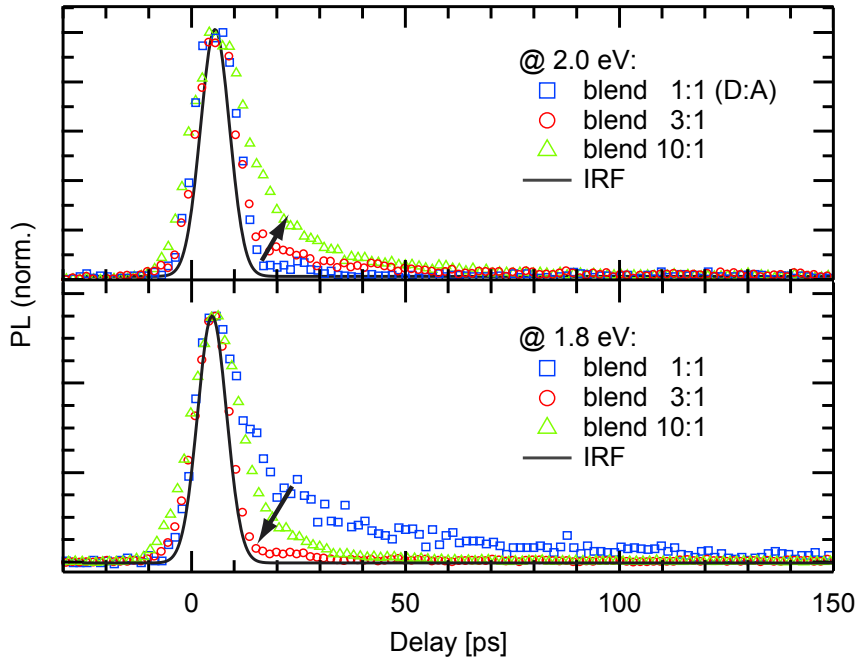


Figure 5.16: Blend transients taken at 2.0 eV (top) and 1.8 eV (bottom) respectively for blends exhibiting a reduced fullerene content (1:1 to 10:1). Here IRF denotes the instrument response function, i.e. the temporal resolution of the measurements.

PCDTBT:fullerene blends form an intercalating system [114, 190], where a ratio of around 1:1 is indeed sufficient for an efficient exciton splitting and subsequent charge generation. Additional fullerene content is required for the formation of pure acceptor phases that are crucial for charge transport. As mentioned before, the residual PL observed from the 1:1 blend for delay times > 8 ps can be assumed to originate from acceptor emission indicated by the slower decay of the transient taken at 1.8 eV (top graph of Figure 5.16). For this transient a second time constant of around 55 ps can be identified indicating that migration assisted exciton splitting might contribute to the acceptor PL. Considering the intercalation this means that at a ratio of 1:1 the fullerenes might already start to form domains. Reducing the fullerene content (3:1 blend) results in a more efficient quenching of acceptor PL which is confirmed by the fact that the 1.8

eV transient now also decays within the temporal resolution. Thus, from a photophysical point of view, the ideal blend ratio for PCDTBT:PC₇₀BM films is close to 3:1 as excitons generated in both donor and acceptor phase are efficiently quenched at the D-A interfaces. Further reducing the fullerene content (10:1) enhances the migration assisted character of the quenching of excitons created in the donor phase and both transients clearly exhibit a second time constant of around 55 ps as the whole spectrum now is dominated by copolymer emission.

In the blend system excitation of the copolymer into the HEB can in principle lead to the direct transfer of excitation energy by means of an electron or energy transfer towards the fullerene acceptor. This process can in principle act as an effective decay route competing with the internal conversion to the LEB followed by the subsequent radiative relaxation to the ground state. The transfer of excitation energy towards a fullerene acceptor has been observed for the copolymers F8BT and IFBT blended with PC₆₀BM following photoexcitation of the donors [85, 86]. However, the aforementioned copolymers were only excited via LEB absorption and the energy transfer towards the fullerene acceptor was followed by intersystem crossing and triplet generation within the acceptor resulting in relatively poor device efficiencies. In order to check for the existence of an alternative decay channel from the HEB of PCDTBT when used in a photovoltaic blend system, a PLE measurement of the 1:1 blend film was carried out and compared to the PLE spectrum of a neat copolymer film. As shown in Figure 5.17, both PLE spectra are almost identical, strongly indicating that there is no transfer of excitation energy from the HEB of PCDTBT towards PC₇₀BM. Therefore, even for excitons created close to the donor-acceptor interface, which are expected to have a significant contribution to the blend PL of the intercalated system [191], the direct electron transfer from the HEB towards the fullerene represents no significant alternative decay channel. Instead the internal conversion in form of a partial CT on the copolymer backbone is expected to precede the electron transfer process towards the PC₇₀BM.

It can be argued that the increased delocalization of the exciton on the copolymer backbone due to its CT character support the final separation of these excitons into charges at the D-A interface of the photovoltaic blend. The presence of this correlation is indicated by the dependency of device efficiency on the copolymer intrachain dipole moment observed for copolymer PTB7 [192, 193]. This would also explain why in the case of PCDTBT no lamella-like domains, which are expected to assist the exciton dissociation process in P3HT [188, 189], are necessary to yield a very high light-to-charge conversion efficiency.

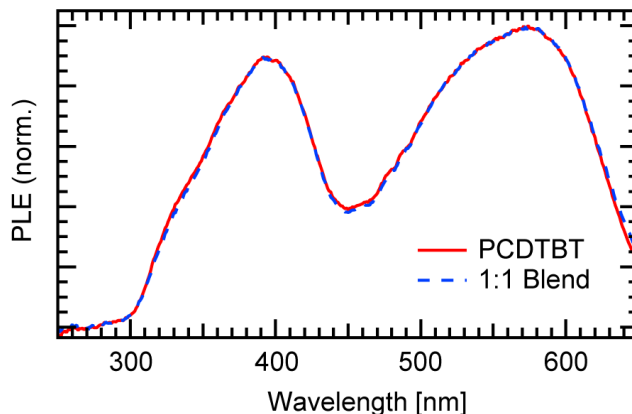


Figure 5.17: The PLE spectra of PCDTBT and the 1:1 blend are almost identical indicating that there is no significant decay channel from the HEB of PCDTBT competing with the internal relaxation towards the LEB.

5.5 Summary

This chapter presents the results of a detailed optical characterization of the donor-acceptor type copolymer PCDTBT, its repeat unit CDTBT, its building blocks carbazole and DTBT as well as the newly synthesized BPT carbazole. The latter molecule represents a PCDTBT backbone segment without the thia-diazole groups. By applying steady state absorption and PL as well as solvatochromic shift measurements it is possible to identify the functional subunits of PCDTBT giving rise to the two distinct absorption bands and decipher the nature of the internal coupling mechanism between both excited electronic levels. These functional groups differ from the building blocks used for the synthesis of the copolymer leading to a slightly different "functional repeat unit". As shown in Figure 5.18 the HEB ($|2\rangle$) of PCDTBT stems from the absorption of the 2,7-di(thien-2-yl)carbazole group. The LEB ($|1\rangle$) in contrast can be assigned to the intra-chain charge transfer state formed by the latter and the adjacent benzothiadiazole units. An energy level representation of the two prominent excited electronic states as well as the relevant relaxation pathways identified in this chapter are shown in Figure 5.19. Excitation via the HEB is followed by an internal conversion step in the form of an ultrafast partial CT towards the benzothiadiazole group followed by relaxation to the ground state. The radiative lifetime of singlet excitons in PCDTBT is found to be in the order of 1 ns. The PL decay dynamics are dominated by a redshift of about 70-80 meV which can be explained by exciton migration to lower energy sites, i.e. to more ordered regions. This shift is significantly larger than for P3HT indicating a

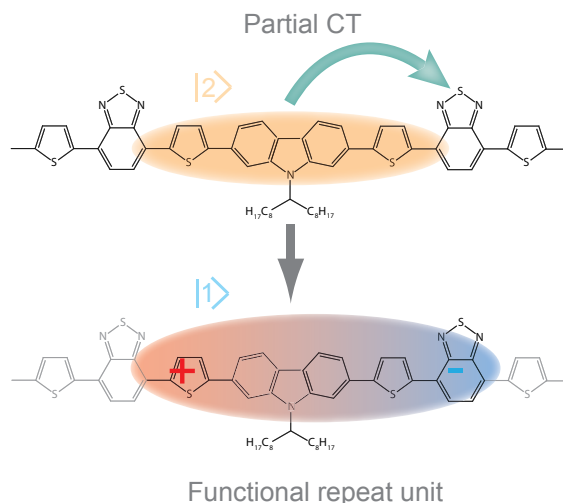


Figure 5.18: Scheme illustrating the nature of the two prominent excited electronic states of PCDTBT and the coupling mechanism between them.

reduced crystallinity of the copolymer film or in other words a sample morphology exhibiting a larger gradient between disordered and ordered regions. It can be assumed that the copolymer film is dominated by large disordered regions and only exhibits nanometer-sized ordered domains. An additional thermally activated decay channel with a time constant of ≈ 280 ps can be interpreted as resulting from quenching of singlet excitons at inhomogeneities for example impurities, defects or interfaces between ordered and disordered regions during migration. In blend films with PC₇₀BM the copolymer PL is efficiently quenched within the first 50 ps after excitation due to the electron transfer towards the fullerene. No indication for a direct transfer of excitation energy from the HEB of PCDTBT to PC₇₀BM was identified and since the internal relaxation within PCDTBT is expected to precede the electron transfer process towards the acceptor molecules. This finding indicates that the effective coupling between the functional subgroups of the copolymer governs the photovoltaic performance within these new donor-acceptor-based blend systems. It can be speculated that this intra-chain pre-separation of singlet excitons facilitates the generation of charge carriers within the blend resulting in the high conversion efficiency reported in literature. From a more macroscopic point of view, the transfer of excitation energy within the copolymer guarantees for the efficient operation of PCDTBT devices that benefit from the optimized HOMO and LUMO levels of the copolymer.

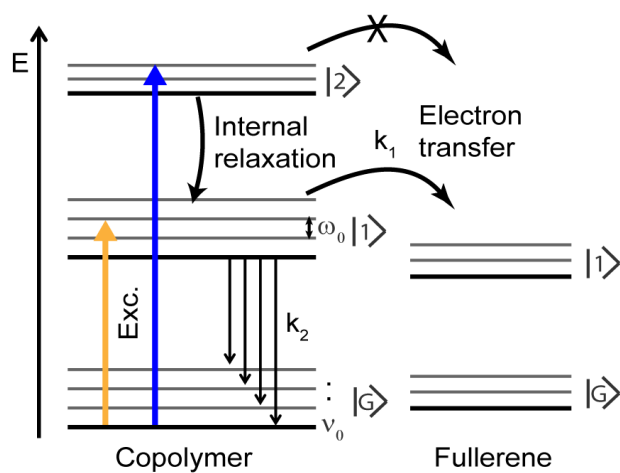
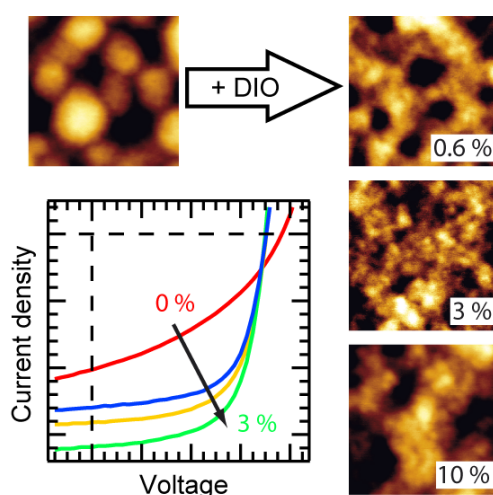


Figure 5.19: Energy level scheme of the relaxation pathways present in a photovoltaic blend of PCDTBT with fullerene PC₇₀BM following photoexcitation.

The Influence of Processing Additive on the Charge Generation in Copolymer Solar Cells



6.1 Copolymer Blends and the Influence of Additives

A second key aspect for improving the efficiency of organic solar cells besides the previously discussed synthesis of new donor materials is the optimization of the morphology of the active layer. The major issue concerning this task arises from the general discrepancy between the ideal thickness of the layer for absorption of solar irradiation of around 100 nm and reported singlet exciton diffusion length of ≤ 10 nm (see Chapter 2). Nevertheless the ideal active layer should facilitate both: efficient charge generation and transport. To cope with this challenge and promote exciton dissociation — i.e. charge photogeneration — the bulk heterojunction approach was introduced [194] and has proven to be one of the most successful designs for organic photovoltaics so far. However, this

type of solar cell comes with the disadvantage of potentially higher recombination losses and a lack of control of the actual morphology.

In order to improve the device efficiencies of P3HT-fullerene blends usually a post production annealing step is employed which promotes phase separation and improves the extraction of photogenerated charges while at the same time reduces trap regions by isolated donor and/or acceptor domains [195, 196, 197]. For solar cells based on new copolymer donors this annealing step has been replaced by using a solvent additive during thin film production. The method has the general advantage that no additional fabrication step is needed. The effect, however is similar: The degree of intermixing between donor and acceptor phases within the active layer employing the additive is significantly altered compared to the sample without additive. These morphological changes result in a substantial increase of device efficiencies [118, 198, 199]. For example adding 3 % of diiodooctane (DIO) increases the efficiency of PTB7:PC₇₀BM solar cells by a factor of almost two [119]. The processing additives are expected to increase the solubility of the fullerene molecules thus increasing their ability to move within the blend film during processing. If the intermixing of the blend system is enhanced or reduced upon employing an additive depends on the copolymer used as indicated in Figure 6.1. While for blends based on copolymer PCPDTBT the processing additive results in a demixing and the formation of pure fullerene domains [199] the effect for PTB7-based blends is the opposite. Here the intermixing is improved and the size of the fullerene clusters is reduced [198]. While existing publications focus on the comparison between the morphologies of the optimized blend and the untreated one, there exist only few detailed studies about the correlation between additive content, morphology and device performance. In particular the different mechanisms affecting the efficiency of the solar cell and their interplay that leads to a distinct performance maximum for a certain additive content are unknown.

In this chapter a detailed study of the influence of processing additive DIO on the optical, electrical and morphological properties of blend films comprised of copolymer PBDTTT-C and PC₇₀BM is presented. As the molecular structure of PBDTTT-C is very similar to PTB7 (see Section 6.3) a significant influence of processing additives on the blend morphology is also expected for this copolymer:fullerene system. As mentioned in Chapter 3, PBDTTT-C is an example of the promising family of benzodithiophene donor materials and thus an ideal copolymer for the study. By comparing the results of picosecond time-resolved PL and TA experiments on the one hand and current-voltage (IV) and AFM measurements on the other hand, we are able to develop a detailed picture of the morphological changes of PBDTTT-C:PC₇₀BM blend films as a function of the additive content. These changes directly affect the optical properties of the blends like PL emission and transient absorption as well as the device parameters

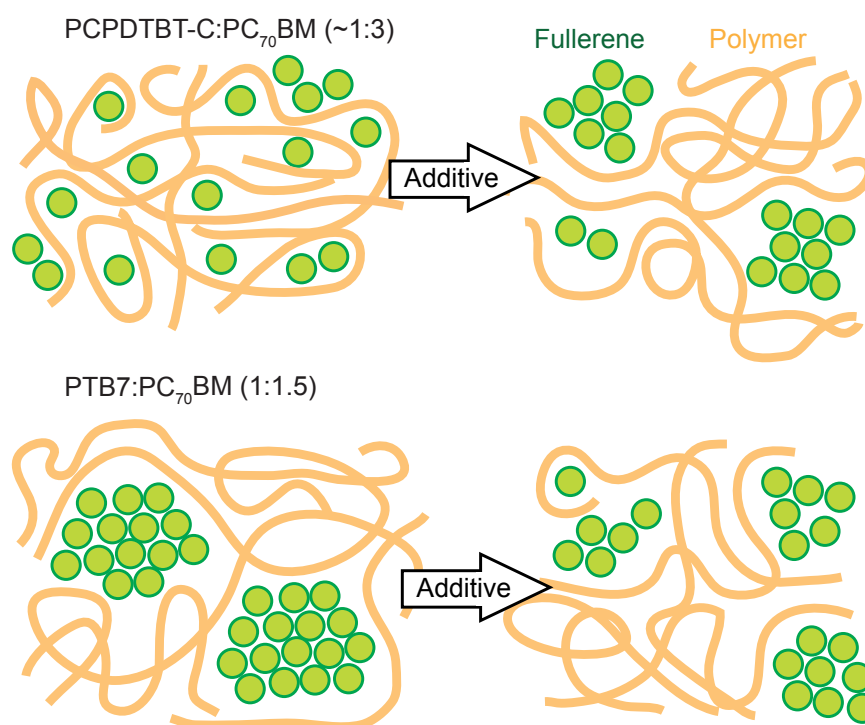


Figure 6.1: Schemes illustrating the influence of a processing additive on the blend morphologies of two different types of copolymer:fullerene systems. While for devices based on copolymer PCPDTBT the additive promotes the formation of pure fullerene phases it reduces the acceptor domain size in the case of PTB7-based devices. The number in brackets denotes the optimized ratios for the respective blends.

of the solar cell as we will see in the following sections.

6.2 Solar Cell Performance

The IV curves of solar cells fabricated from PBDTTT-C:PC₇₀BM blends at a ratio of 1:1.5 with varying DIO content are shown in Figure 6.2. The characteristic photovoltaic parameters can be found in Table 6.1 (measurements and data evaluation presented in this section done by Andreas Zusan). It is obvious that increasing the additive content towards 3 % leads to a subsequent increase of the device efficiency (PCE) from 2.6 % up to 6.9 %. This increase by a factor of more than two mainly results from an increase in short circuit current density j_{SC} (factor 1.6). The significantly larger j_{SC} easily compensates for a slight de-

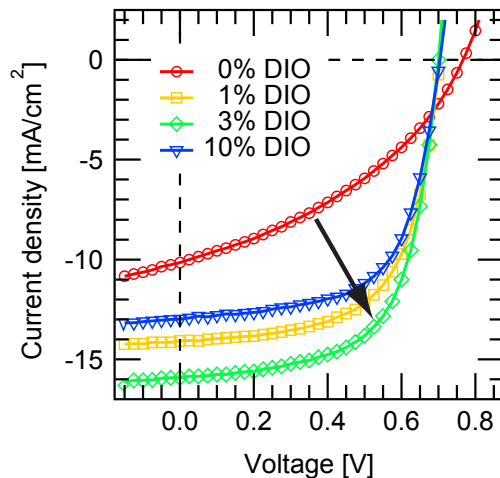


Figure 6.2: IV curves measured under AM 1.5 G conditions for solar cell devices fabricated using an increasing content of the processing additive DIO. The corresponding parameters are summarized in Table 6.1 (Data measured by Anreas Zusan).

crease in open circuit voltage V_{OC} . The increased device performance is reflected by an increase of the fill factor (FF) by a factor of 1.74. Interestingly, the most significant enhancement of solar cell performance can already be observed for the 0.6 % and 1 % DIO blends while further improvements of fill factor and PCE for the 3 % DIO blend are quite small. The described trends are reversed when increasing the DIO content to 10 %. Although the fill factor is still high, the device efficiency drops by 23 % to 5.3 % which is basically due to a comparable reduction in j_{SC} . Thus the cells fabricated by adding 3 % of DIO exhibit the maximum efficiency of around 7 % which is mainly due to a maximum in j_{SC} observed for these devices. The reasons for the described dependence of device efficiency on the DIO content and in particular for the maximum at 3 % percent will be disentangled in the following.

6.3 Optical Characterization

This section summarizes the fundamental optical properties of the analyzed PBDTTT-C:PC₇₀BM blend system, i.e. the steady state absorption and emission spectra of both materials as well as the photoinduced absorption (PIA) spectrum of the blend and a neat PBDTTT-C film. For comparison also the corresponding spectra of copolymer PTB7 and PTB7:PC₇₀BM blends are presented. This copolymer is almost identical to PBDTTT-C as can be seen in Figure 6.3 as

Blend	V_{OC} [mV]	j_{SC} [mA cm^{-2}]	FF [%]	PCE [%]
0 % DIO	773	9.6	35.4	2.6
0.6 % DIO	731	12.8	56.9	5.3
1 % DIO	715	13.7	60.8	6.0
3 % DIO	719	15.5	61.7	6.9
10 % DIO	724	11.9	61.1	5.3

Table 6.1: Solar cell parameters measured under AM 1.5 G conditions for devices fabricated with varying DIO content (Data evaluation by Andreas Zusan).

it is also based on thieno[3,4-b]thiophene and benzodithiophene moieties. The

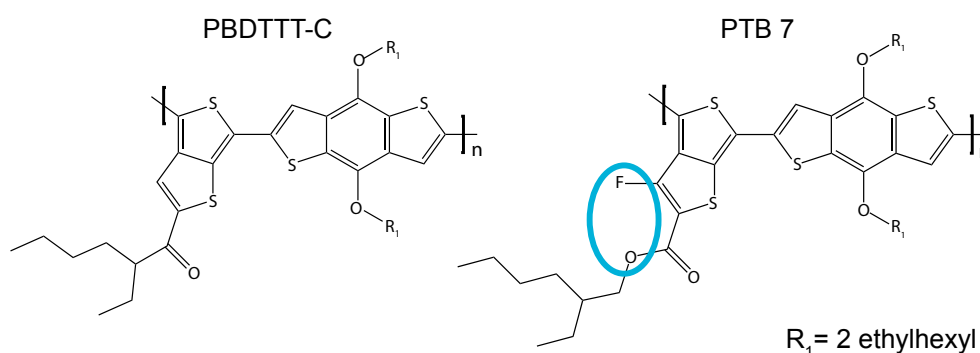


Figure 6.3: Molecular structures of copolymers PBDTTT-C (left) and PTB7 (right). The latter molecule is modified with respect to PBDTTT-C in the way that the thienothiophene unit is modified by an additional oxygen and fluorine atom (blue circle).

only difference is that the thienothiophene unit is slightly modified by an additional fluorine atom and a second oxygen atom is incorporated into the side chain attached to the thienothiophene (circle in Figure 6.3). This modification is expected to increase the intrachain dipole moment of the copolymer repeat group as the electron withdrawing character of the thienothiophene is increased which was found to have a positive effect on the device performance [192, 193]. Concerning the fundamental optical properties and the relaxation dynamics both copolymers are expected to behave very similar as the different dipole moments should mainly affect the initial internal relaxation within the copolymer (compare Chapter 5). Therefore the results derived for PBDTTT-C should in principle be applicable to PTB7-blends and vice versa.

While the absorption spectra of both copolymers slightly differ in shape, the PL spectra are almost identical but energetically shifted with respect to

each other (see Figure 6.4). This might indicate that the modification of the thienothiophene group has a much stronger effect on the energetics of the first excited electronic states than on the ground state. The absorption as well as the emission spectra of PBDTTT-C are significantly overlapping with the respective fullerene spectra. Since excitation of the PBDTTT-C:PC₇₀BM blend in the

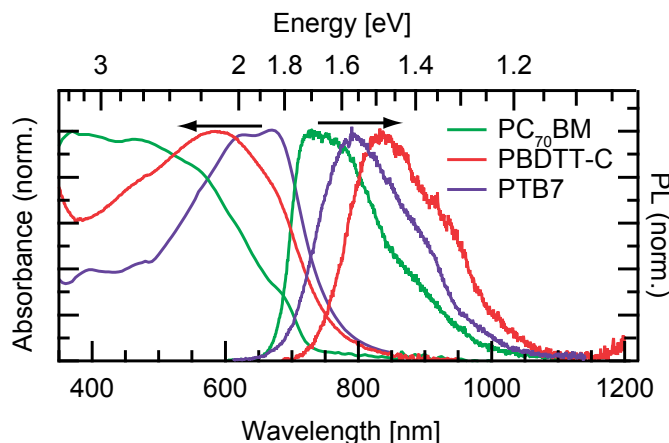


Figure 6.4: Absorbance and PL spectra of the copolymers PBDTTT-C and PTB7 as well as of PC₇₀BM. While the absorbance of both donor materials slightly differs, the PL is very similar in shape but shifted with respect to each other. In general the PL spectra of both donors and the fullerene are overlapping.

visible spectral range will create singlet excitons in both — donor and acceptor phase. The residual PL emitted from the blend can therefore be assumed to be a superposition of donor and acceptor emission.

Both copolymers yield very similar PIA spectra that exhibit one prominent broad and asymmetric absorption band (**1**) centered around 0.90 eV (Figure 6.5 top graph). This observation indicates comparable energetics of the photogenerated intermediate states in both copolymers which implies the presence of the same types of photoexcited species for both copolymers. The different shapes of the bleach (**B**) and stimulated emission (**SE**) bands, respectively (below 1.50 eV) are due to the differences between the absorption and PL spectra of both copolymers. Adding the PC₇₀BM acceptor (ratio PBDTTT-C:PC₇₀BM of 1:1.5) increases the overall intensity of the absorption and bleach/stimulated emission bands in the energy range ≥ 0.6 eV while the relative spectral shapes are comparable to the ones of the neat copolymer films (see Figure 6.5 middle graph). This indicates that the presence of the acceptor increases the number of excited transient species but does not introduce a significant, i.e. detectable, amount of new intermediate states to this part of the blend PIA spectra. Only in the

low-energy part an additional absorption band around 0.30 eV (**2**) can be identified. This second absorption band, however, could in principle also be present in the neat copolymer PIA spectra but might not be detectable because of the low signal to noise ratio in this spectral region. Compared to the PIA spectrum of

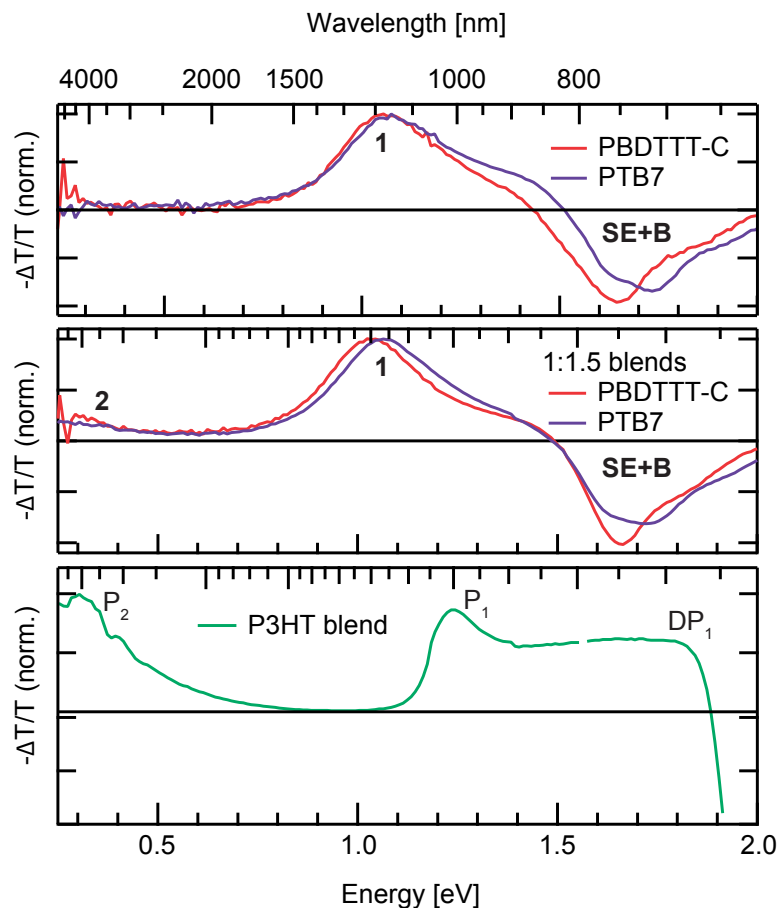


Figure 6.5: PIA spectra of the neat copolymer films (top graph) and blend films with $PC_{70}BM$ (middle graph). The relative spectral shapes of all spectra are found to be very similar. For comparison also the PIA spectrum of a P3HT-based blend is shown (P3HT spectrum measured by Julien Gorenflot).

a P3HT:fullerene blend film (Figure 6.5 bottom graph) the overall shape of the absorptive part of the copolymer-based blend spectra appears to be less complex. A possible explanation is that PBDTTT-C- and PTB7-based blends do not exhibit highly ordered lamella-like donor regions like P3HT (see Chapter 5) that give rise to the transient signatures of delocalized polarons and interchain excitons [62]. Due to the asymmetric shape of absorption band **1** however the existence of two spectrally overlapping absorption peaks representing two different

photoexcited transient species is highly probable.

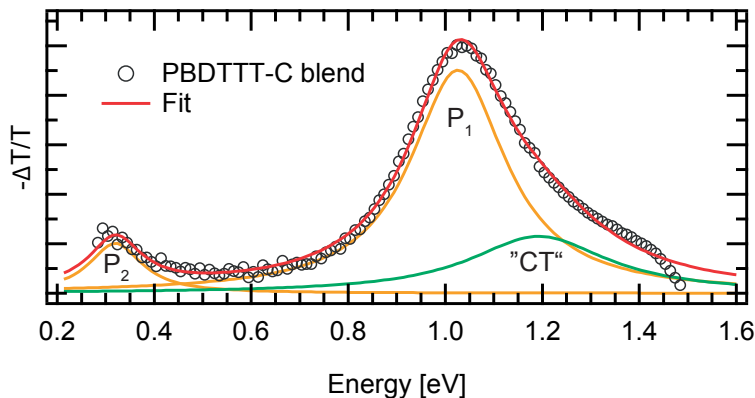


Figure 6.6: Qualitative fit of the PBDTTT-C blend PIA spectrum. The asymmetric shape of the main absorption band around 1.0 eV indicates the presence of two overlapping absorption peaks. $P_{1,2}$ denotes the absorption peaks attributed to absorption by hole polarons while “CT” stands for absorption by intrachain CT states.

As indicated in Figure 6.6 a fit of the PBDTTT-C:PC₇₀BM blend spectrum yields two peaks for the dominant absorption band **1**— one dominant contribution centered at around 1.03 eV and a second smaller peak at around 1.20 eV. The actual shape of the latter peak, however, might be slightly different from the fit as the high-energy edge of absorption band **1** might be affected by the spectrally overlapping bleach/stimulated emission band. This circumstance would also explain the deviation of the fit from the measured PIA spectrum in this region.

The main PIA band at 1.03 eV is in the typical energy range for polaron absorption observed for copolymers and copolymer:fullerene blends [193, 73]. A broad transient absorption band centered at around 1.07 eV found for a neat PTB7 film has been assigned to absorption of hole polarons generated in the copolymer film [192]. Assuming that this peak results from absorption of holes (P_1) a second absorption peak (P_2) is expected at smaller energies according to the bandgap state model (see Section 3.4.1). This assumption is consistent with the observation of the low-energy absorption band located at around 0.30 eV and indeed absorption from hole polarons can be observed in this energy regime (see lower graph in Figure 6.5).

A possible explanation for the additional absorption peak at 1.20 eV could be the absorption of a delocalized excitonic species according to observations for other polymeric systems [62, 200]. Possible candidates for such a delocal-

ized excitonic state are in general CT excitons generated at the D-A interface or an intrachain quasi CT exciton considering the D-A character of the copolymer repeat units (see Chapter 5). The fact that the PIA spectrum of the neat PBDTTT-C film also exhibits the 1.20 eV peak points towards the latter interpretation. This assignment of the 1.20 eV peak is also in agreement with TA measurements on PTB7 films where an absorption band centered at around 1.30 eV has been assigned to a pseudo intrachain CT state [192]. According to the bandgap state model there should again be a second absorption band arising from such a delocalized excitonic state at energies below 0.30 eV. The presence of absorption peaks below 0.30 eV has been reported for example for P3HT blends [62], however, the detection range of the PIA setup does not allow for expanding the measuring range to these energies.

6.4 Singlet Exciton Dissociation

The detected PL spectra of PBDTTT-C:PC₇₀BM blends (ratio 1:1.5) for varying DIO contents are expected to be a superposition of donor and acceptor emission as already mentioned in Section 6.3. The shape of the spectra can be modeled according to

$$PL_{Blend} = A_D \cdot PL_D(\Delta T_0) + A_A \cdot PL_A(int.) . \quad (6.1)$$

Here $PL_D(\Delta T_0)$ and $PL_A(int.)$ are the separately measured initial donor and time-integrated acceptor PL spectra, respectively while $A_{D,A}$ are the corresponding amplitudes. The amplitudes resulting from fits can be found in Table 6.3. As the shown blend spectra can be fitted assuming only the emission from copolymer and fullerene domains, it can be concluded that there is no significant contribution of CT PL in the measured spectral range. The reason for using the initial copolymer PL spectrum, i.e. the one detected around zero delay time, for the fit is that copolymer contributions to the blend emission can only be detected in this time window. Therefore, as the PBDTTT-C PL in principle exhibits a dynamic redshift similar to PCDTBT (see Chapter 5) the time-integrated PL spectrum of the neat copolymer film fails to describe the donor contribution. As can be seen in the top graph of Figure 6.7 a contribution of copolymer PL to the 3 % DIO blend can only be observed for the initial emission (30 ps) while the residual signal is almost exclusively due to acceptor emission (see also Table 6.2). In comparison, the blend without DIO (lower graph of Figure 6.7) shows no donor contribution at all, which is in agreement with the respective result for the time-integrated spectrum. The absence of the characteristic redshift of copolymer emission in the presence of fullerene acceptors indicates a very fast and efficient separation of singlet excitons generated in the donor phase at the donor-acceptor interfaces.

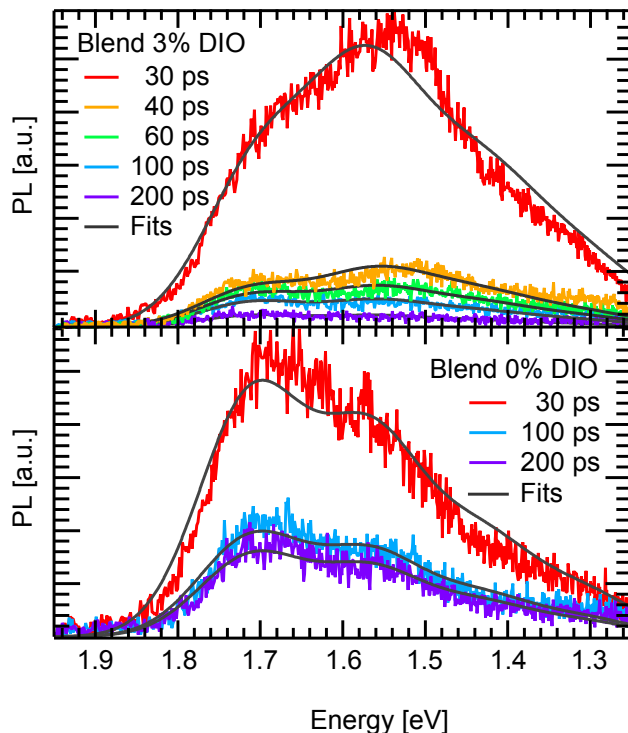


Figure 6.7: Analysis of transient PL spectra of the 0 % (upper graph) and 3 % blend (lower graph) for the first 200 ps after excitation. While the blend without DIO exhibits no significant contribution of copolymer PL, the spectra of the 3 % blend show donor contributions but only around zero delay.

For the blend without additive the time-integrated PL spectrum is found to exhibit no significant copolymer contributions but can be solely attributed to fullerene emission (see Figure 6.8 (a)). This observation implies two different things: first that there have to be large fullerene domains that allow for the radiative decay of singlet excitons and second a good intermixing of the residual fullerenes with the copolymer in order to completely quench the donor PL. The addition of DIO results in a gradual reduction of detected blend PL up to a DIO content of 3 %. For the 10 % blend, however, there is a slight increase of intensity. The observed dependency of emission from the blend as a function of DIO content is in agreement with the measured changes of device efficiency with the highest efficiency being measured for the device showing a minimum in PL. This seems logical since the radiative decay of singlet excitons acts as a loss mechanism in organic solar cells.

Comparing the relative spectral changes as a function of additive content (Figure 6.8 (b)) one finds that the blend PL changes from being acceptor dom-

Blend	0% DIO			3% DIO			
Delay [ps]	30	100	200	30	60	100	200
A_D	—	—	—	356	0	0	0
A_A	242	100	81	278	68	54	25
A_D/A_A	—	—	—	1.28	0	0	0

Table 6.2: Contributions of donor and acceptor PL to the transient spectra shown in Figure 6.7. The spectra were fitted according to Equation 6.1.

inated to being donor dominated (see also amplitudes in Table 6.3). While the 0 % and 1 % spectra clearly exhibit a PL maximum at 1.7 eV resembling the maximum of the fullerene PL spectrum, this peak vanishes when increasing the DIO content to 3 % and 10 %, respectively. The emission from the latter blends is dominated by an emission peak centered at around 1.57 eV which is the energetic position of the maximum of the initial copolymer PL spectrum. The observed relative spectral changes as a function of DIO can in principle be explained with a decrease of the average acceptor domain size allowing for a more efficient quenching of excitons generated within the fullerene domains. The relative increase of the donor contribution however, especially for the 3 % blend that yields the best devices, seems contradictory at first glance. In particular it cannot be explained just considering the aforementioned large acceptor domains that shrink upon increasing DIO content as well as an unaffected polymer-rich donor-acceptor (D-A) intermixed phase as suggested for PTB7 blends by Collins et al. [201]. Instead the results point towards the existence of pure copolymer regions within the intermixed phase.

To further investigate if the average acceptor domain size decreases with increasing the DIO content we compared the PL decay dynamics of transient taken at 1.74 eV for the different blends (Figure 6.9). Especially for the blends exhibiting a lower DIO content these transients mainly represent the decay dynamics of singlet excitons within the fullerene domains and thus are expected to be sensitive to changes of the domain size (see Figure 6.4). For comparison also the decay of the PL signal recorded for a neat PC₇₀BM film is shown. For the latter the decay is found to be monoexponential with a time constant of around 730 ps as shown in Table 6.3. This value represents the average lifetime for excitons created in the fullerene phase. In the blend this average lifetime is reduced ($\tau_2 = 512$ ps) indicating the influence of the interfaces. We find a second low ps time constant τ_1 of 24 ps which is close to the temporal resolution of the measurements of ≈ 20 ps. It can be assumed that this decay channel originates from the dissociation of excitons at the D-A interfaces. Adding DIO leads to a significant acceleration of the PL decay dynamics due to a strong increase of

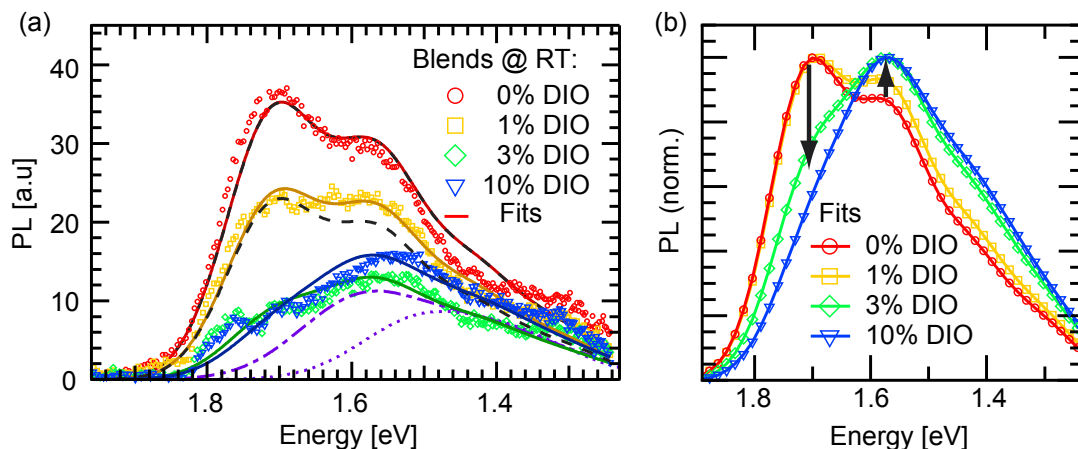


Figure 6.8: Absolute (a) and relative (b) changes of the time-integrated PL spectra obtained for the different blends. Upon adding and increasing the DIO content the spectra change from being fullerene dominated to being copolymer dominated. For comparison also the time-integrated (dotted line) and initial (dash-dotted line) PL spectra of a neat copolymer film are shown in (a).

the relative contribution of τ_1 while the effective exciton lifetime is reduced by a factor of two. The same trends can also be observed when increasing the DIO content to 3 %. These results again point towards a reduction of the average fullerene domain size upon increasing the additive content. The only transient that does not follow the observed trend is the one for the 10 % blend as it looks very similar to the 3 % transient. The fit however indicates a strongly increased contribution of the fast picosecond channel and a slight increase of τ_2 . These observations might be due to the increased contribution of copolymer PL for the 10 % blend and the bigger value of τ_2 could then be interpreted as resulting from the presence of pure copolymer regions within the aforementioned intermixed D-A phase.

6.5 Charge Carrier Generation

Assuming that upon adding DIO the fullerene domains shrink resulting in an increased intermixing between donor and acceptor phases, the interface area will be significantly enhanced. Since it is expected that the number of initially generated charge carriers as well as their precursors — the CT states (polaron pairs) — is also significantly increased. Polarons and CT states can be monitored applying TA spectroscopy as the measured change in optical density is directly proportional to the number of generated absorbing species (compare Section

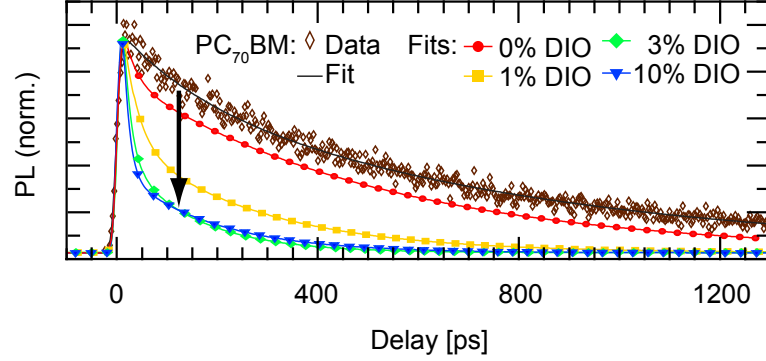


Figure 6.9: Transients taken at 1.74 eV for the different PBDTTT-C:PC₇₀BM blends. For comparison also the transient of a neat PC₇₀BM film taken at the same energy is shown. Adding DIO leads to a faster decay of the PL signal probably due to a more efficient quenching of excitons generated within the fullerene domains.

	A_D	A_A	A_D/A_A	τ_1 [ps]	τ_2 [ps]	A_1/A_2
PC ₇₀ BM	—	—	—	—	726	—
0% DIO	—	3525	—	24	512	0.29
1% DIO	233	2329	0.1	28	264	0.97
3% DIO	693	701	1.0	18	145	1.47
10% DIO	1180	471	2.5	14	186	2.80

Table 6.3: Fitting parameters resulting from analyzing the time-integrated blend spectra (Figure 6.8) employing Equation 6.1 as well as fitting the PL transients shown in Figure 6.9 assuming a biexponential decay.

3.4.1). Figure 6.10 shows the transient spectra of the four analyzed blends around zero delay time (0.5 ps) probed in the energy range between 0.23 and 0.40 eV. According to the previous analysis of the PIA blend spectrum it can be speculated that the transient absorption in this range is due to hole polarons generated within the donor regions with the signal height being proportional to the initial hole population. In literature the probed low-energy absorption band has been associated with hole polaron [62, 200] as well as CT state absorption [71]. These diverging interpretations might be due to the fact that the absorption bands of both CT states and hole polarons are in general spectrally overlapping making it difficult if not impossible to separately detect the TA signature of just one of the two species [26, 75]. However, as free charges and their precursor states are sensitive to changes of the interface area, the measured TA spectra are a good indicator for variations of the blend morphology.

As can be seen from Figure 6.10, the addition of just 1 % of DIO results in an increase of the initial TA signal by more than a factor of two. This means that the initial population of the probed transient species is significantly enhanced probably due to an enhanced photogeneration of the latter. These results clearly indicate a massive increase in interface area due to an enhanced intermixing, which is consistent with the results from the PL study as well as the trends observed for the device efficiency. Surprisingly, the initial height of the transient absorption signal only slightly varies compared to the 1 % blend spectrum if the DIO content is increased. In particular, the TA signal of the 3 % blend is even

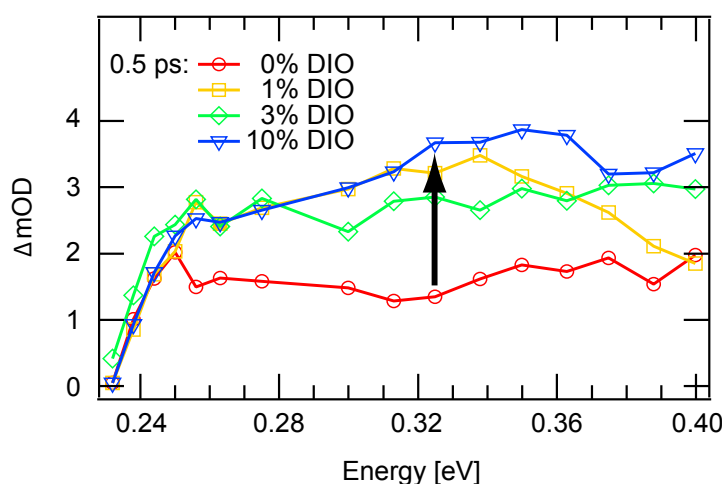


Figure 6.10: Initial transient absorption spectra (0.5 ps) of the four different blends in the range between 0.40 and 0.23 eV. It can be clearly seen that adding DIO leads to a significant increase of the probed transient absorption band.

slightly lower although this blend yields the best device efficiency. In addition the transient spectrum of the 10 % blend seems to be slightly higher in average than the 3 % and the 1% blend which again is contradictory to the results for the device performance. These contrary trends can be understood when recalling that for a good device both charge generation and extraction have to be efficient while for the transient absorption measurements only the first process is of relevance. From a photophysical point of view, adding around 1 % of additive is already sufficient to optimize the blend morphology by significantly increasing the interface area. A further increase of the DIO content, however does not lead to drastic changes of the D-A interface area as indicated by the initial TA spectra. These observations indicate that the further increase in device efficiency observed for these blends might result from morphological changes improving the transport of generated charge carriers by creating percolation pathways. Com-

pared to the massive changes upon adding 1 % of DIO these changes can be viewed as fine-tuning of the morphology by optimizing the mixing/demixing. It again appears reasonable to also assume changes of the intermixed D-A phase in order to fully explain the results consistently, especially when concerning the discrepancy between the TA data for the 3 % and 10 % blends and the respective device performances. In this context the slightly reduced initial TA signal of the 3 % blend compared to the 1 % blend could be explained when assuming the formation of pure donor regions within the intermixed phase, i.e. a partial demixing of the latter, reducing the interface area and thus the initial charge generation. At the same time the high initial TA signal of the 10 % blend might be explained by considering changes of both the fullerene as well as the intermixed phase. In principle the high TA signal of the 10 % blend is in contrast to the reduced device efficiency and the observed increase of copolymer emission (see Section 6.4). A possible explanation that accounts for all these observed changes could be an interplay between the ongoing reduction of the larger fullerene agglomerates and the gradual demixing of the intermixed phase. Both processes would result in the presence of smaller and tendentially isolated fullerene domains that give rise to a strong TA signal but at the same time hinder the efficient transport of generated charges.

The decay dynamics in the probed spectral range are found to be independent of probe energy, which is in agreement with the assignment of a single PIA absorption band present in this spectral region. In contrast to the initial transient absorption spectra, however, the decay dynamics do not change significantly upon adding DIO or varying its content (see Figure 6.11). The transients can be fitted assuming a biexponential decay yielding time constants of $\tau_1 \approx 100$ ps and $\tau_2 \approx 2$ ns, respectively with an amplitude ratio A_1/A_2 of about 0.8. These time constants are significantly shorter than expected lifetimes for free charge carriers within organic semiconductors (see Chapter 2) indicating that the transient signal might rather originate from the absorption of bound charge pairs. Considering the one nanosecond detection window these charge pairs might be interpreted as CT states generated at the D-A interfaces as the interaction of free with trapped charges only becomes relevant on longer time scales (see Chapter 2). Indeed the value of τ_2 is in the typical range of observed lifetimes of CT excitons [82, 83] while τ_1 could depict a picosecond CT decay channel which is in general agreement with results for P3HT- and MEH-PPV-based blends [75, 76, 202]. However, due to the 1 ns detection window, τ_2 and hence also possible contributions by polarons might be underestimated as they are expected to decay on longer timescales [177, 203]. In principle also the presence of intrachain excitons could give rise to the observed decay dynamics, but as this species should be insensitive to changes of the D-A interface it is not considered as probed species.

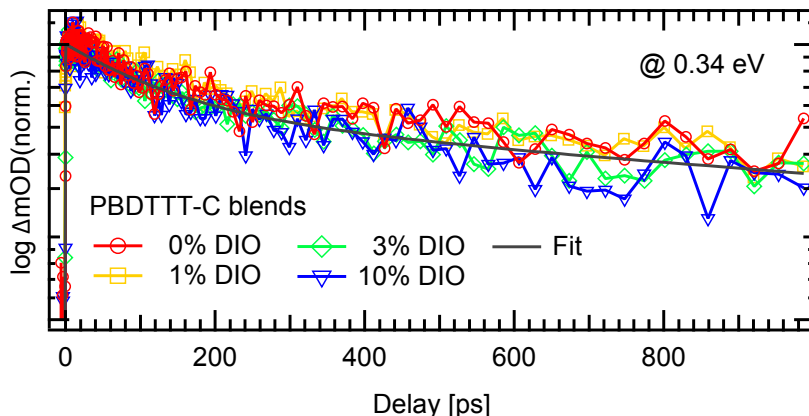


Figure 6.11: While the initial spectra shown in Figure 6.10 vary with changing the DIO content, the transients taken in that energy range (shown 0.34 eV) are almost identical.

As discussed in Chapter 4, the analysis of the temperature dependent decay dynamics can provide additional information about the nature of the decay mechanism and the energy levels involved. Figure 6.12 shows transients taken at 0.34 eV measured at different temperatures for a PTB7:PC₇₀BM blend using the same measurement conditions as for the PBDTTT-C blend measurements. As mentioned before, the photophysics of the PTB7 blend system is expected to be almost identical with the aforementioned one. Indeed, the decay at room temperature is biexponential with $\tau_1 \approx 70$ ps and $\tau_2 \approx 1.3$ ns which is in good agreement with the two time constants found for the PBDTTT-C blends (fit parameters can be found in the caption of Figure 6.12). Reducing the temperature results in a reduced relative contribution of τ_1 , while at 8 K no signature of this channel can be found. These findings indicate that the decay mechanism depicted by τ_1 is thermally activated. This result can be interpreted as a characteristic feature of the CT dissociation process assuming an energetic offset between the CT and the charge separated state which is also indicated by recent results from pump-push-probe experiments [71]. Considering the diffusion assisted nature of the CT dissociation process τ_1 could depict the hole polaron moving away from the interface [76, 202]. Therefore it can be speculated that the probed dynamics are rather influenced by the absorption of bound charge pairs (CT states) than the absorption of free polarons.

For excitation powers $> 20 \mu\text{W}$ the decay dynamics become significantly faster as shown in Figure 6.13 (a). In this excitation regime the response of the samples, i.e. the initial change in optical density, as function of excitation power changes towards a nonlinear dependence (Figure 6.13 (b)). The acceler-

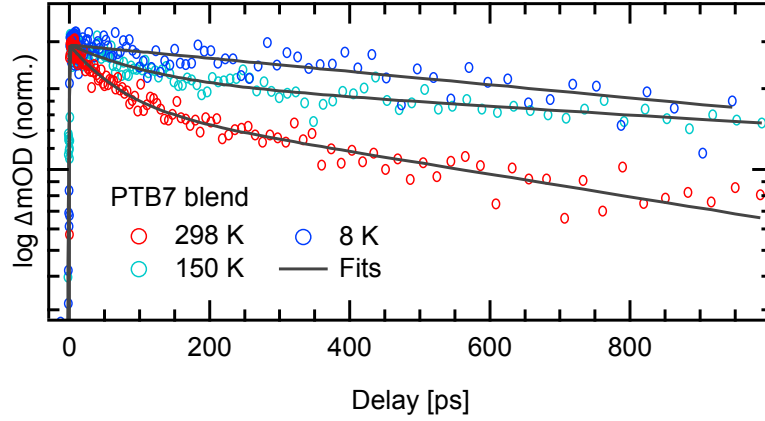


Figure 6.12: Transients taken at 0.34 eV for different temperatures measured for a PTB7:PC₇₀BM blend. At low temperatures the decay dynamics are found to change from a biexponential towards a monoexponential behavior. The respective fitting parameters are: (298K) $\tau_1 = 70$ ps, $\tau_2 = 1.3$ ns, $A_1/A_2 = 0.50$; (150K) $\tau_1 = 110$ ps, $\tau_2 = 3.9$ ns, $A_1/A_2 = 0.26$; (8K) $\tau = 2.2$ ns.

ated decay is due to the presence of an additional fast decay channel with a time constant τ_1 of around 30 ps (see also Table 6.4). This additional decay mechanism can be attributed to a bimolecular recombination of the probed species that only becomes relevant at high excitation densities, i.e. at high densities of the photoexcited states. However, as the presented results were recorded using excitation powers ≤ 20 μW a dominant contribution of this decay mechanism can be neglected.

Exc. power [μW]	τ_1 [ps]	τ_2 [ps]	τ_3 [ps]	A_1	A_2	A_3
10	—	370	ns	—	1.12	0.75
20	—	190	3250	—	1.83	1.98
40	66	230	1450	2.92	0.93	3.28
60	27	229	ns	3.26	4.43	1.48
80	36	207	900	5.56	1.89	3.28

Table 6.4: Time constants and associated amplitudes found for the transients shown in Figure 6.13 assuming a triexponential decay model.

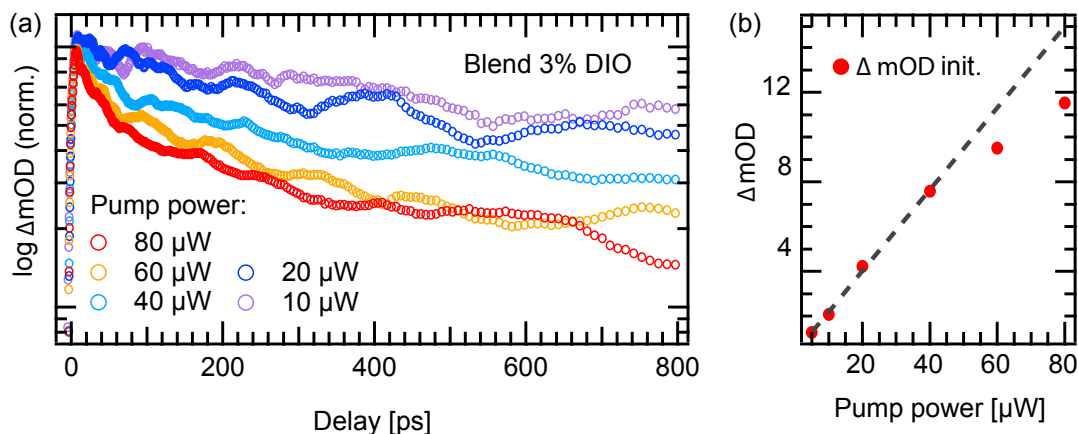


Figure 6.13: (a) Excitation power dependence of the decay dynamics probed at 0.38 eV (a) indicating the presence of an additional fast decay channel for excitation powers $> 20 \mu\text{W}$. (b) For these excitation powers the initial rise of the transients is found to develop a nonlinear dependency.

6.6 Blend Topography

The topography of the different blend films was analyzed using atomic force microscopy (AFM) in the so-called intermittent contact mode (measurements by Mario Zerson from the university of Chemnitz). In this mode not only the height profile of the sample can be measured but also the phase change of the cantilever-oscillation is mapped. These changes are due to the interaction of the tip with the sample surface, caused by surface forces such as adhesion and friction. The magnitude of this phase change gives additional information about the analyzed material system, for example elasticity, and can help to identify the local morphology or even differentiate between incorporated materials [204, 205, 206]. The resulting topography maps together with the respective phase maps for the different blends are shown in Figure 6.14.

For the 0 % blend one finds large round agglomerates with diameters in the range of 100-200 nm embedded within a smooth surrounding (Figure 6.14 (a)). The same structures can also be identified in the phase image (Figure 6.14 (b)) indicating that the material properties in these regions differ from the ones of the surrounding. Adding 0.6 % of DIO leads to a significant change of the blend: The large domains get smaller and link while the surface becomes smoother (Figure 6.14 (c) and (d)). These changes are reflected by the corresponding phase map (Figure 6.14 (d)) indicating smaller nanoscale structures. Increasing the DIO content to 3 % (Figure 6.14 (e) and (f)) leads to a further reduction of the average

domain size and flattening of the surface of the film. Compared to the transition from 0 % to 0.6 %, however the changes are not fundamental. Adding 10 % DIO (Figure 6.14 (g) and (h)) inverts the aforementioned trends: The sample displays larger particles and the surface becomes rougher. Interestingly the phase images for all samples containing DIO (Figures 6.14 (d), (f) and (h)) exhibit comparable nanostructures that do not change significantly upon increasing the additive content.

The large domains that can be identified in the AFM scans of the blend film without DIO are comparable to structures observed for PTB7-based blends without additive using TEM and have been identified with fullerene domains [119, 207]. The tendency of fullerenes to form large round agglomerates has also been reported for other copolymer- and polymer-based blends [118, 122] so that it is very likely that the large structures are indeed fullerene clusters. This assumption is in agreement with the PL measurements indicating the emission from large fullerene domains. Considering the absence of donor PL, it can be assumed that the blend surrounding the large clusters has to be a well intermixed D-A phase in order to effectively quench the generated excitons. It can be speculated that the fullerene domains exhibit a higher degree of order compared to the intermixed D-A phase and act as energetic traps for electrons which would explain the comparably small device efficiency for the devices without DIO. In general the AFM scans only give information about the surface of a sample but in this case, as the height of the round structures is almost one fifth of the total film thickness, it can be assumed that the scans also give a qualitative picture of the actual blend morphology.

According to the aforementioned picture assuming the presence of large fullerene clusters, the AFM scans indicate that adding DIO results in smaller and linked fullerene domains. As a result the D-A interface area is highly increased allowing for more efficient exciton harvesting which is consistent with the drop in fullerene PL, the accelerated PL decay and the dramatic rise in generated charge pairs as well as the increase in device efficiency.

Increasing the DIO content to 3 % leads to a better intermixing of donor and acceptor phase and the fullerene phase forms a well interlinked network. This interpretation is in agreement with the observed additional drop in fullerene PL, the even faster PL decay and the further increase of device efficiency while it seems contradictory to the almost constant initial charge generation yield and the observed increase in donor PL. A possible explanation is that the AFM scans are rather insensitive to slight changes of the intermixed D-A phase. In particular a demixing of the latter that would compensate for the increase in D-A interface area due to the formed fullerene network and at the same time promote donor emission might not be detectable.

Adding 10 % DIO inverts the aforementioned trends: The fullerene phase

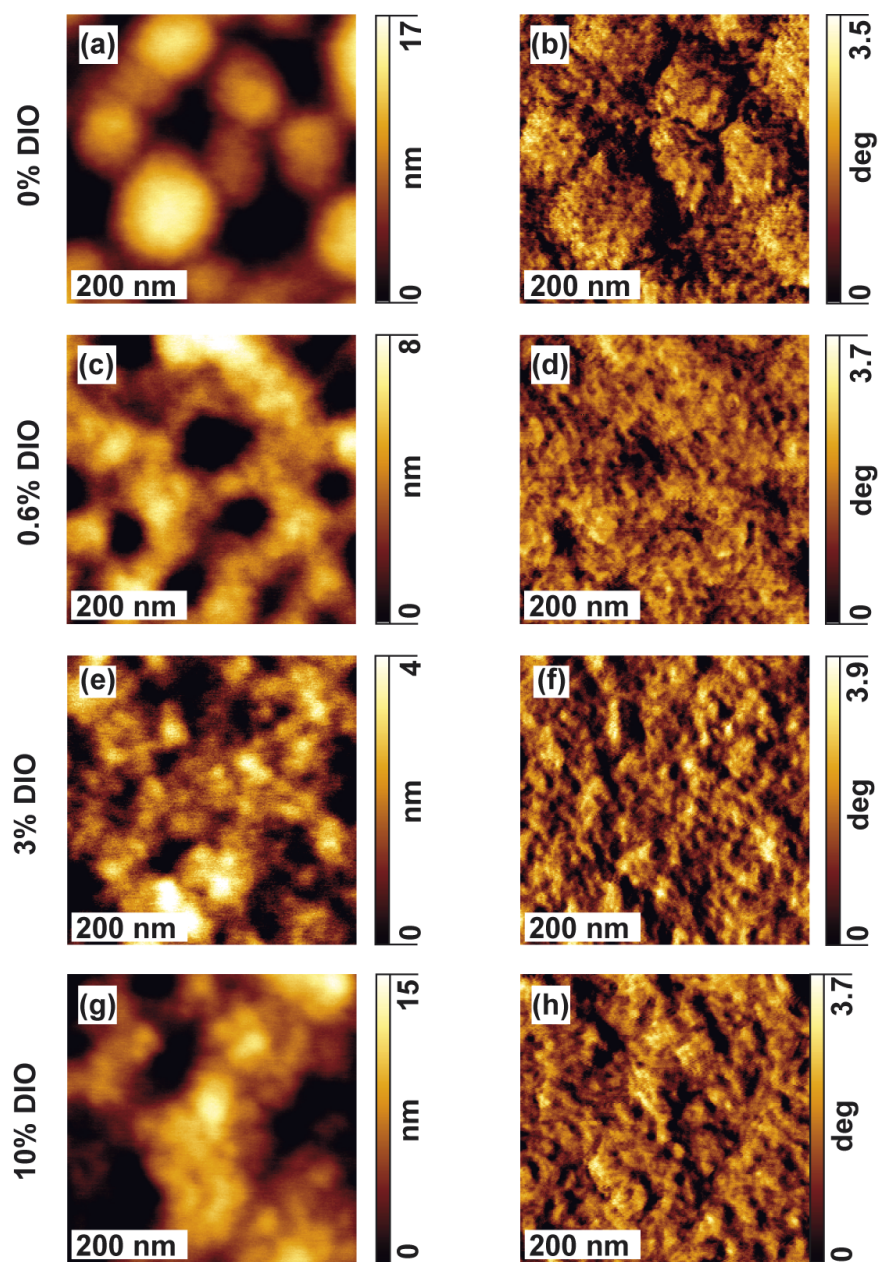


Figure 6.14: Topography maps (left) together with the corresponding phase change maps (right) for blends prepared with different amounts of DIO. The AFM scans clearly indicate drastic changes of the blend morphology upon adding DIO.

seems to become coarser and the surface rougher. In general this trend is again in agreement with the observed decrease in device efficiency and the increase in donor PL. At this point it has to be mentioned that the 10 % blend might be affected by gradual morphological changes that take place after film production

due to the large DIO content. Hence the surface morphology measured by AFM might differ from the one investigated by means of IV and time-resolved optical measurements directly after film preparation. However, the reduced device efficiency and the increased emission from the blend point towards a demixing of donor and acceptor phase resulting in a reduction percolation pathways thus hampering the transport of charges.

The changes of the fullerene phase upon adding and increasing the DIO content found in the AFM scans match the major trends observed in the preceding studies very well. In particular the reduction of fullerene domain size and linking of these domains for small DIO contents and the formation of branched percolation pathways for increasing the DIO content to 3 % is in perfect agreement with the results of the optical studies and the measured device characteristics. Changes of the intermixed phase, i.e. a partial demixing and the formation of pure donor regions, as indicated by the time-resolved PL and TA results could not be observed in the AFM scans. This might be due to the fact that the film surface is covered by a thin intermixed layer that is not affected by the DIO content which would explain the similar phase images measured for the blends with DIO.

As the additive is expected to solely influence the solubility of the fullerene the opposite results for PCPDTBT- and PBDTTT-C-based blends in term of blend intermixing might be due to the fact that the PCPDTBT-fullerene blend is an example for an intercalating system, which means that fullerenes can be located between the copolymer side chains, while PBDTTT-C is a non-intercalating system [190]. Since fullerenes will tend to leave the donor regions to form clusters in the case of PCDTBT while for PBDTTT-C-based blends they tend to intermix with the donor phase, probably in order to reduce the energy of the respective blend system.

6.7 Summary

In this chapter the influence of processing additive DIO on the morphology of PBDTTT-C:PC₇₀BM blends was thoroughly investigated. By combining the results of picosecond time-resolved PL and TA experiments on the one hand and IV and AFM measurements on the other hand we are able to draw a detailed picture of the changes of the blend morphology as a function of DIO content. Our findings indicate that the optimization of the blend nanostructure regarding the balance of charge generation and transport is the crucial parameter in order to optimize device efficiency. The trends observed in the aforementioned experiments are qualitatively summarized in Figure 6.15 while Figure 6.16 illustrates the underlying morphological changes.

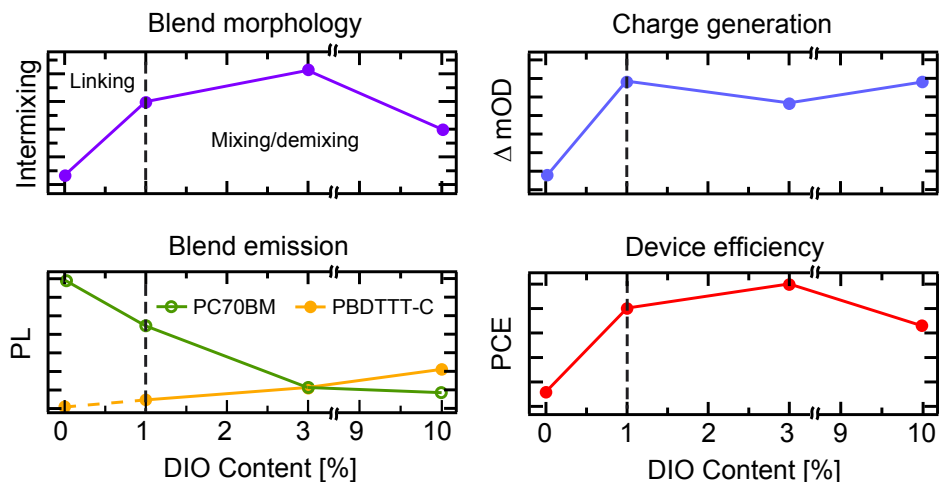


Figure 6.15: Qualitative graphs summarizing the results of the optical (bottom left and top right), morphological (top left) and electrical (bottom right) studies described in this chapter. The observed changes can be explained by the drastic influence of DIO on the blend morphology. In general two regimes can be distinguished: The linking of fullerene domains when adding only a little amount of DIO and the mixing/demixing regime for higher DIO contents.

Starting with the blend without additive the properties of the blend film are mainly defined by the presence of large fullerene clusters with diameters around 100-200 nm. These domains act as traps for generated charge carriers and give rise to the characteristic acceptor PL observed for this blend. The absence of copolymer PL indicates that the phase surrounding the fullerene clusters is initially a well intermixed donor-acceptor phase. Adding around 1 % of DIO significantly changes this morphology. The fullerene domains get smaller and link leading to a massive increase of D-A interface area. As a result excitons generated within the fullerene phase are quenched more efficiently and the number of generated charges is significantly increased boosting the device efficiency by a factor of more than two. The best device efficiency, however, is achieved when increasing the additive content to 3 % which is mainly due to an improvement of the charge transport properties of the blend while the initial generation of charges only slightly varies. It can be seen as fine tuning of the intermixing of the blend to find a balance between generation and transport of charges. This balance is destroyed when increasing the DIO content to 10 % probably due to a reduction of percolation pathways as the fullerenes form isolated domains within the intermixed phase. The almost constant charge generation yields for all DIO-containing blends and the gradual increase of donor PL with increasing

DIO content indicate that during the mixing and demixing of the blend also the second so-called intermixed phase changes and pure donor regions are formed. Whether or not the fullerenes tend to intermix with the donor phase or form clusters might depend on the energetics of the blend system and could differ significantly depending on the employed polymer donor material and in particular the fact if intercalation takes place or not.

The presented results show that also for blend systems based on next-generation copolymer donor materials the optimization of the blend morphology is a key parameter. For the analyzed PBDTTT-C:PC₇₀BM films an increase of device efficiency by a factor of more than two could be achieved emphasizing the importance of an improved nanostructure of the blend regarding its charge generation and transport properties. Since the direct control of the latter is not possible up to now, the detailed understanding of the correlation between morphology and processing parameters is crucial. As shown in this chapter the analysis of the photophysical properties and in particular their dynamics combined with complementary electrical and topological measurements proves to be a powerful tool that helps to decipher this correlation.

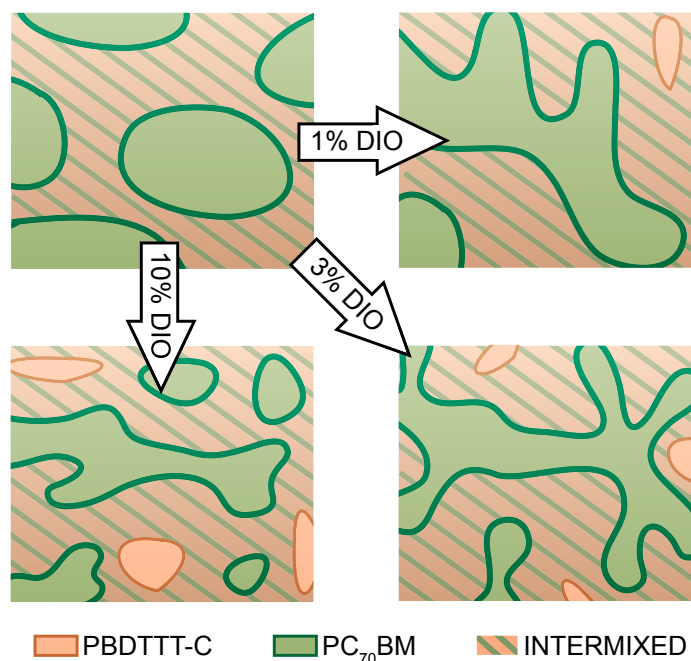


Figure 6.16: Schemes illustrating the changes of the blend morphology upon adding different amounts of DIO as derived from the detailed study described in this chapter.

Zusammenfassung

Der Fokus dieser Arbeit liegt auf der Untersuchung des Transportes von Anregungsenergie, d.h., der Exzitonendynamik sowie der Generierung von Ladungsträgern in organischen Halbleitern. Durch das Verständnis der relevanten Schritte, welche dem elementaren Licht-zu-Ladung-Konversionsprozess zugrunde liegen, und der Identifizierung möglicher Verlustmechanismen konnten hilfreiche Informationen für die zukünftige Optimierung von organischen Solarzellen gewonnen werden. Drei wesentliche Aspekte wurden im Rahmen dieser Arbeit untersucht: Der fundamentale Prozess der Exzitonenerzeugung, das verbesserte Nutzen des Sonnenspektrums durch Verwendung neuartiger Donormaterialien sowie die Optimierung der Morphologie der aktiven Schicht der Solarzelle im Hinblick auf die Ladungsgenerierung. Alle drei Aspekte sind von großer Bedeutung für die Effizienzsteigerung organischer Solarzellen und daher Bestandteil intensiver Untersuchungen in diesem Forschungsgebiet.

Da die meisten der Prozesse sich auf der sub-ns bis ns Zeitskala abspielen, wurden im Rahmen dieser Arbeit zwei verschiedene Picosekunden-zeitaufgelöste Versuchsaufbauten realisiert und verwendet, nämlich die zeitaufgelöste PL-Spektroskopie sowie die transiente Absorptionsspektroskopie. Die Ergebnisse dieser Messungen wurden jeweils ergänzt um nicht zeitaufgelöste optische Charakterisierungsmethoden und komplementäre morphologische Untersuchungen.

Die Effizienz von organischen Solarzellen könnte im Prinzip erheblich gesteigert werden, wenn durch Singlet Fission erzeugte Triplet Exzitonon genutzt werden könnten. Besagter Prozess würde nicht nur zwei Exzitonon pro absorbiertem Photon liefern, sondern Bauteile würden darüber hinaus von der größeren Exzitononendiffusionslänge profitieren. Unsere temperaturabhängigen zeitaufgelösten PL Messungen am prototypischen organischen Halbleiter Rubren zeigen allerdings, dass auch für ein System, das eine signifikante Singlet Fission Rate aufweist, dieser Mechanismus durch die Anwesenheit von Grenzflächenzuständen deutlich unterdrückt werden kann. Durch Analyse der PL Zerfallsdynamik von wohldefinierten Rubrenmorphologien, die ein immer stärker beschränktes räumliches Anregungsvolumen aufweisen, ist es uns möglich, den direkten Einfluss des beschränkten Volumens auf die Zerfallsdynamik der erzeugten Singlet Exzitonon zu

untersuchen. Es zeigt sich, dass in Einkristallen ein signifikanter Teil der Singlet Exzitonen am Singlet Fission Prozess mit einer Zeitkonstante von 20 ps beteiligt ist, während dieser Kanal in Rubren Mikrokristallen nicht identifiziert werden kann. In den Mikrostrukturen relaxieren die Exzitonen hauptsächlich durch Quenching an Grenzflächenzuständen mit einer assoziierten Zeitkonstante von 100 ps. Der Grund dafür ist, dass dieser Mechanismus eine Energiebarriere aufweist, die nur halb so hoch ist wie die des Singlet Fission Prozesses. Da die Abmessungen der Mikrostrukturen von derselben Größenordnung sind wie typische organische Dünnschicht-Bauteile und diese Bauteile ähnliche Grenzflächenzustände aufweisen können, z.B. an der Grenze zwischen geordneten und ungeordneten Regionen innerhalb einer auf Polymeren basierten Solarzelle, sollten diese Ergebnisse bei der Realisierung von Triplet-basierter OPV berücksichtigt werden.

Einer der erfolgreichsten Ansätze der letzten vier Jahre um die Effizienz von organischen Solarzellen zu erhöhen, ist die Verwendung von neuen und komplexeren Copolymer-Donormaterialien. Diese Materialien sind speziell designt um das Sonnenlicht effizienter absorbieren zu können und die Leerlaufspannung der Zelle zu erhöhen. Allerdings ist wenig bekannt über die Natur der angeregten Zustände dieser Systeme sowie der Kopplung zwischen eben diesen Energieniveaus, d.h., über den Transport von Anregungsenergie. Anhand von vergleichenden Absorptions- und PL Messungen sowie einer Solvatochromie Studie am prominenten Copolymer PCDTBT, seiner Bauteile sowie dem neu synthetisierten Molekül BPT-Carbazol war es uns möglich, den Ursprung der beiden charakteristischen Absorptionsbänder zu ermitteln. BPT-Carbazol entspricht dabei einem Copolymer-Kettensegment ohne Akzeptorgruppen. Während wir das hochenergetische Band mit einer Anregung identifizieren konnten, welche auf der Copolymerkette zwischen zwei benachbarten Akzeptorgruppen lokalisiert ist, kann das niederenergetische Absorptionband einem teilweisen Ladungstransferzustand von eben diesem Segment zu einer benachbarten Akzeptorgruppe zugeordnet werden. Dieser teilweise Ladungsübertrag sorgt für eine schnelle und effiziente Kopplung der beiden elektronischen Niveaus des Copolymers. Wie durch die Ergebnisse der zeitaufgelösten PL und nicht zeitaufgelösten PLE Messungen angedeutet, bestimmt diese interne Relaxation die Photophysik des Copolymer:Fulleren Blendsystems. Im Speziellen wurde kein relevanter konkurrierender Relaxationskanal gefunden, sodass die Photoanregung des Copolymers, unabhängig von der Anregungswellenlänge, zu einem Elektronentransfer zum Fulleren führt, falls das Exziton die Grenzfläche erreicht. Unter Ausnutzung der Kopplung kann daher die Absorption des Donormaterials prinzipiell weiter in den NIR-Bereich erweitert werden, indem die gekoppelten funktionalen Gruppen und damit die CT-Absorption modifiziert werden. Der einzige limitierende Faktor hierbei ist die mit der Reduzierung der Bandlücke einhergehende Verringerung der treibenden Kraft für die Ladungsträgertrennung, was ab einem gewissen Punkt einen Kom-

promiss notwendig macht. In diesem Zusammenhang könnte es allerdings von Nutzen sein, dass Elektron und Loch auf dem Copolymer bereits teilweise getrennt sind, was die notwendige Kraft für die Ladungstrennung möglicherweise verringert. Generell stellt der Vergleich der optischen Eigenschaften des Copolymer mit denen seiner Bauteile ein nützliches Werkzeug dar, um die unterschiedlichen funktionellen Gruppen neuer und komplexer Donormaterialien entschlüsseln zu können.

Ein zweiter wichtiger Aspekt, um die Effizienz organischer Solarzellen steigern zu können, betrifft die Optimierung der Morphologie der aktiven Schicht. Diese Aufgabe ergibt sich aus der offensichtlichen Diskrepanz zwischen der Exzitonendiffusionslänge (≈ 10 nm) und der Absorptionslänge des Sonnenlichts (≈ 100 nm). Da eine direkte Kontrolle der Morphologie bis jetzt nicht möglich ist, hängt die Herstellung von effizienten Solarzellen entscheidend von Produktionsparametern ab, welche die Blendmorphologie in positiver Weise beeinflussen — auch für Solarzellen, die auf neuen Copolymermaterialien basieren. Für letzteren Typ konnten gute Ergebnisse erzielt werden, indem man anstelle des Ausheizens der Zelle ein Prozessierungsadditiv verwendet hat. Der Vorteil des Additivs liegt darin, dass ein zusätzlicher Prozessschritt bei der Herstellung vermieden werden kann. Unsere sorgfältige Analyse der morphologischen Veränderungen von Blends, basierend auf dem hocheffizienten Copolymer PBDDTT-C als Funktion des DIO Additivgehaltes zeigen, dass beobachtbare Verbesserungen der Zellen hauptsächlich von einer besseren Durchmischung des Blends herrühren. Die Kombination von Ergebnissen der zeitaufgelösten PL und TA sowie IV-Messungen und AFM-Experimenten deuten dabei darauf hin, dass insbesondere die Akzeptorphase vom Additiv beeinflusst wird. Während die Zugabe von 0.6-1.0 % DIO bereits die Verkleinerung und Vernetzung von großen Fulleren-Domänen bewirkt, kann die Effizienz insgesamt mehr als verdoppelt werden, wenn man 3 % Additiv hinzugibt. Dieses Maximum resultiert aus einem “Fine Tuning” der Blendmorphologie, indem eine optimale Balance zwischen effizienter Ladungsgenerierung durch Grenzflächenerhöhung und Transport entlang sich ausbildender Perkolationpfade erreicht wird. Diese Balance wird allerdings zerstört, wenn der DIO-Anteil auf 10 % erhöht wird, was vermutlich in der Verringerung von Perkolationspfaden durch sich ausbildende kleinere isolierte Fulleren-Domänen begründet ist. Dies wiederum führt zu einem Abfallen der Effizienz. Wie durch die zeitaufgelösten PL und TA Messungen angedeutet, ist die zweite Phase, eine durchmischte Donor-Akzeptor Phase, ebenfalls von den morphologischen Veränderungen betroffen. Insbesondere für DIO-Konzentrationen von > 1 % deuten die Ergebnisse darauf hin, dass sich reine Donorregionen in dieser Mischphase ausbilden, sprich sich letztere entmischt. Die Ergebnisse zeigen, dass auch für Blends basierend auf neuartigen Copolymer-Donormaterialien die Optimierung der Morphologie einen Schlüsselparameter darstellt. Da die direkte Kontrolle

der Morphologie der aktiven Schicht allerdings bis jetzt nicht möglich ist, ist ein detailliertes Verständnis der Korrelation zwischen Morphologie und Prozessparametern um so wichtiger. Hierbei stellt die kombinierte Studie der Photo-physikalischen Eigenschaften und insbesondere deren Dynamik, kombiniert mit elektrischen und morphologischen Untersuchungen einen nützlichen Ansatz dar, um diese Korrelation zu entschlüsseln.

Conclusions

The focus of this work was to analyze the transport of excitation energy, i.e. the exciton dynamics and the generation of charge carriers in organic semiconductor systems. By understanding the relevant steps involved in this elementary light-to-charge conversion process and identifying possible loss mechanisms helpful information for the future optimization of organic solar cells could be obtained. Three main aspects have been investigated in the context of this work: the fundamental process of exciton generation, the improved harvesting of the solar spectrum by new donor materials and the optimization of the morphology of the active layer with regard to charge generation. All three aspects are important for increasing the efficiency of organic photovoltaic devices and therefore the subject of intensive studies in this field of research.

As most of the processes take place on the sub-ns to ns time scale, two different picosecond time-resolved techniques have been installed and employed in this work — namely time-resolved PL and transient absorption spectroscopy. The results of the time-resolved measurements were supplemented by steady state optical characterization methods and complementary morphological studies.

The efficiency of organic solar cells could be significantly enhanced if triplet excitons generated by singlet fission could be harvested. The aforementioned process not only yields two excitons by absorbing just one photon but devices would also benefit from the longer triplet exciton diffusion length. Our temperature dependent time-resolved PL measurements on the prototypical organic semiconductor rubrene, however, show that even for a system exhibiting significant singlet fission rates the presence of interfacial states can significantly suppress this mechanism. By analyzing the PL decay dynamics of well-defined rubrene morphologies exhibiting an increasing degree of confinement we were able to directly study the influence of spatial confinement on the decay dynamics of the generated singlet excitons. We find that while in bulk single crystals a significant amount of singlets undergo the fission process with a time constant of 20 ps this channel cannot be identified for rubrene microcrystals. In the latter the excitons mainly decay by a quenching channel within 100 ps associated with the interfacial states as this mechanism exhibits an energetic barrier which is only half that of the singlet fission process. As the dimensions of the microstructures are found to be on typical length scales of organic thin film devices and comparable quenching sites could be present for example between ordered and disordered regions within a polymer-based solar cell, the results have to be considered for triplet-based OPV.

One of the most successful approaches for enhancing the efficiency of organic solar cells in the last four years is to employ new and more complex copolymer donors. These materials are designed for a more efficient harvesting of the solar

spectrum and an increased open circuit voltage of the devices. Nevertheless little is known about the nature of the excited states and in particular about the coupling between these states, i.e. the transport of excitation energy. By carrying out comparative steady state absorption and PL as well as solvatochromic shift measurements of the prominent copolymer PCDTBT, its building blocks as well as the newly synthesized BPT-carbazole we could clearly identify the nature of its two distinct absorption bands. BPT-carbazole resembles a segment of the copolymer backbone without the acceptor groups. While we attribute the high-energy absorption band to an intrachain excitation that is confined between two adjacent acceptor units, the low-energy band can be associated with a partially CT type excitation between the latter segment and an adjacent acceptor unit. The partial charge transfer guarantees for a fast and efficient coupling of the electronic levels of the copolymer. As indicated by time-resolved PL and steady state PLE measurements this internal relaxation governs the photophysics of the copolymer-fullerene blends. In particular no significant competing relaxation channel could be identified so that, independent of wavelength, photoexcitation of the copolymer leads to an electron transfer towards the fullerene if the exciton reaches an interface. Therefore — by utilizing the coupling between both units — the donor absorption can in principle be further expanded into the NIR by modifying the donor and acceptor groups and thus the CT absorption. The only limiting factor is that the reduction of the donor bandgap comes with the reduction of driving force for charge separation so that at some point a compromise has to be made. Concerning this aspect, however, it might be beneficial that electron and hole are already pre-separated on the copolymer backbone which might reduce the required driving force. In general we consider the approach of comparing the optical properties of a copolymer with those of its building blocks a useful tool that can be used to decipher the different functional units of new and complex donor materials.

A second important aspect for increasing the efficiency of organic solar cells is to optimize the morphology of the active layer. This task arises from the discrepancy between the diffusion length of generated singlet excitons (≈ 10 nm) and the ideal layer thickness (≈ 100 nm). Since the direct control of the morphology is not possible until now, the fabrication of efficient solar cell devices crucially depends on processing parameters that positively affect the blend morphology — also for the systems based on new copolymer materials. For the latter, instead of annealing the device good results have been achieved when employing a processing additive which has the advantage that no additional processing step is needed. Our careful analysis of the morphological changes of blends based on high-efficient copolymer PBDTTT-C as a function of DIO additive content show that observed device improvements are mainly due to an increased intermixing of the blend. The combined results of time-resolved PL and TA as well as IV and

AFM measurements indicate that mainly the acceptor phase is influenced by the additive. While adding only 0.6-1.0 % of DIO already results in a shrinking and linking of large fullerene clusters present in the blend, the devices efficiencies can be more than doubled when adding 3 % of DIO. This maximum is due to a “fine tuning” of the blend morphology creating an optimized balance between a high charge generation yield by increasing the interface area and charge transport via emerging percolation pathways. This balance is destroyed when increasing the DIO content to 10 % probably due to a reduction of percolation pathways as the fullerenes form smaller isolated domains, resulting in a drop in device efficiency. As indicated by the time-resolved PL and TA measurements the second phase, an intermixed donor-acceptor phase, is also affected by the morphological changes. Especially for DIO contents > 1 % the results point towards the formation of pure donor regions within this intermixed phase, i.e. a demixing of the latter. The results show that a detailed understanding of the correlation between morphology and processing parameters is crucial in order to optimize up-to-date organic solar cells. The presented results show that also for blend systems based on next-generation copolymer donor materials, the optimization of the blend morphology is a key parameter. Since the direct control of the latter is not possible up to now, the detailed understanding of the correlation between morphology and processing parameters is crucial. The presented analysis of the photophysical properties and in particular their dynamics combined with complementary electrical and topological measurements proves to be a powerful tool that helps to decipher this correlation.

Experimental Details

A.1 Preparation of Thin Film Samples

Copolymers PCDTBT, PTB7 (both 1-material) and PBDTTT-C (Solarmer Materials Inc.), polymer P3HT (Rieke Metals Inc.) as well as PC₇₀BM (Solenne BV) were used for thin film preparation without further purification. The donor materials were all dissolved in chlorobenzene at concentrations of 7 mg/ml (PCDTBT), 8 mg/ml (PBDTTT-C), 10 mg/ml (PTB7) and 20 mg/ml (P3HT), respectively under inert atmosphere. For the blend films the necessary amount of PC₇₀BM was added to the solution and in case of the PBDTTT-C-based blends optionally 0.6, 1, 3 and 10 % by volume DIO were added. For the pure PC₇₀BM films the fullerene was dissolved in chlorobenzene at a concentration of 10 mg/ml. All thin films were then fabricated by spin cast onto quartz substrates from solution. Right before spin casting the substrates were cleaned using soap water followed by ultrasonic bath cleaning in deionized water, acetone and isopropanol, respectively for ten minutes each. Remaining contaminants were removed treating the sample with an oxygen plasma for 30 seconds. PBDTTT-C and PTB7-based films were fabricated at 1400 rpm for 60 s yielding film thicknesses between 100 and 120 nm. The spin parameters for PCDTBT-based films and P3HT films were 800 rpm for 30 s followed by 2000 rpm for 10 s resulting in around 100 nm thick films while the fullerene film was fabricated at 800 rpm for 60 s.

A.2 Synthesis of PCDTBT Building Blocks

All commercially available starting materials, reaction intermediates, reagents and solvents for the synthesis of the co-monomers and monomer CDTBT were obtained from Acros, Sigma Aldrich or VWR and used without further purification or modification, unless otherwise noted. The synthesis were carried out in an inert atmosphere and all molecules were characterized employing ^1H - and ^{13}C -NMR spectroscopy. The spectra were recorded employing a Bruker Avance 400 or a Bruker Avance III 600 MHz spectrometer. Both the synthesis of the N-(1-octylnonyl)carbazole (carbazole) and 4,7-di(thien-2-yl)-2,1,3-benzothiadiazole (DTBT) were described elsewhere [109, 208]. The co-monomer CDTBT was synthesized by a palladiumcatalyzed Stille-type coupling using N-(1-octylnonyl)-2-bromocarbazole and 4-(thien-2-yl)-7-[2-(tributylstannyl)thien-5-yl]-2,1,3-benzothiadiazole [209]. BPTcarbazole was synthesized dissolving N-(1-octylnonyl)-2,7-dibromocarbazole (1.00 g; 1.77 mmol) and 5-phenyl-2-thienylboronic acid (0.84 g; 4.12 mmol) in a mixture of 50 ml toluene, 10 ml water and 10 ml 2N aq. KOH solution. Then tetrakis(triethylphosphin)palladium was added and the resultant mixture was heated at 80° overnight. The reaction mixture was allowed to cool, poured into water (300 ml) and the crude product was extracted with DCM (3 x 200 ml). The organic extracts were washed with brine (2 x 200 ml), dried over MgSO_4 and the solvent was removed under reduced pressure. Purification was carried out via column chromatography (hexane) to yield a yellow solid (340 mg; 29 %).

A.3 Femtosecond Laser Setup

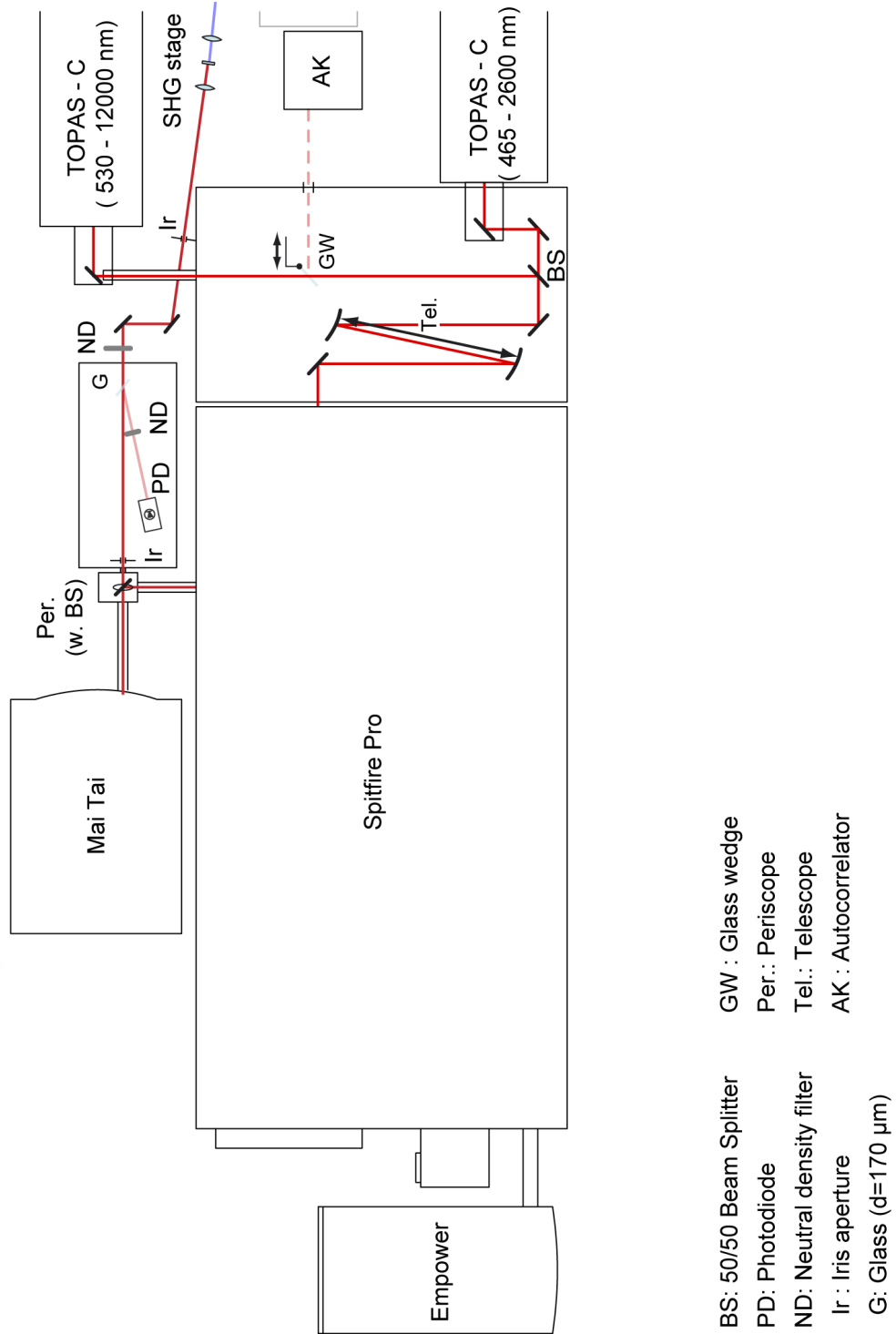


Figure A.1: Scheme of the femtosecond laser setup (after image by V. Baianov).

A.4 Cryostat Holder and TA Alignment Stage

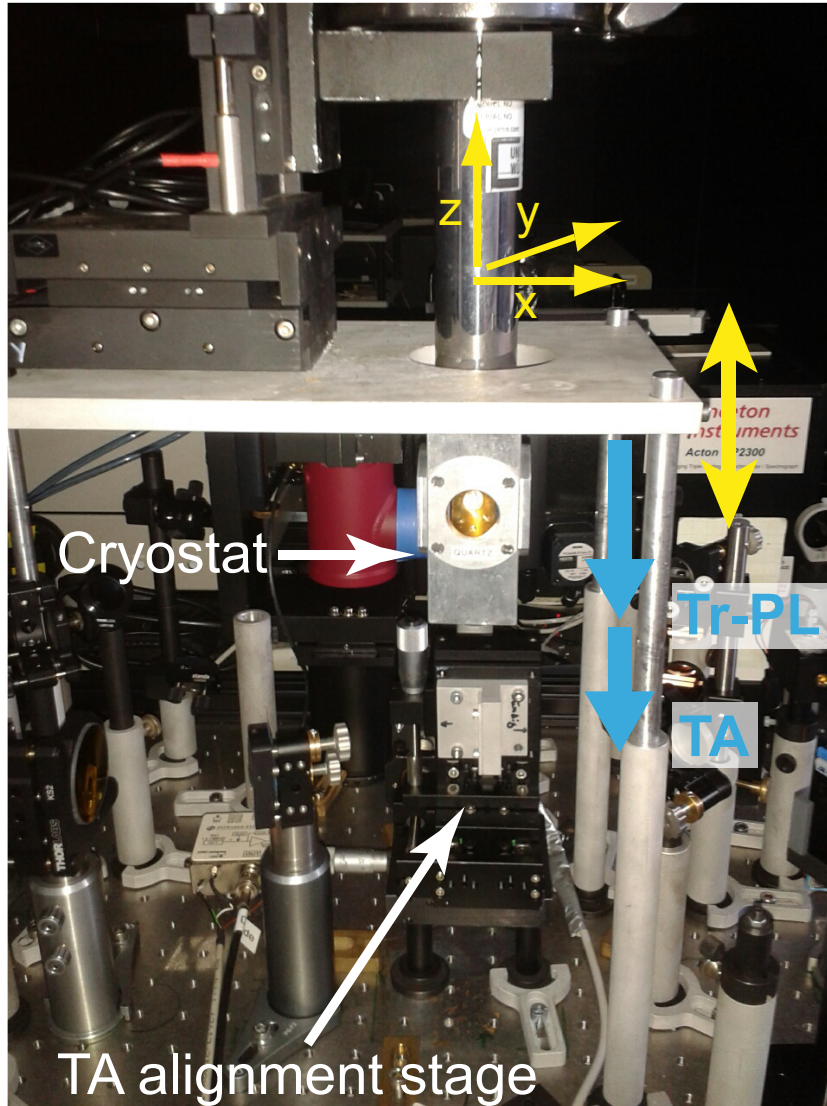
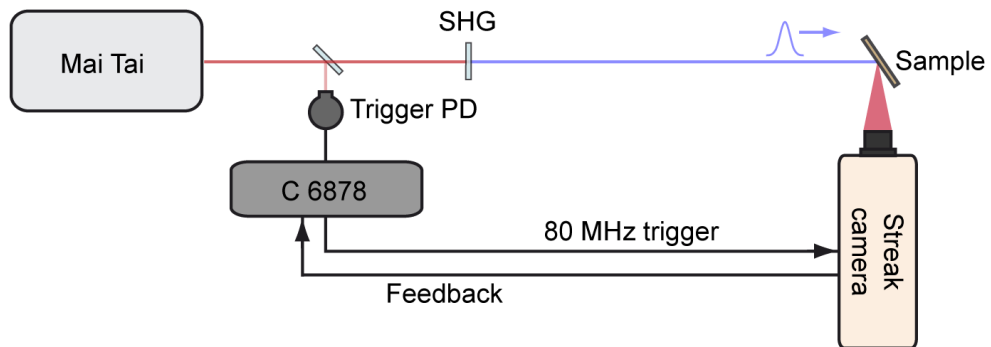


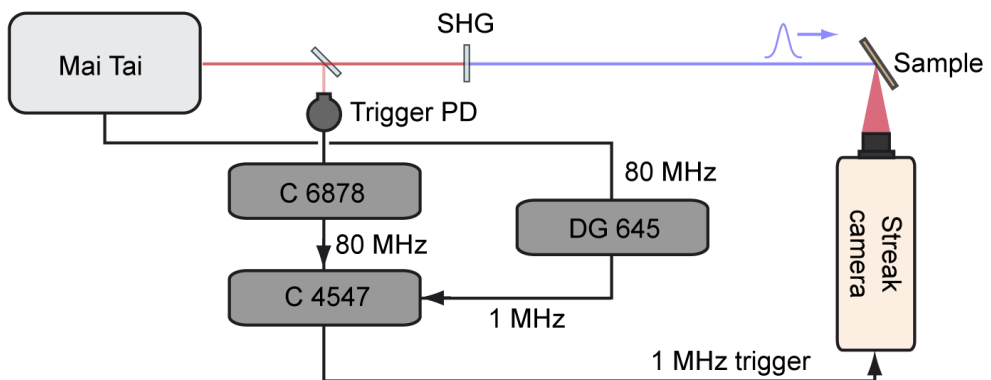
Figure A.2: Photograph of the adjustable cryostat holder and table as well as the modular TA beam alignment stage. The cryostat is mounted to a x,y,z -linear stage module allowing for a precise positioning of the sample. Changing the height of the cryostat table allows for switching between the two measuring modes (Tr-PL, TA) and the alignment position, respectively. The latter position allows for placing the TA beam alignment stage on the optical table that can be equipped with a pinhole, a sample holder and a motorized knife edge scanner.

A.5 Streak Measurement Modes

(1) Synchro scan + 80 MHz excitation



(2) Single sweep + 80 MHz excitation



(3) Single sweep + 1 kHz excitation

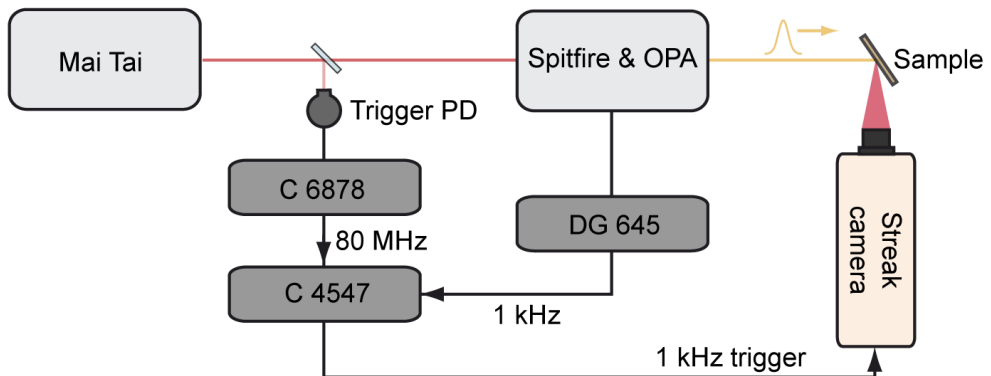


Figure A.3: Schematic overview of the experimental layouts of the different streak measuring modes employed in this work.

APPENDIX B

List of Publications

Full Papers

- Paper-1 Excitation Dynamics in Low Band Gap Donor-Acceptor Copolymers and Blends, **B. Giesekeing**, B. Jäck, E. Preis, S. Jung, M. Forster, U. Scherf, C. Deibel, V. Dyakonov, *Adv. En. Mat.* 2, 1477–1482 (2012).
- Paper-2 Effects of Characteristic Length Scales on the Exciton Dynamics in Rubrene Single Crystals, **B. Giesekeing**, T. Schmeiler, B. Müller, C. Deibel, B. Engels, V. Dyakonov, J. Pflaum, *submitted* (2014).
- Paper-3 The Effect of Diiodooctane on the Charge Carrier Generation in Organic Solar Cells Based on the Copolymer PBDTTT-C, **B. Giesekeing**, A. Zusan, M. Zerson, V. Dyakonov, R. Magerle, C. Deibel, *submitted* (2014).
- Paper-4 Interplay Between Exciton Decay Rate and Impurity Occupation in Strongly Mn-doped and Partially Compensated Bulk GaAs, F. Münzhuber, T. Henn, **B. Giesekeing**, G. V. Astakhov, T. Kießling, V. Dyakonov, W. Ossau, L.W. Molenkamp, *submitted* (2014).
- Paper-5 Being Trapped on Acceptor Islands: Influence of Structural Changes on the Nongeminate Recombination in PTB7:PC₇₁BM Solar Cells, A. Zusan, **B. Giesekeing**, J. Rauh, A. Baumann, K. Tvingstedt, B. Mueller, M. Gluecker, V. Dyakonov, C. Deibel, *to be submitted* (2014).

Contributions to Conferences

Talks

1. Exciton Dynamics in Copolymer PCDTBT and a PCDTBT:PC₇₀BM Blend System, **B. Giesekeing**, B. Jäck, C. Deibel, V. Dyakonov, *DPG-Frühjahrstagung in Dresden*, talk, HL 55.11 (2011).
2. Exciton Dynamics in Low Band Gap Donor-Acceptor Copolymers and Blends, **B. Giesekeing**, B. Jäck, E. Preis, S. Jung, M. Forster, U. Scherf,

- C. Deibel, V. Dyakonov, *DPG-Frühjahrstagung in Berlin*, talk, CPP 33.5 (2012).
3. The Local Environment Affects the Exciton Dynamics in Rubrene Single Crystals, **B. Giesecking**, T. Schmeiler, B. Müller, C. Deibel, V. Dyakonov, J. Pflaum, *SPIE Optics and Photonics in San Diego*, talk, 8811-34 (2013).
 4. Preparation and optical characterization of self-organized surface structures on polyaromatic single crystals, T. Schmeiler, **B. Giesecking**, S. Thoms, J. Pflaum, *FOR 1809 Projekttreffen in Niederstetten*, talk, P7 (2013).

Poster presentations

1. Time-Resolved Photoluminescence and Transient Absorption Spectroscopy of Organic Semiconductors, **B. Giesecking**, D. Kreier, B. Jäck, C. Deibel, V. Dyakonov, *International Cluster Conference Organic Photovoltaics in Würzburg*, poster presentation (2010).
2. Probing Polaron and Singlet Exciton Dynamics by Transient Absorption and Time-Resolved Spectroscopy, **B. Giesecking**, B. Jäck, A. Kämpgen, J. Gorenflot, C. Deibel, V. Dyakonov, *Workshop "Fundamentale Funktionsweise organischer Solarzellen" in München*, poster presentation (2011).
3. Time-Resolved Photoluminescence Spectroscopy of PCDTBT and PCDTBT:[70]PCBM Blends, B. Jäck, **B. Giesecking**, C. Deibel, V. Dyakonov, *DPG-Frühjahrstagung in Dresden*, poster presentation (2011).
4. Influence of Additive on the Exciton Dynamics in PTB7:PC₇₀BM Blends, B. Müller, **B. Giesecking**, C. Deibel, V. Dyakonov, *DPG-Frühjahrstagung in Berlin*, poster presentation (2012).
5. Excitation Dynamics in Low Band Gap Donor-Acceptor Copolymers and Blends, **B. Giesecking**, B. Jäck, E. Preis, S. Jung, M. Forster, U. Scherf, C. Deibel, V. Dyakonov, *MRS Spring Meeting in San Francisco*, poster presentation (2012).
6. Preparation and optical characterization of self-organized surface structures on polyaromatic single crystals, T. Schmeiler, **B. Giesecking**, S. Thoms, J. Pflaum, *FOR 1809 Projekttreffen in Niederstetten*, poster presentation (2013).
7. Radiative decay times in highly p-doped and partially compensated GaAs:Mn, F. Münzhuber, T. Henn, **B. Giesecking**, G. V. Astakhov, T.

Kiessling, V. Dyakonov, W. Ossau, L. W. Molenkamp *Gorden Research Conference "Spin Dynamics in Nanostructures" in Hong Kong*, poster presentation (2013).

ANHANG C

Danksagung

An dieser Stelle möchte ich mich bei denjenigen bedanken, die mich während meiner Arbeit tatkräftig unterstützt und so zu einem erfolgreichen Gelingen der Promotion beigetragen haben. Ich bedanke mich bei:

- Herrn Prof. Dr. Vladimir Dyakonov für die gute Betreuung dieser Arbeit am Lehrstuhl der EP 6 und das Vertrauen, welches er mir entgegengebracht hat, indem er mir das fs-Lasersystem, dessen Aufbau und Betrieb in meine Hände gelegt hat. Außerdem möchte ich mich für die hilfreichen Kommentare und Diskussionen bezüglich meiner wissenschaftlichen Veröffentlichungen und Kongressvorträge bedanken.
- Prof. Dr. Jean Geurts für die Bereitschaft, mir als Zweitgutachter zur Verfügung zu stehen und die interessierte Begutachtung dieser Arbeit.
- Dr. Carsten Deibel für die gute Betreuung meines wissenschaftlichen Schaffens, die Unterstützung beim Aufbau des Lasersystems mit der ein oder anderen Optik und die kritischen, aber stets konstruktiven und hilfreichen Diskussionen bezüglich meiner wissenschaftlichen Resultate, Poster, Vorträge und Veröffentlichungen und natürlich die Korrektur dieser Arbeit.
- Prof. Dr. Jens Pflaum für die Initialisierung des Rubren-Projektes und die gute Zusammenarbeit bei selbigem. Insbesondere bedanken möchte ich mich für die interessanten und sehr anregenden physikalischen Diskussionen, welche mir nähergebracht haben, dass Ordnung auch so ihren Reiz hat und natürlich für die Korrektur von Teilen diese Arbeit.
- meinen ehemaligen Diplomanden Daniel Kreier, Bert Jäck und Benjamin Müller, die mich beim Aufbau des Lasersystems und vielen Messungen tatkräftig unterstützt haben.
- Markus Steeger aus der Lambert-Gruppe für die Unterweisung und Hilfe bei allen Absorptions-, PL- und PLE-Messungen in der flüssigen Phase sowie den Film-PLE-Messungen, die ich in meiner Arbeit verwendet habe.
- den organischen Chemikern aus Wuppertal: Prof. Dr. Ullrich Scherf, Dr. Michael Forster und Stefan Jung für die Synthese der Copolymerbausteine

ganz nach meinem Wunsch und die unkomplizierte und gute Zusammenarbeit an der PCDTBT-Geschichte.

- Prof. Dr. Magerle und Mario Zerson von der Uni Chemnitz für die AFM-Messungen und die gute Zusammenarbeit bei unserem PBDTTT-C-Projekt.
- Zusi für das unermüdliche Herstellen von Proben, die tolle Zusammenarbeit bei den “DIO tales”, die IV-Kurven und das immer freundliche Repetieren der Prozessparameter, bis auch ich sie mir mal gemerkt habe.
- André für die wichtige Unterstützung im Kampf gegen das laserfeindliche Laborklima — insbesondere die Klimaanlage — und seinen Einsatz für Lasersicherheit.
- Valentin für das Zur-Verfügung-Stellen seiner geheimen Optiksammlung und seiner Erfahrung im Umgang mit Lasersystemen bei Aufbau und Umbau des optischen Schemas des Lasersystems.
- Christian, meinem treuesten Büronachbarn, für das tapfere Beibringen der (rudimentären) Python-Kenntnisse, seine psychologische Unterstützung und das erfolglose Näherbringen des geräuschlosen Kauens.
- Michi und Roland, der leider viel zu früh abgesprungenen “besseren Hälfte” des Büros E11.
- Hannes und Hex für all die Hilfe rund um Labview, Messdatenaufnahme und Computer.
- Julien für die anregenden Photophysik-Diskussionen und teils verstörende Privatdialoge.
- den Jungs aus der alten EP 6 Garde, die da wären Andy, Alex Förtig, Alex (Rüdi), Jens, Markus und Volker für die schönen Stunden am Lehrstuhl, bei DPG und Futschi, bei fachlichen und insbesondere auch fachfremden Inhalten. Bei Andy möchte ich mich darüber hinaus für das Korrigieren von Teilen dieser Arbeit bedanken.
- last but not least bei meinem Lasersystem, welches mir nach störrischer erster Hälfte die Treue gehalten (und funktioniert) hat, bis ich alle wichtigen Messungen im Kasten hatte.

Ein ganz besonderer Dank gebührt an dieser Stelle meinen Eltern, die mich nicht nur während meines gesamten Studium “gesponsert” haben, sondern auch

ein riesiger Rückhalt für mich waren in den letzten Jahren und immer für mich da, wenn ich mal wieder frustriert und deprimiert war, weil im Labor nichts klappte. Ebenso gebührt dieser Dank meiner Schwester, die mich in dieser Zeit immer herzlichst umsorgt, bekocht und beherbergt hat, auch wenn Burn-out Björn nicht immer ein kommunikationswilliger Tischnachbar war.

Darüber hinaus möchte ich mich bei meinen guten Freunden in Würzburg bedanken, die mich glücklicherweise den großen Teil meines Studiums und meiner Doktorarbeit begleitet haben und Würzburg für mich mit Leben gefüllt haben: Gabi & Philipp, mein Roomie Jo, Christian, Eva & Philip, Blacky und Tobi.

And saving the best till last I'd like to thank my girlfriend Marta for always being there for me, giving me strength and motivation and making me a better person.

ANHANG D

Erklärung gemäß §5(2) der Promotionsordnung

Hiermit erkläre ich, dass ich die vorliegende Arbeit selbständig und ohne fremde Hilfe unter Verwendung der angegebenen Quellen und Hilfsmittel angefertigt habe.

Björn Giesecking

Würzburg, den 08.04.2014

Literaturverzeichnis

- [1] BP. *BP Energy Outlook 2030*. London, UK, 2013.
- [2] International Energy Agency (IEA). *World Energy Outlook 2012*. Presentation to the press, London, UK, 2012.
- [3] International Energy Agency (IEA). *2012 Key World Energy Statistics*. Paris, France, 2012.
- [4] G. Lanzani. *The Photophysics behind Photovoltaics and Photonics*. Wiley-VCH, Weinheim, Germany, 1st edition, 2012.
- [5] A. E. Becquerel. *Comptes Rendus de l'Académie des Sciences*, 9(25):561–567, 1839.
- [6] D. M. Chapin, C. S. Fuller, and G. L. Pearson. *Journal of Applied Physics*, 25(5):676, 1954.
- [7] M. A. Green, K. Emery, Y. Hishikawa, W. Warta, and E. D. Dunlop. *Progress in Photovoltaics: Research and Applications*, 21(5):827–837, 2013.
- [8] W. Shockley and H. J. Queisser. *Journal of Applied Physics*, 32(3):510, 1961.
- [9] C. K. Chiang, C. R. Fincher, Y. W. Park, A. J. Heeger, H. Shirakawa, E. J. Louis, S. C. Gau, and Alan G. MacDiarmid. *Physical Review Letters*, 39(17):1098–1101, 1977.
- [10] W. Ma, C. Yang, X. Gong, K. Lee, and A. J. Heeger. *Advanced Functional Materials*, 15(10):1617–1622, 2005.
- [11] NREL National Center For Photovoltaics. *Research Cell Efficiency Records*. <http://www.nrel.gov/ncpv/>, 2013-10-10, 2013.
- [12] M. Pope and C. E. Swenberg. *Electronic Processes in Organic Crystals and Polymers*. Oxford University Press, New York, 2nd edition, 1999.
- [13] N. J. Turro, V. Ramamurthy, and J. C. Scaiano. *Modern Molecular Photochemistry of Organic Molecules*. University Science Books, Sausalito, USA, 1st edition, 2010.
- [14] G. Dennler, M. C. Scharber, and C. J. Brabec. *Advanced Materials*, 21(13):1323–1338, 2009.

- [15] C. Deibel and V. Dyakonov. *Reports on Progress in Physics*, 73(9):096401, 2010.
- [16] C. E. Mortimer and U. Müller. *Chemie*. Georg Thieme Verlag, Stuttgart, 9th edition, 2007.
- [17] W. Demtröder. *Experimentalphysik 3*. Springer-Verlag, Berlin, 3rd edition, 2005.
- [18] M. Kasha. *Radiation Research*, 20(1):55, 1963.
- [19] Kasha, M., H. R. Rawls, and M. El-Bayoumi. *Pure Applied Chemistry*, 11:371–393, 1965.
- [20] H. Haken and H. C. Wolf. *Atom- und Quantenphysik*. Springer-Verlag, Berlin, 8th edition, 2004.
- [21] M. A. El-Sayed. *The Journal of Chemical Physics*, 36(2):573–574, 1962.
- [22] M. B. Smith and J. Michl. *Chemical Reviews*, 110(11):6891–6936, 2010.
- [23] V. Settels. Quantum chemical description of ultrafast exciton self-trapping in perylene based materials. PhD thesis, 2012.
- [24] V. Settels, W. Liu, J. Pflaum, R. F. Fink, and B. Engels. *Journal of Computational Chemistry*, 33(18):1544–1553, 2012.
- [25] N. S. Sariciftci (ed.). *Primary Photoexcitations in Conjugated Polymers: Molecular Exciton versus Semiconductor Band Model*. World Scientific, Singapore, 1997.
- [26] T. M. Clarke and J. R. Durrant. *Chemical Reviews*, 110(11):6736–6767, 2010.
- [27] I.G. Hill, A. Kahn, Z.G. Soos, and Jr. Pascal. *Chemical Physics Letters*, 327(3–4):181–188, 2000.
- [28] J.-L. Bredas, J. Cornil, and A. J. Heeger. *Advanced Materials*, 8(5):447–452, 1996.
- [29] A. S. Davydov. *Theory of Light Absorption in Molecular Crystals*. Naukova Dumka, Kiev, 1951.
- [30] T. Förster. *Annalen der Physik*, 437(1–2):55–75, 1948.
- [31] D. L. Dexter. *The Journal of Chemical Physics*, 21(5):836, 1953.

- [32] E. Silinsh and V. Capek. *Organic Molecular Crystals, Interaction, Localization and Transport Phenomena*. AIP Press, New York, USA, 1st edition, 1994.
- [33] H. Nishimura, T. Yamaoka, K. Mizuno, M. Iemura, and A. Matsui. *Journal of the Physics Society Japan*, 53(11):3999–4008, 1984.
- [34] P. Reinecker, H. Haken, and H. C. Wolf. *Organic Molecular Aggregates*. Springer-Verlag, Berlin, 1983.
- [35] M. Bednarz, P. Reinecker, E. Mena-Osteritz, and P. Bäuerle. *Journal of Luminescence*, 110(4):225–231, 2004.
- [36] S. C. Graham, D. D. C. Bradley, R. H. Friend, and C. Spangler. *Synthetic Metals*, 41(3):1277–1280, 1991.
- [37] J. Kern, S. Schwab, C. Deibel, and V. Dyakonov. *physica status solidi (RRL) – Rapid Research Letters*, 5(10-11):364–366, 2011.
- [38] Z. Shuai, J.-L. Bredas, and W.P. Su. *Chemical Physics Letters*, 228(4-5):301–306, 1994.
- [39] M. Liess, S. Jeglinski, Z. V. Vardeny, M. Ozaki, K. Yoshino, Y. Ding, and T. Barton. *Physical Review B*, 56(24):15712–15724, 1997.
- [40] A. J. Heeger. *Chemical Society Reviews*, 39(7):2354–2371, 2010.
- [41] E. Hennebicq, G. Pourtois, G. D. Scholes, L. M. Herz, D. M. Russell, C. Silva, S. Setayesh, A. C. Grimsdale, K. Müllen, J.-L. Bredas, and D. Beljonne. *Journal of the American Chemical Society*, 127(13):4744–4762, 2005.
- [42] L. Lüer, H.-J. Egelhaaf, D. Oelkrug, G. Cerullo, G. Lanzani, B.-H. Huisman, and D. de Leeuw. *Organic Electronics*, 5(1-3):83–89, 2004.
- [43] J. E. Kroeze, T. J. Savenije, M. J. W. Vermeulen, and J. M. Warman. *The Journal of Physical Chemistry B*, 107(31):7696–7705, 2003.
- [44] A. R. Buckley, M. D. Rahn, J. Hill, J. Cabanillas-Gonzalez, A. M. Fox, and D. D. C. Bradley. *Chemical Physics Letters*, 339(5-6):331–336, 2001.
- [45] E. J. W. List, C. Creely, G. Leising, N. Schulte, A. D. Schlüter, U. Scherf, K. Müllen, and W. Graupner. *Chemical Physics Letters*, 325(1-3):132–138, 2000.
- [46] S. Brazovskii and N. Kirova. *Chemical Society Reviews*, 39(7):2453, 2010.

-
- [47] T.-Q. Nguyen, J. Wu, V. Doan, B. J. Schwartz, and S. H. Tolbert. *Science*, 288(5466):652–656, 2000. PMID: 10784444.
- [48] F. C. Spano. *The Journal of Chemical Physics*, 122(23):234701–234701–15, 2005.
- [49] J. Clark, C. Silva, R. H. Friend, and F. C. Spano. *Physical Review Letters*, 98(20):206406, 2007.
- [50] F. C. Spano, J. Clark, C. Silva, and R. H. Friend. *The Journal of Chemical Physics*, 130(7):074904, 2009.
- [51] E. A. Silinsh, A. Klimkans, S. Larsson, and V. Capek. *Chemical Physics*, 198(3):311–331, 1995.
- [52] V. Capek and E. A. Silinsh. *Chemical Physics*, 200(3):309–318, 1995.
- [53] F. Ortmann, F. Bechstedt, and K. Hannewald. *physica status solidi (b)*, 248(3):511–525, 2011.
- [54] T. Holstein. *Annals of Physics*, 8(3):343–389, 1959.
- [55] K. Hannewald, V. M. Stojanovic, J. M. T. Schellekens, P. A. Bobbert, G. Kresse, and J. Hafner. *Physical Review B*, 69(7):075211, 2004.
- [56] T. Holstein. *Annals of Physics*, 8(3):325–342, 1959.
- [57] D. K. Campbell, A. R. Bishop, and K. Fesser. *Physical Review B*, 26(12):6862–6874, 1982.
- [58] K. Fesser, A. R. Bishop, and D. K. Campbell. *Physical Review B*, 27(8):4804, 1983.
- [59] W. P. Su, J. R. Schrieffer, and A. J. Heeger. *Physical Review Letters*, 42(25):1698–1701, 1979.
- [60] W. P. Su, J. R. Schrieffer, and A. J. Heeger. *Physical Review B*, 22(4):2099–2111, 1980.
- [61] H. Bässler. *physica status solidi (b)*, 175(15):15–56, 1993.
- [62] R. Österbacka, C. P. An, X. M. Jiang, and Z. V. Vardeny. *Science*, 287(5454):839–842, 2000.
- [63] R. E. Smalley. *Reviews of Modern Physics*, 69(3):723–730, 1997.

- [64] M. Riede, T. Mueller, W. Tress, R. Schueppel, and K. Leo. *Nanotechnology*, 19(42):424001, 2008.
- [65] B. Giesecking, B. Jäck, E. Preis, S. Jung, M. Forster, U. Scherf, C. Deibel, and V. Dyakonov. *Advanced Energy Materials*, 2(12):1477–1482, 2012.
- [66] C. J. Brabec, G. Zerza, G. Cerullo, S. De Silvestri, S. Luzzati, J. C. Hummelen, and S. Sariciftci. *Chemical Physics Letters*, 340(3–4):232–236, 2001.
- [67] I.-W. Hwang, C. Soci, D. Moses, Z. Zhu, D. Waller, R. Gaudiana, C.J. Brabec, and A. J. Heeger. *Advanced Materials*, 19(17):2307–2312, 2007.
- [68] R. D. Pensack, K. M. Banyas, and J. B. Asbury. *The Journal of Physical Chemistry C*, 114(12):5344–5350, 2010.
- [69] G. J. Dutton, W. Jin, J. E. Reutt-Robey, and S. W. Robey. *Physical Review B*, 82(7):073407, 2010.
- [70] A. C. Morteani, P. Sreearunothai, L. M. Herz, R. H. Friend, and C. Silva. *Physical Review Letters*, 92(24):247402, 2004.
- [71] A. A. Bakulin, A. Rao, V. G. Pavelyev, P. H. M. Van Loosdrecht, M. S. Pshenichnikov, D. Niedzialek, J. Cornil, D. Beljonne, and R. H. Friend. *Science*, 335(6074):1340–1344, 2012.
- [72] S. D. Dimitrov and J. R. Durrant. *Chemistry of Materials*, 2013.
- [73] F. Etzold, I. A. Howard, N. Forler, D. M. Cho, M. Meister, H. Mangold, J. Shu, M. R. Hansen, K. Müllen, and F. Laquai. *Journal of the American Chemical Society*, 134(25):10569–10583, 2012.
- [74] J. Guo, H. Ohkita, H. Benten, and S. Ito. *Journal of the American Chemical Society*, 132(17):6154–6164, 2010.
- [75] T. Drori, J. Holt, and Z. V. Vardeny. *Physical Review B*, 82(7):075207, 2010.
- [76] L. W. Barbour, M. Hegadorn, and J. B. Asbury. *Journal of the American Chemical Society*, 129(51):15884–15894, 2007.
- [77] S. Cook, R. Katoh, and A. Furube. *The Journal of Physical Chemistry C*, 113(6):2547–2552, 2009.
- [78] D. Veldman, Ö. Ipek, S. C. J. Meskers, J. Sweelssen, M. M. Koetse, S. C. Veenstra, J. M. Kroon, S. S. van Bavel, J. Loos, and R. A. J. Janssen. *Journal of the American Chemical Society*, 130(24):7721–7735, 2008.

- [79] M. Hallermann, S. Haneder, and E. Da Como. *Applied Physics Letters*, 93(5):053307, 2008.
- [80] M. Hallermann, I. Kriegel, E. Da Como, J. M. Berger, E. von Hauff, and J. Feldmann. *Advanced Functional Materials*, 19(22):3662–3668, 2009.
- [81] K. Tvingstedt, K. Vandewal, F. Zhang, and O. Inganäs. *The Journal of Physical Chemistry C*, 114(49):21824–21832, 2010.
- [82] M. A. Loi and M. Scharber. *Advanced Functional Materials*, 17(13):2111–2116, 2007.
- [83] D. Jarzab, F. Cordella, J. Gao, M. Scharber, H.-J. Egelhaaf, and M. A. Loi. *Advanced Energy Materials*, 1(4):604–609, 2011.
- [84] D. Veldman, J. J.A.M. Bastiaansen, B. M.W. Langeveld-Voss, J. Sweelssen, M. M. Koetse, S. C.J. Meskers, and R. A.J. Janssen. *Thin Solid Films*, 511–512:581–586, 2006.
- [85] S. Cook, H. Ohkita, J. R. Durrant, Y. Kim, J. J. Benson-Smith, J. Nelson, and D. D. C. Bradley. *Applied Physics Letters*, 89(10):101128, 2006.
- [86] Y. W. Soon, T. M. Clarke, W. Zhang, T. Agostinelli, J. Kirkpatrick, C. Dyer-Smith, I. McCulloch, J. Nelson, and J. R. Durrant. *Chemical Science*, 2(6):1111, 2011.
- [87] P. Langevin. *Annales de Chimie et de Physique*, 28(28):433, 1903.
- [88] C. Arndt, U. Zhokhavets, M. Mohr, G. Gobsch, M. Al-Ibrahim, and S. Sensfuss. *Synthetic Metals*, 147(1–3):257–260, 2004.
- [89] A. Pivrikas, N. S. Sariciftci, G. Juska, and R. Österbacka. *Progress in Photovoltaics: Research and Applications*, 15(8):677–696, 2007.
- [90] G. Garcia-Belmonte, P. P. Boix, J. Bisquert, M. Sessolo, and H. J. Bolink. *Solar Energy Materials and Solar Cells*, 94(2):366–375, 2010.
- [91] D. Käfer and G. Witte. *Physical Chemistry Chemical Physics*, 7(15):2850, 2005.
- [92] R. W. I. de Boer, M. E. Gershenson, A. F. Morpurgo, and V. Podzorov. *physica status solidi (a)*, 201(6):1302–1331, 2004.
- [93] T. Schmeiler. *Rubrene*. Master’s thesis, Würzburg, 2011.

- [94] J. Takeya, M. Yamagishi, Y. Tominari, R. Hirahara, Y. Nakazawa, T. Nishikawa, T. Kawase, T. Shimoda, and S. Ogawa. *Applied Physics Letters*, 90(10):102120–102120–3, 2007.
- [95] H. Najafov, B. Lee, Q. Zhou, L. C. Feldman, and V. Podzorov. *Nature Materials*, 9(11):938–943, 2010.
- [96] P. Irkhin and I. Biaggio. *Physical Review Letters*, 107(1):017402, 2011.
- [97] A. Ryasnyanskiy and I. Biaggio. *Physical Review B*, 84(19):193203, 2011.
- [98] R. J. Stöhr, G. J. Beirne, P. Michler, R. Scholz, J. Wrachtrup, and J. Pflaum. *Applied Physics Letters*, 96(23):231902, 2010.
- [99] H. Kasai, H. S. Nalwa, H. Oikawa, S. Okada, H. Matsuda, N. Minami, A. Kakuta, K. Ono, A. Mukoh, and H. Nakanishi. *Japanese Journal of Applied Physics*, 31(Part 2, No. 8A):L1132–L1134, 1992.
- [100] D. H. Park, S. G. Jo, Y. K. Hong, C. Cui, H. Lee, D. J. Ahn, J. Kim, and J. Joo. *Journal of Materials Chemistry*, 21(22):8002–8007, 2011.
- [101] M. C. Scharber, D. Mühlbacher, M. Koppe, P. Denk, C. Waldauf, A. J. Heeger, and C. J. Brabec. *Advanced Materials*, 18(6):789–794, 2006.
- [102] N. Blouin, A. Michaud, D. Gendron, S. Wakim, E. Blair, R. Neagu-Plesu, M. Belletete, G. Durocher, Y. Tao, and M. Leclerc. *Journal of the American Chemical Society*, 130(2):732–742, January 2008.
- [103] A. J. Heeger. *Chemical Society Reviews*, 39(7):2354–2371, 2010.
- [104] J. Hou, M.-H. Park, S. Zhang, Y. Yao, L.-M. Chen, J.-H. Li, and Y. Yang. *Macromolecules*, 41(16):6012–6018, 2008.
- [105] F. He and L. Yu. *The Journal of Physical Chemistry Letters*, 2(24):3102–3113, 2011.
- [106] M. Svensson, F. Zhang, O. Inganäs, and M.R. Andersson. *Synthetic Metals*, 135-136(0):137–138, 2003.
- [107] S. Admassie, O. Inganäs, W. Mammo, E. Perzon, and M. R. Andersson. *Synthetic Metals*, 156(7-8):614–623, 2006.
- [108] S. Beaupre, M. Belletete, G. Durocher, and M. Leclerc. *Macromolecular Theory and Simulations*, 20(1):13–18, 2011.

- [109] N. Blouin, A. Michaud, and M. Leclerc. *Advanced Materials*, 19(17):2295–2300, 2007.
- [110] S. H. Park, A. Roy, S. Beaupre, S. Cho, N. Coates, J. S. Moon, D. Moses, M. Leclerc, K. Lee, and A. J. Heeger. *Nature Photonics*, 3(5):297–302, 2009.
- [111] K. Xerxes Steirer, Paul F. Ndione, N. Edwin Widjonarko, Matthew T. Lloyd, Jens Meyer, Erin L. Ratcliff, Antoine Kahn, Neal R. Armstrong, Calvin J. Curtis, David S. Ginley, Joseph J. Berry, and Dana C. Olson. *Advanced Energy Materials*, 1(5):813–820, 2011.
- [112] Y. Sun, C. J. Takacs, S. R. Cowan, J. H. Seo, X. Gong, A. Roy, and A. J. Heeger. *Advanced Materials*, 23(19):2226–2230, 2011.
- [113] J.V. Grazulevicius, P. Strohriegl, J. Pielichowski, and K. Pielichowski. *Progress in Polymer Science*, 28(9):1297–1353, 2003.
- [114] C. H. Peters, I. T. Sachs-Quintana, J. P. Kastrop, S. Beaupre, M. Leclerc, and M. D. McGehee. *Advanced Energy Materials*, 1(4):491–494, 2011.
- [115] H.-Y. Chen, J. Hou, S. Zhang, Y. Liang, G. Yang, Y. Yang, L. Yu, Y. Wu, and G. Li. *Nature Photonics*, 3(11):649–653, 2009.
- [116] H. Pan, Y. Li, Y. Wu, P. Liu, B. S. Ong, S. Zhu, and G. Xu. *Journal of the American Chemical Society*, 129(14):4112–4113, 2007.
- [117] Y. Liang, Y. Wu, D. Feng, S.-T. Tsai, H.-J. Son, G. Li, and L. Yu. *Journal of the American Chemical Society*, 131(1):56–57, 2009.
- [118] Y. Liang, D. Feng, Y. Wu, S.-T. Tsai, G. Li, C. Ray, and L. Yu. *Journal of the American Chemical Society*, 131(22):7792–7799, 2009.
- [119] Y. Liang, Z. Xu, J. Xia, S.-T. Tsai, Y. Wu, G. Li, C. Ray, and L. Yu. *Advanced Materials*, 22(20):E135–E138, 2010.
- [120] Z. He, C. Zhong, S. Su, M. Xu, H. Wu, and Y. Cao. Enhanced power-conversion efficiency in polymer solar cells using an inverted device structure. *Nature Photonics*, 6(9):591–595, 2012.
- [121] J. C. Hummelen, B. W. Knight, F. LePeq, F. Wudl, J. Yao, and C. L. Wilkins. *The Journal of Organic Chemistry*, 60(3):532–538, 1995.
- [122] M. M. Wienk, J. M. Kroon, W. J. H. Verhees, J. Knol, J. C. Hummelen, P. A. van Hal, and R. A. J. Janssen. *Angewandte Chemie*, 115(29):3493–3497, 2003.

- [123] H. Imahori. *Bulletin of the Chemical Society of Japan*, 80(4):621–636, 2007.
- [124] *TOPAS-C Traveling-Wave Optical Parametric Amplifier of White-Light Continuum User's Manual*. Light Conversion, Vilnius, Lithuania, 2007.
- [125] R. W. Boyd. *Nonlinear Optics*. Academic Press, Burlington, USA, 3rd edition, 2008.
- [126] D. Meschede. *Optics, Light and Lasers*. Wiley-VCH, Weinheim, Germany, 2nd edition, 2007.
- [127] K. K. Hamamatsu Photonics. *Guide to Streak Cameras*. <http://www.hamamatsu.com>, 2008.
- [128] B. Lang, G. Angulo, and E. Vauthey. *The Journal of Physical Chemistry A*, 110(22):7028–7034, 2006.
- [129] A. Fürstenberg and E. Vauthey. *The Journal of Physical Chemistry B*, 111(43):12610–12620, 2007.
- [130] S. Mukamel. *Nonlinear Optical Spectroscopy*. Oxford University Press, New York, USA, 1st edition, 1995.
- [131] K. Wynne and R.M. Hochstrasser. *Chemical Physics*, 193(3):211–236, 1995.
- [132] K. Ekvall, P. van der Meulen, C. Dhollande, L.-E. Berg, S. Pommeret, R. Naskrecki, and J.-C. Mialocq. *Journal of Applied Physics*, 87(5):2340–2352, 2000.
- [133] M. Lorenc, M. Ziolk, R. Naskrecki, J. Karolczak, J. Kubicki, and A. Maciejewski. *Applied Physics B*, 74(1):19–27, 2002.
- [134] P. Hamm. *Chemical Physics*, 200(3):415–429, 1995.
- [135] T. Jedju and L. Rothberg. *Applied Optics*, 27:615–618, 1988.
- [136] P. Peumans, A. Yakimov, and S. R. Forrest. *Journal of Applied Physics*, 93(7):3693–3723, 2003.
- [137] A. Rao, M. W. B. Wilson, J. M. Hodgkiss, S. Albert-Seifried, H. Bäsler, and R. H. Friend. *Journal of the American Chemical Society*, 132(36):12698–12703, 2010.
- [138] P. J. Jadhav, P. R. Brown, N. Thompson, B. Wunsch, A. Mohanty, S. R. Yost, E. Hontz, T. Van Voorhis, M. G. Bawendi, V. Bulovic, and M. A. Baldo. *Advanced Materials*, 24(46):6169–6174, 2012.

- [139] G. D. Scholes and G. Rumbles. *Nature Materials*, 5(9):683–696, 2006.
- [140] V. K. Thorsmølle, R. D. Averitt, J. Demsar, D. L. Smith, S. Tretiak, R. L. Martin, X. Chi, B. K. Crone, A. P. Ramirez, and A. J. Taylor. *Physical Review Letters*, 102(1):017401, 2009.
- [141] B. Verreet, P. Heremans, A. Stesmans, and B. P. Rand. *Advanced Materials*, 25(38):5504–5507, 2013.
- [142] H. Najafov, B. Lee, Q. Zhou, L. C. Feldman, and V. Podzorov. *Nature Materials*, 9(11):938–943, 2010.
- [143] P. Irkhin and I. Biaggio. *Physical Review Letters*, 107(1):017402, 2011.
- [144] A. Ryasnyanskiy and I. Biaggio. *Physical Review B*, 84(19):193203, 2011.
- [145] T. S. Rose, R. Righini, and M.D. Fayer. *Chemical Physics Letters*, 106(1–2):13–19, 1984.
- [146] R. J. Stöhr, G. J. Beirne, P. Michler, R. Scholz, J. Wrachtrup, and J. Pflaum. *Applied Physics Letters*, 96(23):231902, 2010.
- [147] M. Nothaft and J. Pflaum. *physica status solidi (b)*, 245(5):788–792, 2008.
- [148] T. Petrenko, O. Krylova, F. Neese, and M. Sokolowski. *New Journal of Physics*, 11(1):015001, 2009.
- [149] Y. Chen, B. Lee, D. Fu, and V. Podzorov. *Advanced Materials*, 23(45):5370–5375, 2011.
- [150] H. Najafov, I. Biaggio, V. Podzorov, M. F. Calhoun, and M. E. Gershenson. *Physical Review Letters*, 96(5):056604, 2006.
- [151] N. Sai, M. L. Tiago, J. R. Chelikowsky, and F. A. Reboredo. *Physical Review B*, 77(16):161306, 2008.
- [152] P. Irkhin, A. Ryasnyanskiy, M. Koehler, and I. Biaggio. *Physical Review B*, 86(8):085143, August 2012.
- [153] V. C. Sundar, J. Zaumseil, V. Podzorov, E. Menard, R. L. Willett, T. Somaya, M. E. Gershenson, and J. A. Rogers. *Science*, 303(5664):1644–1646, 2004. PMID: 15016993.
- [154] J.-L. Bredas, J. P. Calbert, D. A. da Silva Filho, and J. Cornil. *Proceedings of the National Academy of Sciences*, 99(9):5804–5809, 2002. PMID: 11972059.

- [155] L. Ma, K. Zhang, C. Kloc, H. Sun, M. E. Michel-Beyerle, and G. G. Gurzadyan. *Physical Chemistry Chemical Physics*, 14(23):8307–8312, 2012.
- [156] Y. Okada, M. Uno, Y. Nakazawa, K. Sasai, K. Matsukawa, M. Yoshimura, Y. Kitaoka, Y. Mori, and J. Takeya. *Physical Review B*, 83(11):113305, 2011.
- [157] E. Venuti, I. Bilotti, R. G. Della Valle, A. Brillante, P. Ranzieri, M. Masino, and A. Girlando. *The Journal of Physical Chemistry C*, 112(44):17416–17422, 2008.
- [158] A. Yu. Kobitski, R. Scholz, D. R. T. Zahn, and H. P. Wagner. *Physical Review B*, 68(15):155201, 2003.
- [159] L. Ma, K. Zhang, C. Kloc, H. Sun, C. Soci, M. E. Michel-Beyerle, and G. G. Gurzadyan. *Physical Review B*, 87(20):201203, 2013.
- [160] S. Tao, H. Matsuzaki, H. Uemura, H. Yada, T. Uemura, J. Takeya, T. Hasegawa, and H. Okamoto. *Physical Review B*, 83(7):075204, 2011.
- [161] A. Furube, R. Katoh, H. Mitsuta, T. Miyadera, and Y. Yoshida. *Meeting Abstracts*, MA2011-01(38):1831–1831, 2011.
- [162] G. B. Piland, J. J. Burdett, D. Kurunthu, and C. J. Bardeen. *The Journal of Physical Chemistry C*, 117(3):1224–1236, 2013.
- [163] X. Wen, P. Yu, C.-T. Yuan, X. Ma, and J. Tang. *The Journal of Physical Chemistry C*, 117(34):17741–17747, 2013.
- [164] S.L. Murov, I. Carmichael, and G.L. Hug. *Handbook of Photochemistry*. Marcel Dekker Inc., New York, USA, 2nd edition, 1993.
- [165] A. Yildiz, P. T. Kissinger, and C. N. Reilley. *The Journal of Chemical Physics*, 49(3):1403–1406, 1968.
- [166] M. Haemori, J. Yamaguchi, S. Yaginuma, K. Itaka, and H. Koinuma. *Japanese Journal of Applied Physics*, 44(6A):3740–3742, 2005.
- [167] M. Tong, N. E. Coates, D. Moses, A. J. Heeger, S. Beaupre, and M. Leclerc. *Physical Review B*, 81(12):125210, 2010.
- [168] N. Banerji, E. Gagnon, P.-Y. Morgantini, S. Valouch, A. R. Mohebbi, J.-H. Seo, M. Leclerc, and A. J. Heeger. *The Journal of Physical Chemistry C*, 116(21):11456–11469, 2012.

- [169] K. G. Jespersen, W. J. D. Beenken, Y. Zaushitsyn, A. Yartsev, M. Andersson, T. Pullerits, and V. Sundström. *The Journal of Chemical Physics*, 121(24):12613, 2004.
- [170] T. Inagaki. *The Journal of Chemical Physics*, 57(6):2526, 1972.
- [171] J. Chappell, D. G. Lidzey, P. C. Jukes, A. M. Higgins, R. L. Thompson, S. O'Connor, I. Grizzi, R. Fletcher, J. O'Brien, M. Geoghegan, and R. A. L. Jones. *Nature Materials*, 2(9):616–621, 2003.
- [172] W. R. Salaneck, O. Inganäs, B. Themans, J. O. Nilsson, B. Sjögren, J.-E. Österholm, J.-L. Bredas, and S. Svensson. *The Journal of Chemical Physics*, 89(8):4613, 1988.
- [173] D. -Q Feng, A. N Caruso, Y. B Losovyj, D. L Shulz, and P. A Dowben. *Polymer Engineering & Science*, 47(9):1359–1364, 2007.
- [174] J.-F. Morin and M. Leclerc. *Macromolecules*, 35(22):8413–8417, 2002.
- [175] R. Stahl, C. Lambert, C. Kaiser, R. Wortmann, and R. Jakober. *Chemistry - A European Journal*, 12(8):2358–2370, 2006.
- [176] L. E. Polander, L. Pandey, S. Barlow, S. P. Tiwari, C. Risko, B. Kippelen, J.-L. Bredas, and S. R. Marder. *The Journal of Physical Chemistry C*, 115(46):23149–23163, 2011.
- [177] F. Etzold, I. A. Howard, R. Mauer, M. Meister, T.-D. Kim, K.-S. Lee, N. S. Baek, and F. Laquai. *Journal of the American Chemical Society*, 133(24):9469–9479, 2011.
- [178] H. Yamagata and F. C. Spano. *The Journal of Chemical Physics*, 136(18):184901–184901–14, 2012.
- [179] H. Sirringhaus, P. J. Brown, R. H. Friend, M. M. Nielsen, K. Bechgaard, B. M. W. Langeveld-Voss, A. J. H. Spiering, R. A. J. Janssen, E. W. Meijer, P. Herwig, and D. M. de Leeuw. *Nature*, 401(6754):685–688, 1999.
- [180] Y. Kim, S. Cook, S. M. Tuladhar, S. A. Choulis, J. Nelson, J. R. Durrant, D. D. C. Bradley, M. Giles, I. McCulloch, C.-S. Ha, and M. Ree. *Nature Materials*, 5(3):197–203, 2006.
- [181] X. Lu, H. Hlaing, D. S. Germack, J. Peet, W. H. Jo, D. Andrienko, K. Kremer, and B. M. Ocko. *Nature Communications*, 3:795, 2012.

- [182] C. L. Donley, J. Zaumseil, J. W. Andreasen, M. M. Nielsen, H. Sirringhaus, R. H. Friend, and J.-S. Kim. *Journal of the American Chemical Society*, 127(37):12890–12899, 2005.
- [183] N. Banerji, S. Cowan, M. Leclerc, E. Vauthey, and A. J. Heeger. *Journal of the American Chemical Society*, 132(49):17459–17470, 2010.
- [184] J. M. Hodgkiss, S. Albert-Seifried, A. Rao, A. J. Barker, A. R. Campbell, R. A. Marsh, and R. H. Friend. *Advanced Functional Materials*, 22(8):1567–1577, 2012.
- [185] S. De, T. Pascher, M. Maiti, K. G. Jespersen, T. Kesti, F. Zhang, O. Inganäs, A. Yartsev, and V. Sundström. *Journal of the American Chemical Society*, 129(27):8466–8472, 2007.
- [186] H. Ohkita, S. Cook, Y. Astuti, W. Duffy, S. Tierney, W. Zhang, M. Heeney, I. McCulloch, J. Nelson, D. D. C. Bradley, and J. R. Durrant. *Journal of the American Chemical Society*, 130(10):3030–3042, 2008.
- [187] W. Luzny and A. Pron. *Synthetic Metals*, 84(1–3):573–574, 1997.
- [188] G. Dicker, M. P. de Haas, L. D.A. Siebbeles, and J. M. Warman. *Physical Review B*, 70(4):045203, 2004.
- [189] F. Paquin, G. Latini, M. Sakowicz, P.-L. Karsenti, L. Wang, D. Beljonne, N. Stingelin, and C. Silva. *Physical Review Letters*, 106(19):197401, 2011.
- [190] N. C. Miller, E. Cho, R. Gysel, C. Risko, V. Coropceanu, C. E. Miller, S. Sweetnam, A. Sellinger, M. Heeney, I. McCulloch, J.-L. Bredas, M. F. Toney, and M. D. McGehee. *Advanced Energy Materials*, 2(10):1208–1217, 2012.
- [191] Z. M. Beiley, E. T. Hoke, R. Noriega, J. Dacuna, G. F. Burkhard, J. A. Bartelt, A. Salleo, M. F. Toney, and M. D. McGehee. *Advanced Energy Materials*, 1(5):954–962, 2011.
- [192] B. Carsten, J. M. Szarko, H. J. Son, W. Wang, L. Lu, F. He, B. S. Rolczynski, S. J. Lou, L. X. Chen, and L. Yu. *Journal of the American Chemical Society*, 133(50):20468–20475, 2011.
- [193] B. S. Rolczynski, J. M. Szarko, H. J. Son, Y. Liang, L. Yu, and L. X. Chen. *J. Am. Chem. Soc.*, 134(9):4142–4152, 2012.
- [194] G. Yu, J. Gao, J. C. Hummelen, F. Wudl, and A. J. Heeger. *Science*, 270(5243):1789–1791, 1995.

- [195] D. Chirvase, J. Parisi, J. C. Hummelen, and V. Dyakonov. *Nanotechnology*, 15(9):1317, 2004.
- [196] T. Erb, U. Zhokhavets, G. Gobsch, S. Raleva, B. Stühn, P. Schilinsky, C. Waldauf, and C. J. Brabec. *Advanced Functional Materials*, 15(7):1193–1196, 2005.
- [197] M. Campoy-Quiles, T. Ferenczi, T. Agostinelli, P. G. Etchegoin, Y. Kim, T. D. Anthopoulos, P. N. Stavrinou, D. D. C. Bradley, and J. Nelson. *Nature Materials*, 7(2):158–164, 2008.
- [198] S. J. Lou, J. M. Szarko, T. Xu, L. Yu, T. J. Marks, and L. X. Chen. *Journal of the American Chemical Society*, 133(51):20661–20663, 2011.
- [199] J. K. Lee, W. L. Ma, C. J. Brabec, J. Yuen, J. S. Moon, J. Y. Kim, K. Lee, G. C. Bazan, and A. J. Heeger. *Journal of the American Chemical Society*, 130(11):3619–3623, 2008.
- [200] T. Drori, C.-X. Sheng, A. Ndobé, S. Singh, J. Holt, and Z. V. Vardeny. *Physical Review Letters*, 101(3):037401–4, 2008.
- [201] B. A. Collins, Z. Li, J. R. Tumbleston, E. Gann, C. R. McNeill, and H. Ade. *Advanced Energy Materials*, 3(1):65–74, 2013.
- [202] L. W. Barbour, R. D. Pensack, M. Hegadorn, S. Arzhantsev, and J. B. Asbury. *The Journal of Physical Chemistry C*, 112(10):3926–3934, 2008.
- [203] I. A. Howard, R. Mauer, M. Meister, and F. Laquai. *Journal of the American Chemical Society*, 132(42):14866–14876, 2010.
- [204] J. Planes, Y. Samson, and Y. Cheguettine. *Applied Physics Letters*, 75(10):1395, 1999.
- [205] P. J. James, M. Antognozzi, J. Tamayo, T. J. McMaster, J. M. Newton, and M. J. Miles. *Langmuir*, 17(2):349–360, 2001.
- [206] K. D. O’Nei and O. A. Semenikhin. *The Journal of Physical Chemistry C*, 111(40):14823–14832, 2007.
- [207] M. R. Hammond, R. J. Kline, A. A. Herzing, L. J. Richter, D. S. Germack, H.-W. Ro, C. L. Soles, D. A. Fischer, T. Xu, L. Yu, M. F. Toney, and D. M. DeLongchamp. *ACS Nano*, 5(10):8248–8257, 2011.
- [208] C. Zang. US patent b2004 0229925, 2004.
- [209] H. A. M van Mullekom, J. A. J. M Vekemans, and E. W Meijer. *Chemistry - A European Journal*, 4(7):1235–1243, 1998.

